MODELING AND COMPENSATION OF HYSTERESIS IN PIEZOELECTRIC ACTUATORS: A PHYSICAL APPROACH

MARC SAVOIE

A DISSERTATION SUBMITTED TO THE FACULTY OF GRADUATE STUDIES
IN PARTIAL FULFILMENT OF THE REQUIREMENTS
FOR THE DEGREE OF
DOCTOR OF PHILOSOPHY

GRADUATE PROGRAM IN PHYSICS AND ASTRONOMY
YORK UNIVERSITY
TORONTO, ONTARIO

MAY 2022

Abstract

A study in the polarization domain is conducted by probing the impedance of the piezoelectric actuator as it moves along its trajectory. A sensing signal is overlaid over a driving signal that is used to vary the position of the device. The electric polarisation is extracted from the capacitance measurement calculated from the impedance. These polarisation curves are then modelled using the Jiles-Atherton model and compensated for using the inverse model. These measurements give insight into the ferroelectric processes within the piezoelectric actuator, which operate on the polarisation state.

In addition, research has been conducted on the topic of parameter estimation of hysteresis models. This dissertation proposes a Monte Carlo study on a novel normalised Jiles-Atherton model to generate a statistical set of model solutions to compare area and remnant displacement characteristics for different parameter selections. Two parameters were found to be the most responsible for changes in these characteristics, and solutions near the desired values of the measured hysteresis curves were found to be densely distributed in certain areas of the parameter space. Different parameter estimation techniques are proposed for the Prandtl-Ishlinskii model. For this model, the parameters have geometrical significance in the slope of certain points of the hysteresis curve. A novel rescaling procedure is developed to scale a Prandtl-Ishlinskii model hysteresis curve area to a new value without requiring a refitting of the coefficients and a frequency-dependent Prandtl-Ishlinskii model is developed.

Finally, a temperature-dependent, asymmetric Prandtl-Ishlinskii (TAPI) model is de-

veloped to account for the changes in hysteresis due to the external temperature. These effects are modelled in the charge domain as an extra bound charge that appears as a result of domain reorientation effects. The temperature effectively changes the amount of energy required to break pinning sites in the actuator which changes the shape of the curve. The TAPI model is then implemented on a Fabry-Perot interferometer system consisting of three piezoelectric actuators controlling the placement of a mirror forming the etalon. A decoupled inverse TAPI model is shown to effectively linearise the output of this system at different temperatures.

Acknowledgements

Firstly, I would like to thank Prof. Shan for being my PhD supervisor during this project. The culture he has cultivated in SDCNLab has kept me inspired and his wise advice has helped make this research possible. His encouragements in the face of difficult problems and his project management has helped myself and many others in the research group to stay on topic and to refine our ideas into interesting research.

Thanks also to my committee members Jianguo Wang and Ryan Orszulik for serving as my committee members. Our discussions helped provide a fresh perspective in my research. I am also thankful to the late George Vukovich, who served in my committee before his passing.

To all my labmates in SDCNLab, it is the people who make a good environment and it was a pleasure to work alongside everyone I have met there. Thank you to Ganesh, Scott, Ali, William, Samira, Linda, Peng, Mike, Hassan, Mingfeng, Hao, Huarong, Yibo, Shiyuan, Ti, Hunter, Ingredy, Shuo and everyone else who I have met through the lab.

Finally, I would like to acknowledge my family. My mother Nancy and my father Normand, who have never stopped being proud of the things I have done and are never shy to show support. To my brother Mathieu and my sister Monique. I love you guys!

Table of Contents

List of Tables

List of Figures

Abbreviations

BW: Bouc-Wen

FPI: Fabry-Perot Interferometer

JA: Jiles-Atherton

PEA: Piezoelectric actuator

PI: Prandtl-Ishlinskii

PID: Proportional Integral Derivative

PSO: Particle Swarm Optimization

TAPI: Temperature-dependent asymmetric Prandtl-Ishlinskii

Chapter 1

Introduction

Piezoelectricity is an effect in some materials that creates an electric charge accumulation that results in an apparent voltage across their surfaces in response to mechanical stress. The term is a joining of the Greek words 'piezein' meaning to squeeze and the word 'elektron' meaning amber. Piezoelectric devices are widely used in diverse applications ranging from actuators, sensors, clocks, motors, antennas, energy harvesters, to name a few [2–7]. Due to their electromechanical coupling and a number of their appealing properties, there appears to be no end to the applicability of these devices. However, piezoelectric materials suffer from a number of nonlinearities that can render their use more difficult. In positioning applications, the hysteresis and the creep are major characteristics that must be understood to prevent inaccuracies in the movement [8, 9]. Additionally, their frequency dependent behavior and temperature dependence create challenging problems to extend the applicability range of the devices [10].

Piezoelectrics used as actuators have a wide range of different uses in today's technology. As the most direct method of exploiting its electromechanical coupling, they can be utilized as potential solutions to problems that seek electrical control over mechanical properties of a system. One of the advantages of using piezoelectrics in actuator applications is that

it provides direct linear actuation without requiring the interaction of many subsystems which could be the case with mechanical actuators. Their movement is smooth and free of backlash and can range from the nanometer level to the millimeter level [11]. An interesting mode of operation that is possible with piezoelectric devices is as self-sensing actuators. This combines their sensing and actuation properties together which is interesting to obtain a truly collocated sensor and system in a closed loop controller [12].

Two applications in particular have gotten a lot of attention in piezoelectric actuation. The first of these is the vibration control of structures using piezoelectrics. They can be bonded or embedded into the object if desired to achieve this performance. Their collocated nature is appealing for velocity feedback systems due to improved stability properties [13]. Damping vibrations has also been done with piezoelectric materials through a technique called piezoelectric shunt damping by attaching an electrical impedance to the bonded piezoelectric on the system. By tuning the resonant electrical circuit to certain vibrational modes that are not desired in the system, the shunt damping circuit can absorb the vibration passively at these frequencies.

Another interesting and widely studied application of piezoelectric actuators is in nanopositioning applications. These applications seek to exploit the very fine displacement ranges that are possible with piezoelectric crystals. Piezoelectric actuators are notably used in atomic force microscopy applications. In these systems, a cantilever with a very fine needle is scanned across the surface of a sample and the inter-molecular forces that act on the cantilever serve to create small deflections that can be measured by laser. The use of the piezoelectric actuator is normally in position tracking of the needle. The better this task i performed, the sharper the image will be [9]. The sub-nanometer resolution has enabled some interesting atomic force microscopy imaging results in recent years such a the imaging of single molecules and chemical bonds [14, 15]. In the past few years, more and more challenging microscopy experiments are being performed due to the increased understanding

of the system performance in multiple conditions [16]. Other applications in nanopositioning is in spectroscopy. Fabry-Perot spectrometers rely on the positioning of their mirrors to scan through light frequencies and their positioning is often performed with piezoelectric-based nanopositioners [17].

1.1 Piezoelectric Materials

Piezoelectric materials are a wide class of materials that exhibit the piezoelectric effect. The piezoelectric effect was first theorized by René Haüy and Antoine Becquerel after the initial discovery of pyroelectricity by Carl Linnaeus and Franz Aepinius. The first observations of the piezoelectric effect came later by Pierre and Jacques Curie in 1880. In their experiments, they found the piezoelectric effect in tourmaline, quartz, topaz, cane sugar, and Rochelle salt. A year later, the converse piezoelectric effect was discovered by Gabriel Lippmann, demonstrating the symmetric nature of this effect. The piezoelectric effect was not extensively used in applications before the first world war when a piezoelectric-based ultrasonic sonar was developed by Paul Langevin in 1917.

The direct piezoelectric effect is a property of a material where pressure can generate charge on the surface of the material. This represents a conversion of mechanical energy into electrical energy. The opposite effect when an applied voltage or electric field is applied to the material is called the inverse piezoelectric effect and converts electrical energy into mechanical energy. The nature of the piezoelectric effect stems from the dipole moments of constituents of the solid. For crystal structures that create a net polarization in response to mechanical stresses that induce deformation, the piezoelectric effect is the natural result. This polarization implies charge accumulations in certain areas which by definition represents the direct piezoelectric effect. Two classes of crystal structures exist that induce the piezoelectric effect. The first class is a polar crystal in which a spontaneous polarization can exist. These

crystal structures represent a symmetry break in the crystal. In many polar crystals, this symmetry break comes from an ion within the crystal that is not centered. Deformation of the crystal structure will move this atom and change the resultant dipole moment of the crystal. Conversely, an electric field can also serve to move the ion based on the induced electric force. The most commonly used piezoelectric materials are this class of crystal due to their superior electromechanical coupling and piezoelectric coefficients. Commonly used polar piezoelectric materials are lead zirconate titanate (PZT) and barium titanate (BTO), which are both examples of perovskite crystals. Interestingly, piezoelectric materials that have polar crystal structures are also pyroelectric. The pyroelectric effect is the property of converting thermal energy to electric energy by inducing an electric charge by changing the temperature of the material. The mechanism for pyroelectricity relies on the polar nature of the molecule because temperature serves to increase the average energy of atoms within the crystal. If a crystal is non-polar, temperature increases will serve to change the position over time of the atoms of the crystal, but their average distribution will continue to be non-polar in the absence of external factors. However, in the polar case, temperature can change the stability position of the ion that is creating the asymmetry in the material. Because of this phenomena, all pyroelectric crystals are piezoelectric but not all piezoelectric materials are pyroelectric due to the existence of non-polar piezoelectrics. An additional class of polar crystals are ferroelectric crystals. Ferroelectric crystals are polar crystals which imply both piezoelectricity and pyroelectricity, but they possess the property that the dipole moment of the unit cell can be reversed. Fig. 1.1 shows this dependency in the category of dielectrics. Ferroelectricity implies pyroelectricity, which implies piezoelectricity, which implies dielectric.

The mathematical formulation of piezoelectricity has been done in different ways. most influential is the linear description of the piezoelectric effect which is outlined in the IEEE standard for linear piezoelectricity [18]. A set of tensor equations for piezoelectric materials

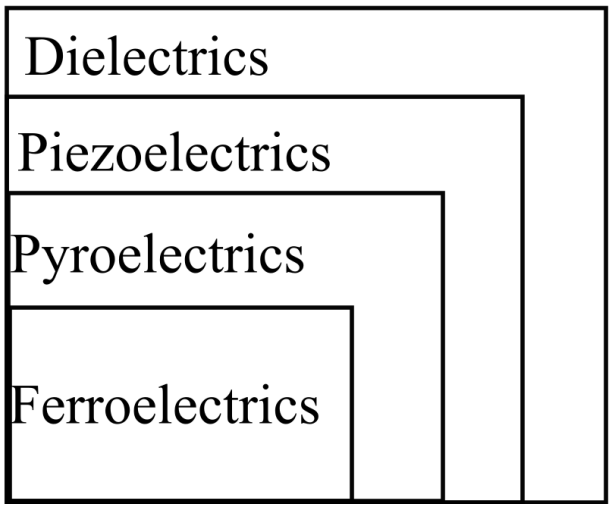

Figure 1.1: Venn diagram of dielectrics.

are often stated from this linear theory which relate the mechanical stress and strain to the electric field and electric displacement. The tensor formulation of the piezoelectric constitutive equations are written as follows.

$$S_{ij} = s_{ijkl}T_{kl} + d_{ijk}E_k \tag{1.1}$$

$$D_i = d_{ikl}T_{kl} + \varepsilon_{ij}E_j \tag{1.2}$$

Where S_{ij} represents the strain tensor, s_{ijkl} is the elastic compliance tensor, T_{kl} is the stress tensor, d_{ijk} is the piezoelectric tensor, E_k is the electric field in direction k, D_i is the electric displacement in direction i, and ε_{ij} is the permittivity tensor. This equation is essentially a first order approximation of the electromechanical coupling of the piezoelectric device and is valid but does not provide any insight on other dependencies such as temperature nor does it provide a description of nonlinear phenomena that may be present in practice. To incorporate higher order effects, higher order stress and field terms can be held. Other approaches to generating constitutive equations that do not linearize the system can be utilized as well such as those derived from balance laws as seen in [19]. Modeling of the

piezoelectric effect can also be done by examining the nano-scale interactions within the material. For ferroelectrics, modeling of the polarization state has parallels with ferromagnetic materials which have attracted a good amount of attention [20]. The polarization behavior of ferroelectric materials is relatively well understood though micromechanical models for the electromechanical coupling is normally complicated [21, 22]. However, nonlinear models of the polarization can serve to create a nonlinear component for the linear constitutive laws.

Piezoelectric materials possess different crystal structures. The most commonly seen in piezoelectric devices are the perovskite piezoceramic materials. One of the most used compounds for piezoelectric devices is PZT which represents a ferroelectric variety of piezoelectrics. It possesses large electromechanical coupling, high curie temperature, and high manufacturing tunability though doping. Ferroelectric materials are often categories into soft and hard categories. Soft ferroelectrics are characterized by their ease of inducing polarization. This is described by their low coercivity value which characterizes how high an electric field must be to reverse the orientation of the polarization of the crystal. Having easy to flip dipoles in the system makes the electromechanical coupling larger. However, soft ferroelectrics normally have higher hysteresis and other nonlinearities than their hard counterparts. Soft ferroelectrics are typically used in actuators and sensors due to their high coupling. Hard ferroelectrics instead are capable of handling higher electric and mechanical stresses than their soft counterparts and possess more stable properties [23]. These materials are often used in ultrasonic applications [24].

A class of piezoelectrics that has been gaining some attention recently are the polymer piezoelectrics. One of the biggest problems with piezoceramic materials is their brittle nature. Piezoelectric polymers such as PVDF solve this issue for flexible applications which are being explored more and more in fields such as soft robotics [25]. Some of the main challenges in this category of piezoelectric materials is their significant loss in remnant polarization over a relatively short number of switching cycles [26].

1.2 Piezoelectric Nonlinearities

Piezoelectric materials are plagued by nonlinearities that reduce performance in many applications. these effects complicate the simple linear description of the piezoelectric effect and can deteriorate control performance if not accounted for. To make matters worse, many properties of piezoelectric materials are determined at low field levels to maintain the linear range of the devices [27]. However, real world applications are often beyond the range of linearity which creates discrepancies between the published data and the applications. The result has been a large research interest in describing and developing techniques to compensate for the nonlinearities present in the piezoelectric system. In soft ferroelectrics, even adding an additional field order to the constitutive equations was found to not produce suitable agreement with experiments and a hysteresis description is needed to account for the micromechanical irreversible losses found in the materials [28].

Hysteresis is a nonlinearity that is found between the polarization and the electric field in ferroelectrics and is observed between the applied voltage and the displacement in piezoelectric actuators. The word is derived from the ancient Greek word "husteros" meaning delay. The first descriptions of hysteresis came from the observations in ferromagnetic materials that the magnetization of some materials would tend to lag behind the magnetic field which created loop patters characteristic of hysteresis. A simple visual example of hysteresis can be shown using a two state relay system as shown in Fig. 1.2. In this system, the center of the relay is at a position s on the $u(t)$ axis and vertical lines are found at distances $\pm r$ that show discontinuous switching between two states $y = \pm 1$ similar to a step function, but two steps occur depending on the direction of travel in the $u(t)$ axis. If the value of the output is $y = -1$ and $u(t)$ increases, then the output will remain at $y = -1$ until it reaches the threshold $u(t) \geq s + r$ where it will transition from a value of -1 to $+1$. If instead $y = -1$ and $u(t)$ decreases, then no transition can happen even if $u(t)$ crosses the $s - r$ threshold.

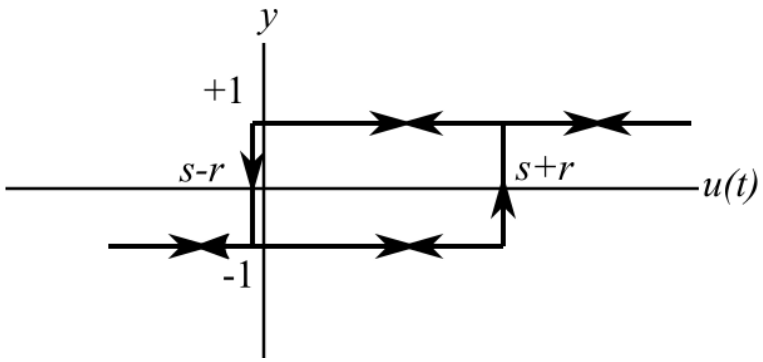

Figure 1.2: A relay centered at s of width $2r$

This threshold describes only the transition between positive outputs to negative outputs and thus the output must remain negative. For the positive case, if $y = 1$ and $u(t)$ increases, then it will remain 1 throughout the range of $u(t) - r$. However, if the input decreases to a value that is below $s - r$, then the output will transition to the negative $y = -1$ value.

This phenomena of holding onto past values of output or lagging behind the input is often described as a memory effect since the output can retain different values for the same input depending on the history of the input. It's not surprising that this effect has found uses in data storage applications such as computer hard drives that are capable of reading and writing bits of data using magnetic hysteresis [29]. In other situations, hysteresis degrades the performance of systems such as hysteresis found in gears [30].

In many applications and as seen in the relay operator shown in Fig. 1.2, the hysteresis is assumed to be a rate independent effect. This means that the speed at which the input changes does not affect the hysteresis effect and doesn't change the shape of the relay in the input-output plane. In real applications, this is an idealization since in practice, the physical processes that create hysteresis do in general depend on rate because transitions in physical systems require time to occur and cannot occur instantaneously [31]. A typical property of a hysteresis curve is a looping behavior. In the relay example, the loop is characterized by the rectangular section between $[s - r, s + r]$.

In hysteresis modeling, a few distinctions are often made for different approaches in the modeling of this nonlinearity. Firstly, there are phenomenological models which are based off of mathematical notions to describe hysteresis empirically without physical insight into the mechanism that causes hysteresis. Occasionally, physical significance can be assigned to phenomenological models after the fact. Most hysteresis models are phenomenological in nature and even the physical models are often used in a phenomenological manor if the parameters are not easily obtained from the system. Examples of phenomenological hysteresis models are polynomial models, operator-based models such as the Prandtl-Ishlinskii model and the Krasnoselskii-Pokrovskii models, and some differential equation-based models such as the Duheim models and the Bouc-Wen model [32–36]. Physical models are another category of hysteresis models and are based on the physical process that creates the hysteresis in the system. These models are typically system dependent since hysteresis in one system may not have the same cause as in a different system. For piezoelectric applications where the piezoelectric material is made of a ferroelectric material, a physics based hysteresis description has been described using the Jiles-Atherton model [20][37]. Hysteresis models are often divided into differential equations-based models and operator based approaches since these two approaches have a number of different modeling approaches. For differential equation-based approaches, the hysteresis is described by differential equations usually producing a smooth hysteresis curve. In the cases of the Duheim and the Bouc-Wen models, they are inspired by adding nonlinear terms to a typical second order dynamical system. The Bouc-Wen model adds to the force term a hysteretic parameter that is itself described by a first order differential equation that depends on the first derivative of the input. The Duheim model adds hysteresis in a similar way but the first order derivative that describes the hysteretic parameter is expressed in a different way. The Jiles-Atherton model takes an entirely different approach to describe hysteresis by examining pinning effects in the domain wall motion within the material and the differential equation that describes it is

more complicated. For the operator based approaches, the Preisach model is based on the relay operator described in Fig. 1.2. In this approach and most other operator approaches, a section of the hysteresis curve is described by the operator in question and a superposition of all operators describing different sections is performed to model the desired curve based on its data. Other approaches in this category use different operators such as the Prandtl-Ishlinskii model being based on the play operator and the Krasnoselskii-Pokrovskii model is based on the Krasnoselskii-Pokrovskii kernel operator [38]. Other approaches that do not directly fall into these categories exist and some notable ones are the ellipse based hysteresis model and the piece-wise descriptions [39, 40].

Hysteresis effects dominate the nonlinearity of piezoelectrics that track signals and cause challenges for tracking controllers. However, for applications where positioning is held at specific values for extended periods of time, hysteresis can often be neglected. The creep effect on the other hand is a second major nonlinearity in piezoelectric systems. The creep is characterized as a drifting output displacement from the piezoelectric actuator after the position of the actuator is changed. Fig. 1.3 shows the creep behavior of a piezoelectric actuator driven by a step signal. It can be seen when compared to the step signal that the output behavior of the piezoelectic actuator slowly rises after its quick response to the signal. The slow rising comes from the time required for domains in the solid to react to the electric field. These domains are pinned and require some energy to reorient themselves. But the process is an average process at macroscopic levels. This means that not all domains will react to the field at the same time and some may require longer before their pinning sites are finally conquered. In many applications, the creep is described with a simple logarithmic model [41]. However, as has been noted by other sources, the creep parameters are different depending on the output history. An operator based creep model is described in [42] to help extend the range of applicability while also pairing well with hysteresis models for inverse compensation. Fractional order models for piezoelectrics can describe the creep effects as

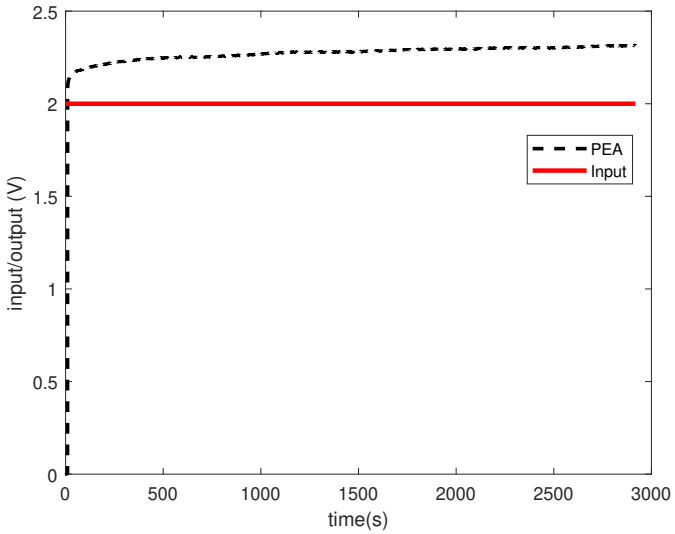

Figure 1.3: Piezoelectric creep driven by a step signal showcasing a gradual increase in displacement over time.

seen in [43] while also lending themselves well to combinations with hysteresis [44].

External factors can affect the piezoelectric performance. Thermal drift is a well known nonlinearity in piezoelectrics that affect their positioning performance [45]. Temperature is known to affect the domain wall dynamics of ferroelectrics which in turn affects the characteristics of the other ferroelectric nonlinearities. For example, hysteresis must be temperature dependent in piezoelectrics because temperature affects the saturation polarization and the coercive fields in ferroelectrics [46]. Regular thermal expansion is also present in piezoelectrics where in many cases, the thermal expansion coefficient is found to be negative [47]. Material aging processes also affect the properties of piezoelectric actuators over the course of their use which can create a need to re-tune control parameters in some applications [48]. In theory, temperature also affects the linear constitutive coefficients in piezoelectrics as well and thermal conductivity is often added into these models by considering the first order approximation of temperature variation[19]. However, a nonlinear model of a piezoelectric coefficient on its own is not easily predicted based on the nature of the material. Ferroelectric

theory provides a framework to predict temperature-based effects in piezoelectric actuators (PEAs).

In different applications, different techniques are used to compensate for the nonlinearities in piezoelectrics. Passive compensation of piezoelectric temperature effects has been performed through the use of axial loading [49]. Many of the hysteresis models possess inverses that can be used to shape the input of the system to linearize it [50]. In certain controller designs, an inverse isn't even needed. For example, a sliding mode controller can be designed with a direct model of the hysteresis [51]. Some control techniques are capable of considering nonlinearity in the system as disturbances. For example, iterative learning control strategies are useful for many scanning piezoelectric applications which can iteratively compensate for disturbances caused by hysteresis [52]. Combining such strategies with modeling yields even improved performance in these systems [53]. It was also noticed that piezoelectric hysteresis is largely compensated if it is driven through charge instead of voltage. The reason for this is that charge is a direct quantification of the polarization of the ferroelectric whereas voltage driven approaches drive the device using electric fields which is known for its hysteresis [54].

1.3 Research Objectives

In this dissertation, the modeling of piezoelectric actuator hysteresis is investigated with a focus on physical significance within the models. The work is largely inspired by ferroelectric processes that are the source of the PEA hysteresis. However, the investigation does not end with the traditional physics-based model provided by the Jiles-Atherton approach. Other approaches are investigated and compared. The difference with with the approaches in this dissertation compared to other methods of modification of hysteresis models is that a bottom-up approach is taken to introduce effects into the modeling which allows for physical insights to be injected into the modeling rather than adding parameter-dependent factors to

the model of unknown significance. This approach is meaningful because it adds information to the modeling which can be further extended with additional information when needed.

In Chapter 2, the Prandtl-Ishlinskii model, the Bouc-Wen model, and the Jiles-Atherton model are compared in their performances as PEA hysteresis compensators. Advantages and disadvantages of the different models are investigated and their performance coupled with proportional-integral controllers is investigated.

In Chapter 3, an investigation of the polarization in PEAs is conducted by overlaying the input signal onto the PEA with a low amplitude sensing signal that allows for the tracking of the impedance of the PEA over the course of its movement. Using this technique, it is shown that compensating for the hysteresis in the polarization also compensates for the hysteresis in the positioning.

In Chapter 4, parameter estimation of hysteresis parameters is investigated and improved. Monte Carlo simulations are conducted on the Jiles-Atherton model to examine how parameter selection influences characteristics of the hysteresis curves. A normalized Jiles-Atherton model is developed that retains inversion properties and allows easy comparison between different hysteresis curves generated by the model. Comparisons between the normalized areas and remnant displacements generated by different parameters is investigated in the data. A novel particle swarm optimization formulation is developed based on the results of the Monte Carlo simulations. Additionally, simple scaling method is proposed for the Prandtl-Ishlinskii model that utilizes several model properties to change hysteresis properties without the need to refitting parameters.

In Chapter 5, the temperature properties are investigated on the PEA system. Temperature was found to change the hysteresis shape requiring re-tuning of the hysteresis models. A temperature extended asymmetric Prandtl-Ishlinskii model is developed based on the expected temperature dependence on the ferroelectric behavior as described by the domain wall model. To add these effects into the Prandtl-Ishlinskii model, the case of a nonlinear capacitive

component is studied in an electromechanical model in which the Prandtl-Ishlinskii model can be assigned physical significance. Parameter estimation for this new model is described and its performance is assessed for a range of different temperatures and input values. Finally, a temperature dependent coupled Prandtl-Ishlinskii model is developed and tested on a Fabry-Perot interferometer to compensate for hysteresis over three mechanically coupled PEAs while also compensating for the mechanical coupling effects.

In Chapter 6, conclusions are drawn from this work and some future research directions based on the investigations in this dissertation are suggested.

Chapter 2

Established Models

The control of PEAs is plagued with nonlinearities that may degrade their positioning performance. For continuous signals that provide movement at a higher frequency, hysteresis is generally the dominant nonlinearity that degrades tracking performance. However, for maintaining a specific position, creep dominates over hysteresis. This dissertation is mainly focused on the hysteresis nonlinearity and thus, this chapter is dedicated to studying established models in the theory of hysteresis modeling and comparing their effectiveness as compensators to linearize PEA displacement and to improve the performance of simple linear controllers.

The objective of this chapter is to provide an overview of the existing literature on models used in this dissertation and to compare these classical models against each other based on their tracking accuracy both with and without a closed-loop controller.

2.1 Hysteresis Models

Hysteresis is a phenomena of energy loss in a material which causes the output to lag behind the input. This effect has been studied most seriously in the case of ferromagnetism in

which the magnetisation and the magnetic field form a characteristic hysteresis curve.[50] In ferromagnetic theory, the cause of the lag is due to pinning effects in the material which require energy to break free from before the magnetic particle is free to reorient.[55]

Hysteresis models are either physics-based, or phenomenological. They are further classified into differential equation-based models and operator-based models.[56] These two major categories encompass most of the most common modeling approaches for hysteresis. The differential equation-based models are defined by a set of differential equations. Some common models in this category are the Duheim model [34], the Bouc-Wen model [33], the Jiles-Atherton model [20], and the Dahl model [57]. These models are often described in terms of friction terms due to their description often relying on the first derivative of the position. In fact, as described earlier, hysteresis is an energy loss effect therefor friction is a natural analog in the mechanical domain.

Operator-based models are described by a superposition of mathematical operators to systematically describe a hysteresis curve. Common models in this category are the Preisach model [58], the Prandtl-Ishlinskii model [59], the Krasnoselskii-Pokrovskii model [**?**], and the Maxwell-slip model [43]. In most cases, operator-based models are composed of simple mathematical operators that are can be superimposed in such a way that their coefficients can be obtained geometrically giving them an advantage over differential equation-based models. However, in many cases they do not generate smooth hysteresis curves like the differential equation-based models.

Other approaches to model hysteresis that do not fall into these two categories exist such as the ellipse-based method described in [39] in which the hysteresis curve is assumed to describe an ellipse and the best fitting ellipse is sought. Also, a polynomial-based approach has been utilized to create hysteresis curves that maintain the desired properties.[36]

2.1.1 Prandl-Ishlinskii Model

The Prandtl-Ishlinskii (PI) model is an operator based model that is based on the play operator. The play operator is a mathematical object that maps an input $u(t)$ onto an output $y(t)$. Due to the nature of hysteresis possessing multiple possible outputs for a given input, a functional description of the effect is insufficient to model this behavior. The operator is characterized by a threshold value r that describes a period within the output that is unchanging. The purpose of the threshold is to switch between two modes in the play operator. The first mode of operation occurs for input values that are smaller than the threshold value. In this mode, the output does not change. Once the input reaches the threshold value, the mode of operation changes to duplicate the input. This mode switching occurs as the input is varied in one direction (eg. monotonically increasing or decreasing inputs). If the direction of the input is changed, the output will again hold its value until the threshold is reached. Fig. 2.2 shows the resulting input-output behavior of the play operator. It can be seen from the time plot that there is a lag between in input and output which is dictated by the threshold r. When input and output is plotted together, the resulting shape forms a parallelogram centered at the origin. The top and bottom of the parallelogram are parallel to the input axis and represent regions where the output do not change. these sections have length $2r$. The sides are diagonal and vary at the same rate as the input. The threshold appears naturally in the input-output plot at the start of the curve where the play operator output holds its value until it reaches its orbiting parallelogram.

The play operator can be described iteratively with dependence on a threshold r and an input u. The output of the play operator is denoted by $w(t)$ while a fully unambiguous notation is often written as $w(t) = F_r[u](t)$ which explicitly states the dependence on u and r.[59]

$$w(0) = F_r[u](0) = f_r(u(0), w_0) \tag{2.1}$$

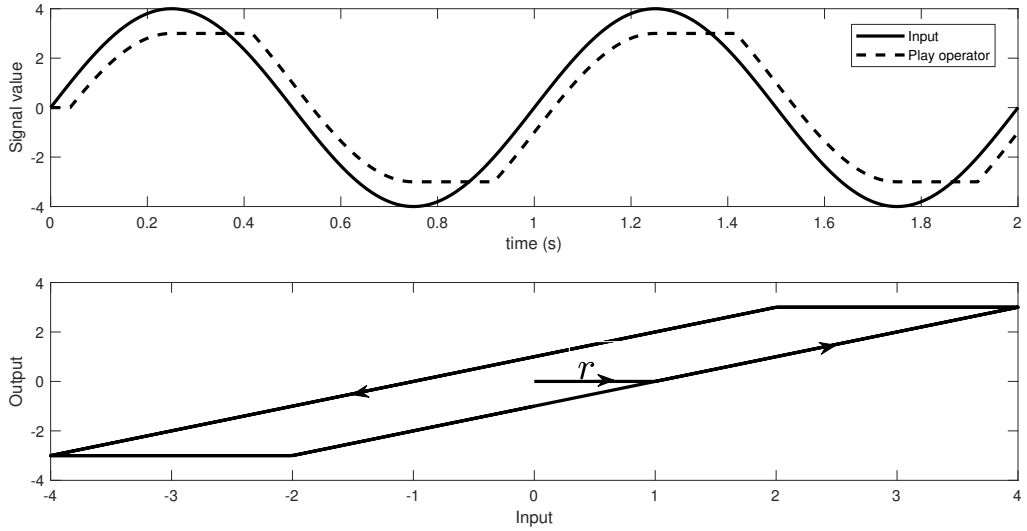

Figure 2.1: The Play operator with $r = 1$. The top shows the input and output over time. The bottom shows input and output plotted together

$$w(t_i) = F_r[u](0) = f_r(u(t_i), w(t_{i-1})) \tag{2.2}$$

Eq. (2.1) denotes an initial condition requirement for the play operator which can be set with the parameter w_0. Eq. (2.2) defines each point of the play operator through an iterative relationship for each time instant $0 < t_{i-1} < t_i$. The quantity $f_r(u, w)$ is defined as follows

$$f_r(u, w) = \max(u - r, \min(u + r, w)) \tag{2.3}$$

While the PI model is built upon the play operator, some variant operators are useful in the modeling of PEA hysteresis. Many PEA systems are rated for unipolar operation. In these applications, an operator that has a center of symmetry in some other location than the origin may be appealing. The one-sided play operator (OSP) has this properly and simplifies modeling of the hysteresis curve. An example of the input-output behavior of the OSP operator can be found in The main difference between the play operator and the

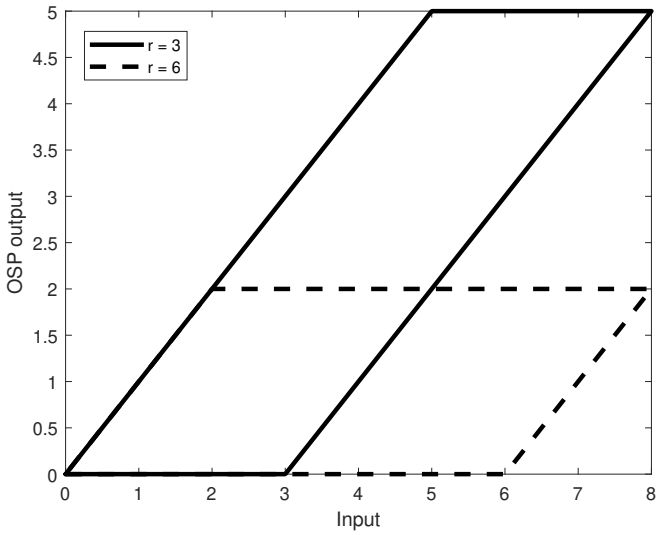

Figure 2.2: Input-output behavior of the OSP operator for different threshold values

OSP operator is in the $f_r(u, w)$ quantity which holds the following expression for the OSP operator.

$$f_r(u, w) = \max(u - r, \min(u, w)) \tag{2.4}$$

The PI model is simply a superposition of play-type operators and models a hysteresis curve $H(u)$. An expression for this model can be expressed as follows

$$H(u) = c_0 u + \sum_{r_1}^{r_N} c_i F_{r_i}[u](t) \tag{2.5}$$

Eq. (2.5) sums over N different threshold values and requires $N + 1$ coefficients that must be determined for accurate modeling of hysteresis. It should be noted that the number of coefficients needed to define a PI model is entirely problem dependent and a larger number of coefficients will provide a more accurate model for the hysteresis curve. In fact, if the distance between thresholds is chosen to be an infinitessimal distance, then Eq.(2.5) can be written as an integral as has been done in [35]. In fact, coefficient c_0 comes from the special case where $r = 0$. This is an important threshold value for hysteresis modeling as it represents

an hysteresis-free embedding function upon which the rest of the operators are overlaid onto. Without such an embedding curve, an inverse model may not be obtainable due to an inherent singularity. The major advantage to using an operator-based model such as the PI model is that it is easy to find optimal parameters procedurally. To do this, properties of the OSP operator are exploited. Firstly, as is shown in Fig, 2.4, the slope of the input-output curve before the threshold value is 0. Let $\boldsymbol{y}_m$ denote the set of measured output values. Let $\boldsymbol{c}$ and $\boldsymbol{r}$ denote the sets of PI coefficients and the set of threshold values respectively. The first step to modeling a hysteresis curve with the PI model is to select a suitable set of threshold values. The selection of these threshold values To procedurally obtain optimal PI model parameters, coefficients c_i are obtained sequentially starting with coefficient c_0. This coefficient scales a linear function in the input-output plane. It's important to note that before smallest threshold value $\min(\boldsymbol{r})$, no other operators contribute to the section of the curve in the input range of $[0, \min(\boldsymbol{r})]$ since before their threshold is reached, they hold the same value and have a slope of 0. The strategy to model the slope in this section then is to choose the coefficient such that it matches the slope of a linear regression. Let $\boldsymbol{r}$ be an ordered set such that $r_i < r_{i+1}$, $i > 0$. Let $\boldsymbol{u}_F \in \boldsymbol{u}$ be a subset of the input signal such that $u_f(t)$ is monotonically increasing or decreasing. The PI model parameters within the range of the input $u_f(t)$ can be determined as follows.

$$\boldsymbol{y}_m^{r_1} = \omega_0 + c_0 \boldsymbol{u}_F^{r_1} \tag{2.6}$$

$$\boldsymbol{y}_m^{r_{i+1}} = \omega_i + (c_i - \sum_{j=1}^{i-1} c_j) \boldsymbol{u}_F^{r_{i+1}} \tag{2.7}$$

Here, $\boldsymbol{y}_m^{r_i}$ refers to the output points associated to the input range $\boldsymbol{u}_F^{r_i}$ which is defined as $[\boldsymbol{u}_F(r_{i-1}), \boldsymbol{u}_F(r_i)]$. Eqs. (2.6) and (2.7) correspond to a linear regression between successive threshold values with intercept ω_i and a slope that depends on the PI coefficients. The

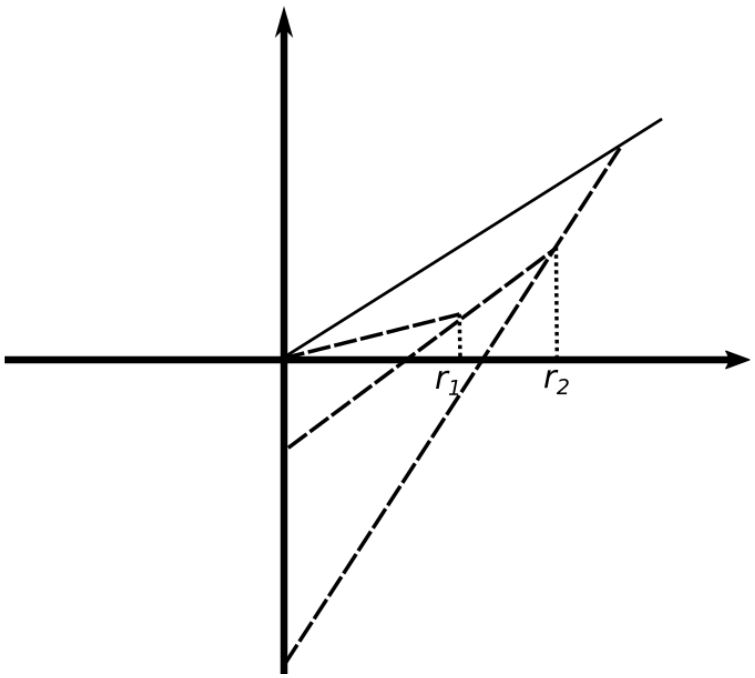

Figure 2.3: The PI model extrapolated into a series of linear functions

parameter estimation of N PI coefficients is reduced to N linear regression calculations.

The PI model possesses an analytical inverse that is itself a PI model. To obtain this inverse, it's useful to picture the PI model as series of linear functions. Fig. 2.3 shows an example of a 3 operator PI model with the linear functions that make up the curves extrapolated to the y-intercept. To construct the inverse geometrically, it is sufficient to find an inverse to all the line functions that make up the PI model.

Assume that $c_0 \neq 0$. This coefficient is associated to a linear curve whose intercept is at 0. The inverse coefficient c_0' can be expressed as follows.

$$c_0' = \frac{1}{c_0} \tag{2.8}$$

Eq. (2.8) corresponds to the special case where the associated threshold value is 0. This expression illustrates the requirement that $c_0 \neq 0$ if a well defined inverse is desired due to a

singularity that appears in Eq. (2.8) when $c_0 = 0$. To obtain a general expression for the inverse parameters of the PI model, an expression for the slopes of each linear segment as well as their y-intercepts is required. From Eq. (2.7), an expression for the slope m_j associated to the line function that occurs directly after the threshold r_j can be found as follows.

$$m_j = \sum_{i=1}^{j} c_j \tag{2.9}$$

To obtain the y-intercept value, a point on the line function can be found by considering the value of the PI model at a particular threshold r_j. An expression for this value $y_(r_j)$ can be expressed as follows.

$$y(r_j) = \sum_{i=1}^{j} c_i(r_j - r_i) \tag{2.10}$$

Eq. (2.9) and Eq. (2.10) generate a complete description of the linear functions that are implicit in the OSP operators. From these two equations, an expression for the y-intercept ω_j can be derived as follows.

$$\omega_j = -\sum_{i=1}^{j} c_i r_i \tag{2.11}$$

The linear function $f_j(u)$ associated to a specific threshold can be expressed using eqs. (2.9) and (2.11) as follows

$$f_j(u) = \sum_{i=1}^{j} c_i(u - r_i) \tag{2.12}$$

To invert the PI model, it is sufficient to choose OSP operators whose threshold apply to the output regime rather than the input regime and to invert the line function of Eq. (2.12). Inverse thresholds take the following form based on Eq. (2.10)

$$r'_j = \sum_{i=1}^{j} c_i(r_j - r_i) \tag{2.13}$$

From Eq. (2.12) and utilizing Eq. (2.9) to link linear slope with PI coefficients yields the following expression for inverse coefficients.

$$c_j' = \frac{c_j}{(\sum_{i=1}^{j} c_i)(\sum_{i=1}^{j-1} c_i)} \tag{2.14}$$

The ease of use of the PI model is apparent from the description as a series of truncated line segments. However, its description is inherently symmetric and frequency independent. For applications that do not have these properties such as PEA applications, it may be desirable to generalize the PI model to introduce these properties. For asymmetric extensions to the PI model, two common approaches are to either generalize the operator such that it is itself asymmetric or to modify the embedding non-hysteretic function such that the slope behavior in forward and backwards directions is different.

2.1.2 Jiles-Atherton Model

The Jiles-Atherton (JA) model is a differential equations-based model for hysteresis that was first introduced by Jiles and Atherton in 1984 to describe ferromagnetic hysteresis [20]. Unlike most other hysteresis models, the JA model was constructed from physical principles and is heralded as a physics-based modeling approach that is very popularly used in magnetic materials due to its description of useful physical parameters. In ferroelectric materials, The magnetization vector $\boldsymbol{M}$ varies with the magnetising field $\boldsymbol{H}$ and exhibits hysteresis in its description. A similar description exists in ferroelectric materials and acts as the electric analog to the ferromagnetic description. The JA description for ferroelectric materials was first described by Smith and Hom in 1999 [37]. It connects the polarization behavior of the ferroelectric material to the electric field.

In many cases, the material used to create PEA devices are ferroelectric in nature and this ferroelectricity is fundamentally the source of most of the hysteresis found in PEAs.

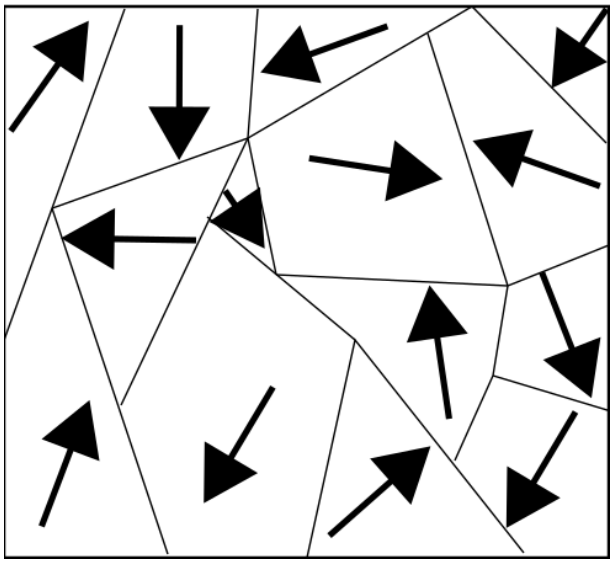

Figure 2.4: Example of ferroelectric domains oriented in different directions

The JA model provides a means to understand the underlying hysteresis present in PEAs more than other hysteresis models. The JA model describes objects within the ferroelectric called domains and details their interactions with each other as well as their response to electric fields. A domain is a cluster of unit cells within the ferroelectric crystal that share the same polarization direction $\boldsymbol{P}$. Fig. 2.4 shows an illustration of domains possessing different polarization orientations. The orientation of these domains yields a net polarization over the entire material. In a configuration such as that found in Fig. 2.4, the net polarization would be 0 since domains are distributed in random directions. However, if an electric field is applied to the material, then it can induce the reorientation of domains within the material to point in the same directions.

Two commonly used ferroelectric materials used in PEA devices are barium titanate (BTO) and lead zirconate titanate (PZT). The PZT unit crystal is shown in Fig. 2.5 and shows a perovskite structure with an inner Ti atom. Over the Curie temperature, the Ti atom only has a stable configuration at the center of the crystal. Under the Curie temperature, the Ti molecule can remain off center resulting in a net polarization. The movement of this

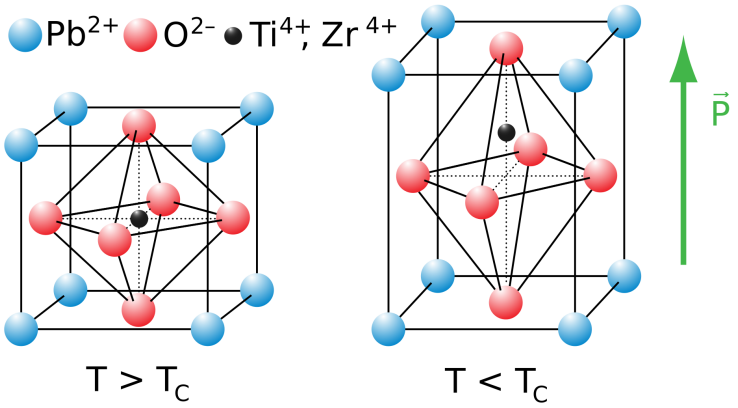

Figure 2.5: The unit crystal of PZT over and under the Curie temperature [1].

Ti atom within the unit cell stretches the unit cell in the same direction as the atom travels and provides a description of the piezoelectric effect.

The JA model is a semi-macroscopic model of the polarization within the ferroelectric since it describes groups of microscopic molecules and their collective behavior rather than their individual behavior. Consider first the interaction of a ferroelectric crystal of polarization P in the presence of an electric field $\boldsymbol{E}$ above its Curie temperature T_C. Above T_C, the unit cells within are polarizable but do not hold a net polarization if the electric field is turned off. A description for the potential energy U of a cell with a dipole moment $\boldsymbol{p}_0$ within an electric field can be described as follows[37]

$$U = -\boldsymbol{p}_0 \cdot \boldsymbol{E} = -p_0 E \cos(\theta) \tag{2.15}$$

Considering the behavior of a large number of cells provides statistical behavior that corresponds to perceived macroscopic behavior. A physical description for a system with a large number of distinct particles contributing some energy to the system is Boltzmann statistics which expresses the probability that particles the system occupy certain energies.

The probability $\rho(U)$ that a cell occupies an energy U is described as follows.

$$\rho(U) = Ce^{-U/kT} \tag{2.16}$$

Where k is the Boltzmann constant, T is the temperature, and C is a normalization coefficient that normalizes the probability to 1. Assume a simplified model of polarization such that it can occupy two distinct states, namely up and down. This two state system is commonly referred to as the Ising model first described in the 1920s [60]. Assume N_+ cells are oriented in the direction of the electric field and N_- cells are oriented in the opposite direction. The total number of cells can be determined by the following expression.[37]

$$N = N_+ + N_- \tag{2.17}$$

N_+ and N_- define situations in which $\theta = 0$ and $\theta = \pi$ respectively. Utilizing the expression in Eq. (2.16) and combining it with Eq. (2.17) and Eq. (2.15) yields the following

$$N = Ce^{-p_0E/kT} + Ce^{p_0E/kT} = 2C\cosh(\frac{p_0E}{kT}) \tag{2.18}$$

A description of the total polarization P can be found by counting the number of cells in the positive direction and subtracting them with the number of cells in the negative direction as described as follows.

$$P = p_0N_+ - p_0N_- = 2p_0C\sinh(\frac{p_0E}{kT}) \tag{2.19}$$

Combining Eq. (2.18) with Eq. (2.19) yields the following expression for the macroscopic polarization

$$P = p_0N\tanh(\frac{p_0E}{kT}) \tag{2.20}$$

Eq. (2.20) provides a description of the behavior of a polarizable material if its constituent cells only interact with the electric field. In reality, cells interact with each other as well and not only the external electric field dictates the local field perceived by the cell. A useful quantity to describe the true field that an average cell is interacting with is the effective field E_e which considers interactions from other neighbouring cells. An expression for the effective field is given as follows.

$$E_e = E + \alpha P \tag{2.21}$$

Where α is a positive coefficient referred to as the domain interaction parameter. Stronger values are associated to stronger neighbouring interactions and coupling inside the material. If all cells are oriented in the same direction, they reach a saturated state in which adding extra energy via electric fields cannot reorient additional particles within the material. This state is called the saturation polarization P_s and can be described as follows

$$P_s = Np_0 \tag{2.22}$$

Additionally, for constant temperatures, a parameter $a = kT/p_0$ is defined called the shape parameter. Eq. (2.20) in terms of the newly defined parameters and by replacing the electric field by the effective electric field as follows.

$$P_{an} = P_s \tanh(\frac{E + \alpha P}{a}) \tag{2.23}$$

Eq. (2.23) is referred to the anhysteretic polarization P_{an} and quantifies the behavior of a ferroelectric material when it is free of hysteresis. This situation arises when the temperature of the crystal is above the Curie temperature. Characterization of parameters P_s, a, and $alpha$ can be done under these conditions directly. Under the Curie temperature, the polarization state of a cell can retain some memory of the electric field and retain a net polarization with

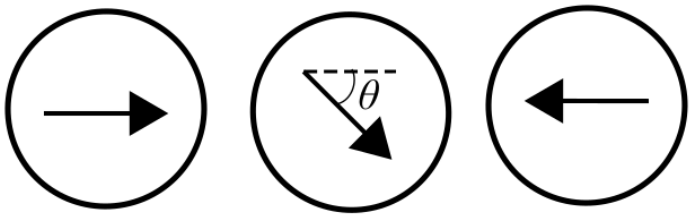

Figure 2.6: Diagram of domain rotations. The left image is the initial orientation. The middle image represents a rotation of θ. The right image is a rotation of π

no external field present. In the JA model, this effect is modeled by introducing pinning sites which constrain the walls of the domains and require an expenditure of energy to break. This energy requirement to break pinning sites acts as a loss and describes an irreversible process. Microscopically, the pinning sites can be any material defect either intentionally (for example, doping agents) or unintentionally added to the material (cracks or voids). The domain walls can exhibit reversible and irreversible dynamics.

To describe the energy required to break pinning sites, it is assumed that the energy requirement is proportional to the energy required to rotate a domain. Fig. 2.6 shows the rotation range of a domain. The configuration requiring the least amount of energy is a rotation of 0. The maximal required energy is associated to a rotation of π.

It can be shown that the energy required to break a pinning site U_p can be expressed as a function of the energy required to rotate the domain by π, U_π as follows

$$U_p = \frac{1}{2} U_\pi (1 - \cos\theta) \tag{2.24}$$

The energy required to break the pinning sites of of a domain depends on the overall size of the domain as well as the average volumetric density of pinning sites, n. The energy required to break pinning sites for a domain of area A moving a distance of x can be expressed

as the following integral.[37]

$$U_p = \int_0^x \frac{nU_\pi}{2}(1-\cos\theta)Adx' \tag{2.25}$$

The change in polarization can be expressed by adding a dipole moment p to parts of the integral of Eq. (2.25) as $dP = p(1-\cos\theta)Adx$. From this, the pinning coefficient $k = nU_\pi/2p$ can be defined and the energy required to break pinning sites as a function of polarization is given as follows by noticing that the expression within the integral has units of polarization.

$$U_p(P) = k\int_0^P dP' \tag{2.26}$$

Eq. (2.26) provides a description of an irreversible energy loss whereas an idealized lossless energy process can be described by integrating the anhysteretic polarization found in Eq. (2.23) with the effective electric displacement D_e. The total energy is described as the sum of the lossless energy from the anhysteretic case and the lost energy generated by the irreversible case. An integral equation can be derived combining the irreversible polarization P_{irr}, anhysteretic polarization, by substituting the integration variable in Eq. 2.26 to depend on D_e.

$$\int_0^{D_e} P_{irr}(E_e)dD'_e = \int_0^{D_e} P_{an}(E_e)dD'_e - k\varepsilon_0\int_0^{D_e}\frac{dP_{irr}}{dD'_e}dD'_e \tag{2.27}$$

Since the integration is on the same domain, integrals can be cut and a differential equation can be written for P_{irr}. The differential component of P_{irr} can become positive if the electric field decreases since the derivative term becomes negative. This situation is not possible since P_{irr} is purely dissipative. The addition of a factor $\delta = \text{sign}(dE)$ ensures that this quantity is always negative. Eq. (2.27) becomes the following.

$$P_{irr}(t) = P_{an}(t) - \varepsilon_0 k\delta\frac{dP_{irr}(t)}{dD_e} \tag{2.28}$$

Using the definition of $D_e = \varepsilon_0 E + \alpha P$, the differential equation of Eq. (2.28) can be expressed in terms of the electric field as follows.

$$\frac{dP_{irr}(t)}{dE(t)} = \frac{P_{an}(t) - P_{irr}(t)}{k\delta - \alpha(P_{an}(t) - P_{irr}(t))} \tag{2.29}$$

The final component required for a complete description of the JA model is a reversible component. The motion of domain walls is complex and many movement modes do not lose energy. Jiles and Atherton took into account the effect of domain wall bowing in response to the pressure induced by the electric force [20]. However, a simpler description can be derived by considering two collective processes. Eq. (2.29) includes all dissipative contributions. The total polarization can be expressed as a sum of reversible and irreversible components as follows.

$$P(t) = P_{irr}(t) + P_{rev}(t) \tag{2.30}$$

Meanwhile, in the absence of irreversible components, the total polarization would reach the ideal anhysteretic case P_{an}. An expression for P_{an} can be created using a parameter $c \in [0, 1]$ acting as a ratio.

$$P_{rev}(t) = c(P_{an}(t) - P_{irr}(t)) \tag{2.31}$$

These derivations were inspired by the works of RC Smith on the extension of the Jiles-Atherton model into the ferroelectric domain in [37] and [61]. Combining eqs. (2.23), (2.29), (2.30), (2.31) can yield a single differential equation that describes the JA model as follows.

$$\frac{dP}{dt} = \frac{dE}{dt} \frac{1}{1 - \frac{cP_s\alpha}{a}\text{sech}^2(\frac{E+\alpha P}{a})} \left(\frac{P_{an} - P}{k\delta - \frac{\alpha}{1-c}(P_{an} - P)} + \frac{cP_s\alpha}{a}\text{sech}^2(\frac{E + \alpha P}{a}) \right) \tag{2.32}$$

To find the inverse of the JA model established in Eq. (2.32), the model is expressed as a

function of E and P parameters

$$\frac{dP(t)}{dt} = \frac{dE(t)}{dt} F(E(t), P(t)) \tag{2.33}$$

with

$$F(E,P) = \frac{1}{1 - \frac{cP_s\alpha}{a}\mathrm{sech}^2(\frac{E+\alpha P}{a})} \left(\frac{P_{an} - P}{k\delta - \frac{\alpha}{1-c}(P_{an} - P)} + \frac{cP_s\alpha}{a}\mathrm{sech}^2(\frac{E+\alpha P}{a}) \right) \tag{2.34}$$

The inverse model that yields an inverse polarization P' can be expressed as follows[62]

$$\frac{dP'}{dt} = \frac{\frac{dE}{dt}}{F(P', E)} \tag{2.35}$$

The JA model is complicated compared to other models due to its physical derivation. However, it has the advantage that all parameters used within have a physical interpretation that can in theory be used to measure parameters from experiments. In practice however, these parameters are not typically easy to obtain especially in commercial systems and they are normally only mentioned during physical characterization of ferroelectric materials. It should also be noted that the hysteresis model describes the hysteresis between polarization and electric field as opposed to the hysteresis between displacement and voltage typically seen in PEAs. Nevertheless, the JA model is capable of describing the hysteresis between displacement and voltage of PEA systems well but the physical significance of the parameters is no longer retained in this process. The link between polarization and displacement is not obvious but if an expression is known, then the JA model could also provide a physical model for piezoelectric hysteresis as well. However, this approach is not attempted in this dissertation and hysteresis between displacement and voltage modeled with the JA model are phenomenological.

2.1.3 Bouc-Wen Model

The Bouc-Wen (BW) model is another differential-equations-based model that was first described by Bouc in 1971 and later extended by Wen in 1976. It represents a phenomenological model of hysteresis that is based on the mechanical description of the system. The BW model considers the problem of modeling hysteresis in a system through a nonlinear restoring force that has a hysteretic component as well as a non-hysteretic component. For low frequency applications and high stiffness PEA systems, the dynamics of the PEA can be approximated to behave as follows.

$$y = d_p u - z \tag{2.36}$$

Where d_p is the piezoelectric coefficient, y is the output position, u is the input voltage, and z is a hysteretic component that characterizes the BW model and takes the following differential form.[59]

$$\dot{z} = \alpha\dot{u} - \beta|\dot{u}|z|z|^{n-1} - \gamma\dot{u}|z|^n \tag{2.37}$$

Where parameters α, β, γ, and n are coefficients that adjust the shape of the hysteresis curve. The BW model is one of the most popular differential equations-based models found in the literature due to its simplistic formulation and its ability to describe a wide range of hysteresis shapes. Physical interpretation of BW parameters is less clear than other models but from Eq. (2.37), it is clear that α serves the purpose of a regular restoring force that works against the regular restoring force. In the event that $\alpha < d_p$, the output increases when the input increases and vice-versa. In the event where $\alpha > d_p$, the output is inverted in regard to the input. In the case that $\alpha = d_p$, the curve initially varies little before reaching a threshold similar to those seen in the PI model. Fig. 2.7 shows these three situations for a BW curve generated with $\beta = \gamma = d_p = n = 1$. Two distinct regions appear in the hysteresis curve. Initially, the hysteresis curve has a slope that is characterized mainly by α and $\dot{p}$.

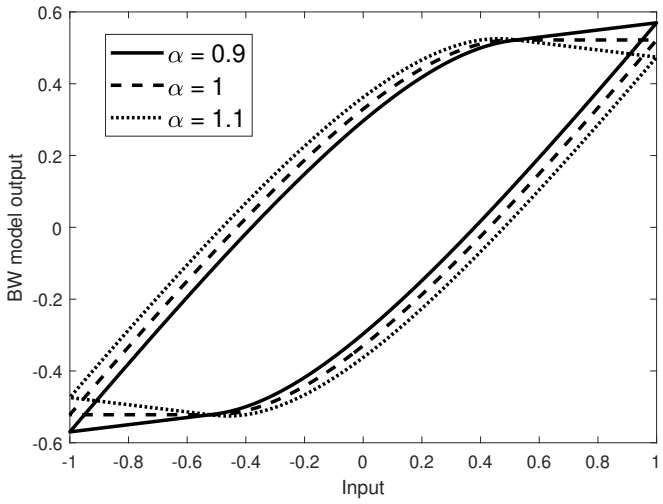

Figure 2.7: Three examples of BW hysteresis. $\alpha = 0.9$ represents a case where $\alpha < d_p$, $\alpha = 1$ represents a case where $\alpha = d_p$, and $\alpha = 1.1$ represents a case where $\alpha > d_p$

Later on, the output begins to increase at a faster rate even in the situation where $\alpha =$. In this sense, the BW model gives a smooth description of a bi-linear model. Parameters β and γ are more difficult to characterize but their value affects the shape of the hysteresis. Parameter n is often associated with the elastic to plastic transition. Larger values of n have more abrupt transitions. For this reason, when modeling PEA systems, this parameter is often chosen such that $n = 1$ to ensure smooth curves found in practice.

An inverse model for the BW model can be found by studying the structure of the BW model. Fig. 2.8 shows a block diagram model that generates an inverted signal for a BW modeled system. Let y_r refer to the reference signal, u the input to the PEA, y the PEA output, and $H(u) = z(u)$ as defined by Eq. (2.37). From figure 2.8, u can take the following form

$$u = \frac{y_r}{d_p} + \frac{H(u)}{d_p} \tag{2.38}$$

Once the signal expressed by Eq. (2.38) reaches the PEA, it is transformed into the

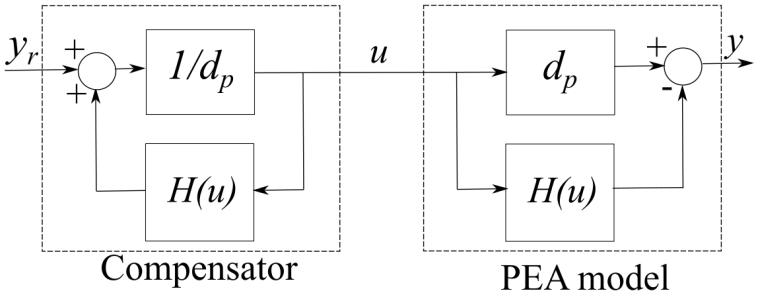

Figure 2.8: Block diagram of BW compensator

output y using Eq. (2.36) and yields the following

$$y = y_r + H(\frac{y_r}{d_p} + \frac{H(u)}{d_p}) - H(\frac{y_r}{d_p} + \frac{H(u)}{d_p}) = y_r \tag{2.39}$$

From Eq. (2.39), it is clear that the process shown in Fig. 2.8 generates an inverse model for the BW hysteresis curves.

2.2 Hysteresis Compensation

In the previous section, three models have been introduced as hysteresis models. However, it is unclear how the compare in the compensation of PEA hysteresis. In this section, compensators are designed and their performance in linearizing the PEA output is examined. Additionally, two different PID controllers are designed and their performance coupled with the proposed compensators are assessed.

2.2.1 Experimental System

To perform experiments to compare hysteresis models, The P-753.1CD LISA actuator and stage designed by Physik Instrumente is used as the PEA system. This actuator is equipped with a precise capacitive sensor with a resolution of 0.1 nm. To power the system, the E-625

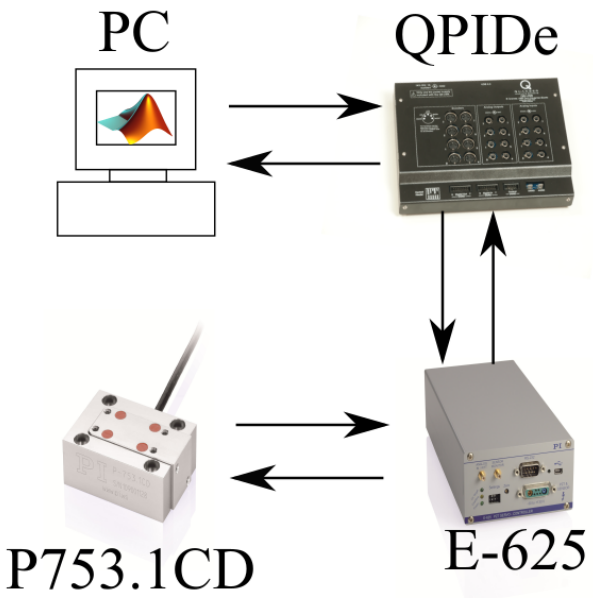

Figure 2.9: Experimental system consisting of a PC running simulink, the QPID-e, the E-625, and the P753.1CD

piezo-servo controller from Physik Instrumente is utilized in open loop mode. This mode of operation acts as an amplifier and provides an amplification of 10x over the input signal. The input signals are generated by the Quanser QPIDe data acquisition device. The QPIDe has an input/output range of -10V - 10V allows for reading the position sensor as well as writing the input signal at 16 bits of resolution. Experiments are conducted at 10 kHz. The QPIDe has the capability of real-time hardware in the loop experiments coupled with the MATLAB Simulink software. Fig. 2.9 shows a diagram of these system components. The Simulink-equipped PC sends model commands to the QPIDe and receives sensor readings from it. The QPIDe sends control commands to the E-625 amplifier and receives calibrated capacitive sensor data from it. Finally, the E-625 amplifier sends amplified control commands to the P-753.1CD and receives the raw sensor data.

In tracking experiments, the PEA output is required to track a reference signal as closely as possible. Experiments must have a defined reference to accomplish this task. Two reference signals are assessed, namely a sinusoidal signal and a triangle wave pattern. Due to the

P-753.1CD being a unipolar actuator with a smaller range of acceptable negative inputs, reference signals should avoid being negative to allow for a greater range of control corrections in this range. The sine wave reference input y_r^s can be written as follows

$$y_r^s(t) = A + A\sin(2\pi ft - \pi/2) \tag{2.40}$$

Where A is the amplitude of the signal and f is the frequency. Similarly, the triangle wave reference $y_r^t(t)$ can be expressed with the same parameters as follows

$$y_r^t(t) = 4A|ft - \lfloor ft + \frac{1}{2}\rfloor| \tag{2.41}$$

Fig. 2.10 shows both varieties of reference signals for $A = 3$ and $f = 5$ Hz. The amplitude was chosen such that a large range of the PEA system can be traveled while also allowing some margin for control inputs to go over or under. The frequency of 5 Hz is chosen so that the frequency is high enough such that the effect of creep is not important in the measurements while being slow enough such that the dynamic effects in the PEA can be neglected. It should be noted that most hysteresis models are frequency independent and require modification to describe frequency dependent effects. In PEAs, the hysteresis curves broaden when the frequency is increased. Hence, to compare these models, maintaining the same frequency is desirable. Parameters for models are estimated by optimizing a fitness function. The least squares method is utilized to generate this fitness function of value S and is defined as follows.

$$S = \sum_{i=1}^{N}(y(t_i) - y_m(t_i))^2 \tag{2.42}$$

Where $y(t_i)$ is the output of the PEA at a time t_i and $y_m(t_i)$ is the model output at the same time. This fitness function is essentially a sum of the model error over the open loop data collected. Better agreement equates to smaller errors for all time instants t_i and thus a

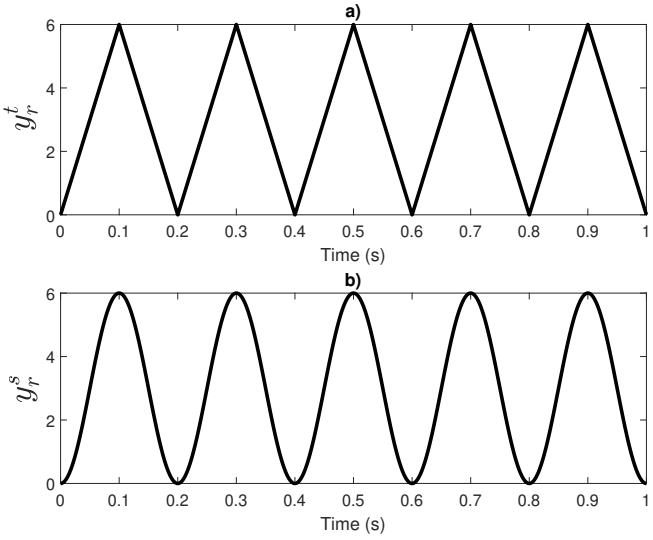

Figure 2.10: Reference signals for tracking experiments. a) Triangle wave with $A = 3$ and $f = 5Hz$. b) Sine wave with $A = 3$ and $f = 5Hz$

smaller value for S. For the BW and JA models, it is difficult to have an idea of optimal parameters a priori and thus an optimization algorithm is normally utilized to find suitable parameters. For the PI model, coefficients possess a geometrical interpretation and can be calculated directly for one side of the hysteresis curve optimally by using Eqs. (2.6) and (2.7) However, due to the symmetric nature of the PI model and the asymmetric nature of the PEA hysteresis, the fit is only optimal for one side of the hysteresis curve and not for the other side. If more accurate modeling is needed, symmetric PI models can be used and some appear in this work in later sections.

2.2.2 Feedforward Compensation

Feedforward compensation of a system involves a control component that remains open due to not requiring the measurement of the process while it is being run. This method typically involves a model of the plant under consideration and seeks to shape the input in a pre-defined way. Feedforward components are very useful in PEA systems to help remove detrimental

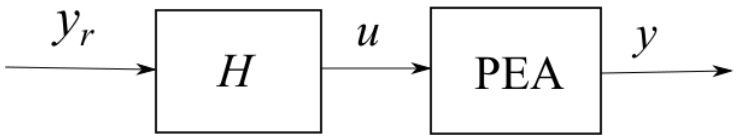

Figure 2.11: Feedforward compensator block diagram

nonlinear effects that are difficult for certain control systems to deal with on their own. This is the case for hysteresis which affects the way the input affects the output depending on the direction it is going in. To solve this with a linear controller is not easily achieved without changing the gains during the process. However, if the problematic non-linearity is removed from the system through modeling, then the system behaves like a linear system and the controller can perform its task more effectively.

To examine compensator performance in effectively canceling PEA hysteresis, a feedforward compensator is attached to the input and fed into the PEA system. The block diagram of this compensator is shown in Fig. 2.11. Compensators are designed for the JA, BW, and PI models. The JA compensator is designed according to Eq. (2.35). The BW compensator is designed based off the process shown in Fig. 2.8. The PI compensator is calculated based off the model parameters calculated from Eqs. (2.6) and (2.7). From these parameters, an analytical inverse model is generated with inverse parameters calculated using the process indicated in Eqs. (2.13), (2.14).

Experiments are conducted over both reference signals shown in Fig. 2.10 and defined in Eqs. (2.40) and (2.41). Figs. 2.15 and 2.16 show compensator performance in the input-output plane for the BW, JA, PI, and uncompensated compensators. Fig. 2.12 shows the model fit of the BW model compared to the PEA hysteresis while Figs. 2.13 and 2.14 show similar plots but related to the JA and the PI model respectively. In all three cases, it can be seen that the models are in good agreement with the measured hysteresis in the system. However, it can be seen that the PI model is inaccurate on one side of the hysteresis curve.

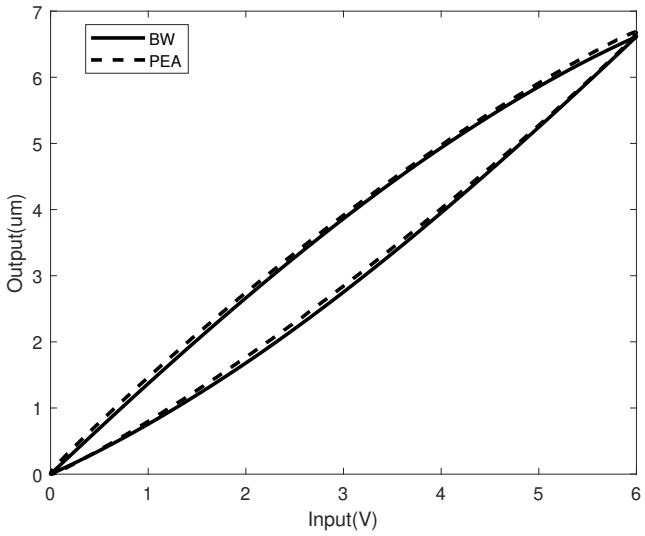

Figure 2.12: BW model compared to PEA hysteresis

Table 2.1: BW model parameters and fitness function result

α	0.6187	β	0.2418
γ	0.0237	n	1
d_p	1.6126	Fitness	7.59

This is due to the hysteresis being asymmetric and a better agreement could be obtained if the PI model was made asymmetric. In Chapter 5 of this dissertation, the classical PI model in this section is modified to create asymmetric curves but the classical model was kept in this section as an unmodified variant that was built upon. Tables 2.1, 2.2, and 2.3 show the parameters used in the BW, JA, and PI models respectively as well as their fitness function value. The JA model yields a slightly better agreement compared to the PI model and BW model. The PI model has the worst agreement due to the fitting process being one-sided rather than two sided. Though if models are compared on one side, the PI model has the best agreement due to being optimal.

The compensated output for a 5 Hz sine wave can be found in Fig. 2.15 and the compensated output for a 5 Hz triangle wave can be found in Fig. 2.16. These plots are

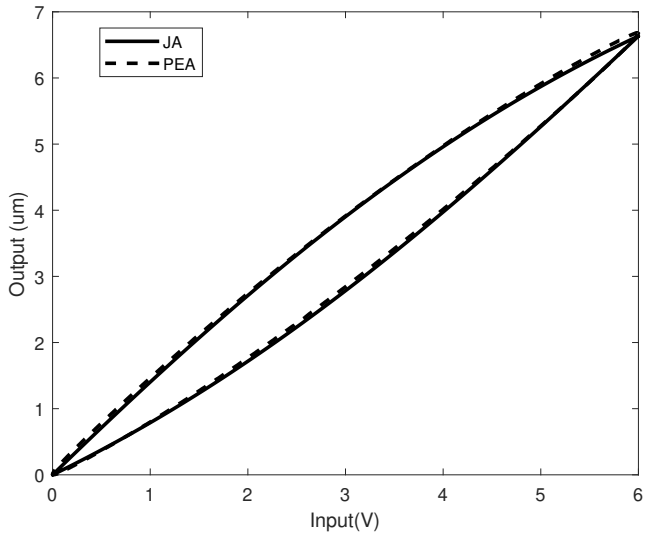

Figure 2.13: JA model compared to PEA hysteresis

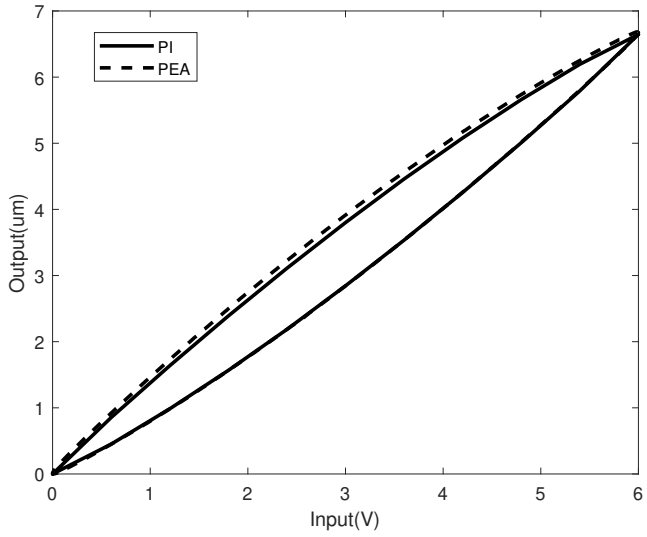

Figure 2.14: PI model compared to PEA hysteresis

Table 2.2: JA model parameters and fitness function result

P_s	55.9973	α	0.2512
a	48.5843	k	3.8892
c	0.6929	Fitness	6.04

Table 2.3: PI model parameters and fitness function result

c_0	0.7521	c_1	0.1381	c_2	0.0775	c_3	0.0651
c_4	0.0658	c_5	0.0522	c_6	0.0506	c_7	0.0523
c_8	0.0520	c_9	0.1169	r_i	$0.6i$	$Fitness$	14.6312

plotted in the input/output plane and PEA input is based on the compensator shown in Fig. 2.11. Better agreement is characterized by how linear the graph is in appearance. For the sine wave case, it can be seen that the JA model and the BW model yield good linearity compared to the compensated case while the PI model retains a small amount of hysteresis in its plot. For the triangle wave case, the JA and BW model perform slightly worse than the PI model case. The difference between these two situations may be due to the shape of the input. The sine wave represents a pure frequency component whereas the triangle wave is a superposition of multiple frequencies. The rate dependent nature of the PEA hysteresis makes these two scenarios slightly different and thus the performance can also be altered. Despite these differences, all three modeling approaches yield much better linearity than in the uncompensated case.

Figs. 2.17 and 2.18 show the resulting error from the feedforward compensators. The error $e(t)$ are calculated based on the following equation.

$$e(t) = y(t) - y_r(t) \tag{2.43}$$

In the uncompensated case, large errors up to 1 um are present in the output which are reduced significantly with all three models. Maximum and minimum errors for the sine wave case can be found in Table 2.4. It can be seen that the BW has the best peak-to-peak error and also the most symmetric around 0. The JA model tends to underestimate positioning more than it overestimates whereas the PI model tends to overestimate rather than underestimate. The uncompensated performance tends to overestimate much more than

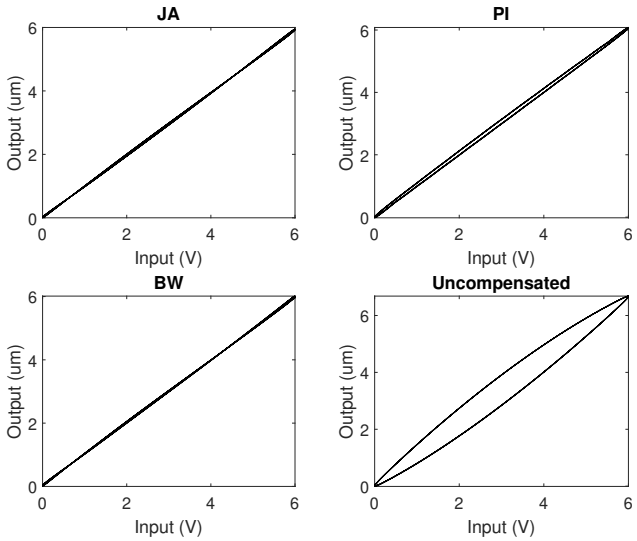

Figure 2.15: Feedforward compensator performance for a 5 Hz sine wave signal comparing linearized performance between the models

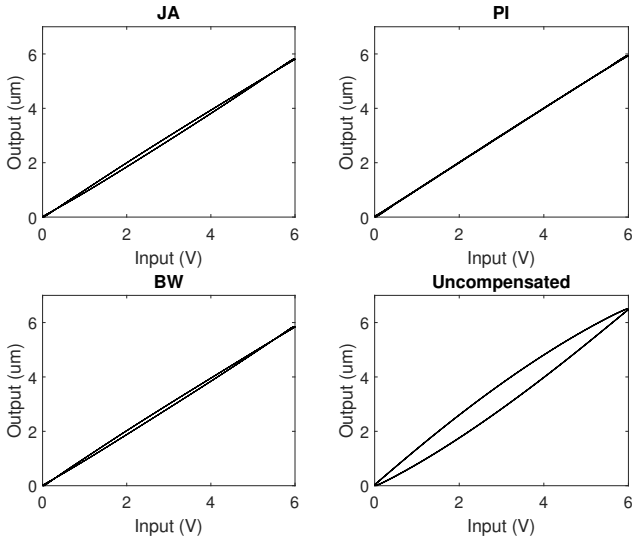

Figure 2.16: Feedforward compensator performance for a 5 Hz triangle wave signal comparing linearized performance between the models

Table 2.4: Peak errors above and below 0 for a sine wave in the Feedforward configuration

Model	Peak error above 0 (um)	Peak error below 0 (um)
BW	0.0428	-0.0623
JA	0.0229	-0.1070
PI	0.1546	-0.0239
Uncompensated	0.9670	-0.2281

Table 2.5: Peak errors above and below 0 for a triangle wave in the Feedforward configuration

Model	Peak error above 0 (um)	Peak error below 0 (um)
BW	0.0229	-0.1641
JA	0.0162	-0.1951
PI	0.0213	-0.0744
Uncompensated	0.8057	-0. 2473

underestimate though all models improve these aspects considerably. For the triangle wave case, Table 2.5 shows the error peaks of the resultant compensated output of the PEA system based on the tested compensators. In this experiment the PI model outperforms the rest.

The error graphs presented show that compensators are capable of reducing error in both the triangle wave and sine wave reference signals. However, it is interesting to examine the errors more closely to compare their profiles. It is also noted that little vibration is present in the feedforward errors. This is due to the high stiffness of the PEA requiring a lot of energy to generate vibrations in the material which are quickly dissipated from the damping. A Fourier transform is conducted on the errors from Figs. 2.18 and 2.17. The results of this Fourier transform can be found in Fig. 2.19 for triangle waves and 2.20 for sine waves with intensity referring to the magnitude of the error with units of um. The results of these plots show that the differential equations-based models contain fewer peaks above 5 Hz compared to the PI model. The reason this occurs is that the differential equations-based models produce smooth curves whereas the operator-based models are not necessarily smooth. In the PI model, the OSP operator is not smooth and thus the shape of its curve can generate higher

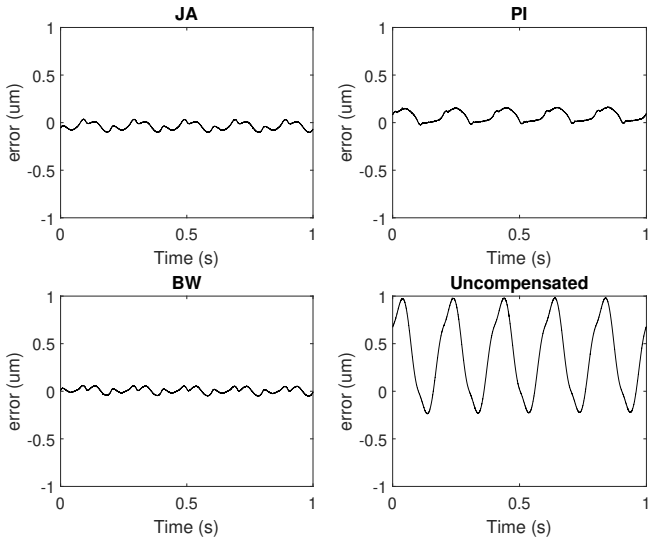

Figure 2.17: Feedforward compensator error for a 5 Hz sine wave signal comparing tracking accuracy between the models

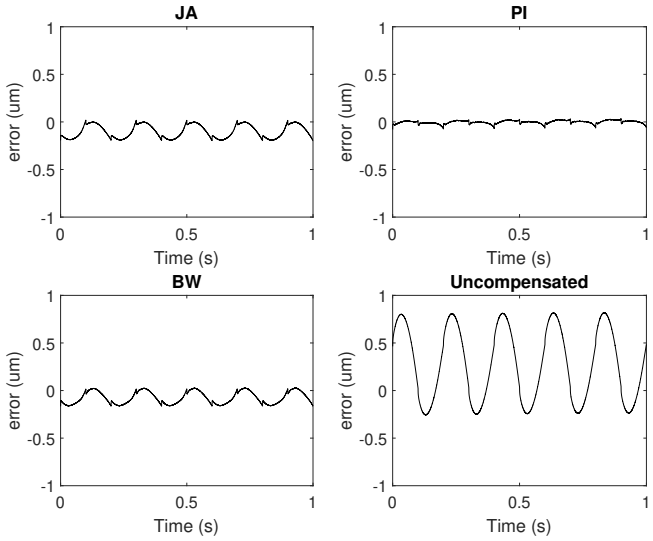

Figure 2.18: Feedforward compensator error for a 5 Hz triangle wave signal comparing tracking accuracy between the models

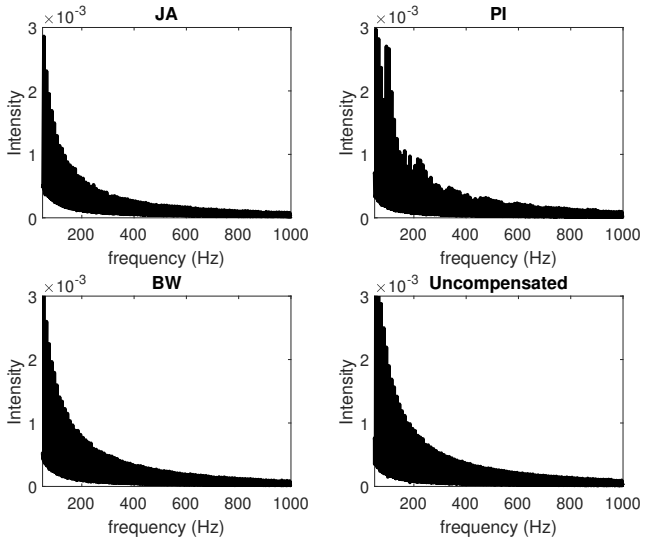

Figure 2.19: Frequency distribution of triangle wave errors comparing noise spectrum between the models

frequency modes due to abrupt changes in input slope.

2.3 Proportional Integral Control

While feed forward control can improve the tracking performance of PID systems, they possess several disadvantages compared to feed back controllers that are difficult to overcome in purely feed forward designs. The main problem with the approach is that any modeling errors that are present in the feedforward controller will generate a disturbance in the tracking performance of the PEA and there is no way to correct for these disturbances during the process. Also, should an unpredictable disturbance impede the movement of the PEA system, most feedforward approaches would not be able to react and thus errors may accumulate after prolonged periods.

In most situations, a controller with a feedback component is desirable to increase robustness to disturbances and require less complicated modeling to solve the same problem. One of the simplest and most widely used control strategies is the proportional-integral-

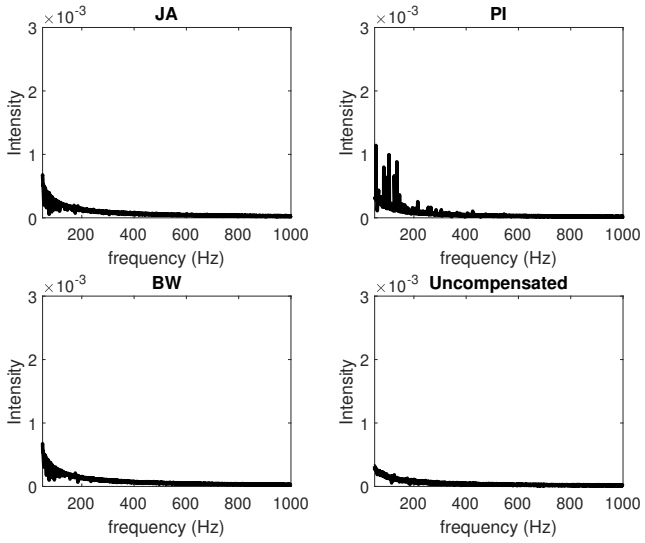

Figure 2.20: Frequency distribution of sine wave errors comparing noise spectrum between the models

derivative (PID) control strategy. The principles of PID control are to control the process with an input that is a function of the error between a reference signal and the measured output value. The control input takes the following form.[63]

$$u(t) = K_p e(t) + Ki \int_0^t e(t')dt' + K_d \frac{de(t)}{dt} \tag{2.44}$$

Where K_p, K_i, K_d are control gains for the proportional, integral, and derivative component respectively. PID controllers are reactive linear controllers that do not require knowledge of the system to act as a controller. However, improper selection of PID parameters can lead to poor control performance and instability. For nonlinear systems, the PID controller will not perform as well by itself compared to if the system was linear because the system dynamics do not behave in the linear and symmetric way that the controller does. Therefor, if the system is linearized, it can be expected that the PID controller will perform better. There are different strategies to adapt PID controllers to nonlinear systems such as gain scheduling or adaptive control strategies. PID controllers work well with feedforward components that

seek to address some of the weaknesses of the PID control strategy by linearizing the system through compensating the major nonlinearities. To examine the performance of a PID controller, a linear model of the plant dynamics is needed to assess performance. The PEA system can be modeled at typical second-order mechanical system described as follows.

$$m\ddot{x}(t) + c\dot{x}(t) + kx(t) = u(t) \tag{2.45}$$

Where m, c, k are the effective mass, effective damping, and the effective stiffness coefficients of the PEA system. The PEA is cascaded with the E-625 piezoamplifier which itself imparts onto the system its own second order dynamics. A transfer function $G(s)$ for the PEA in series with the amplifier can be written as a 4th order system as follows

$$G(s) = \frac{k_a\omega_a^2}{s^2 + 2\zeta_a\omega_a s + \omega_a^2} \cdot \frac{k_p\omega_p^2}{s^2 + 2\zeta_p\omega_p s + \omega_p^2} \tag{2.46}$$

Where ω_a is the amplifier natural frequency, ω_p is the PEA natural frequency, ζ_a is the amplifier damping factor, and ζ_p is the PEA damping factor. System identification can be performed on the PEA-amplifier system using a chirp signal of low input magnitude and the following 4th order transfer function is found to adequately model the system.

$$G(s) = \frac{1.377 \times 10^{16}}{s^4 + 2.813 \times 10^4 s^3 + 5.403 \times 10^8 s^2 + 4.981 \times 10^{12} s + 1.822 \times 10^{16}} \tag{2.47}$$

Fig. 2.21 shows the frequency response of the PEA cascaded with the amplifier as well as the modeled frequency response according to Eq. (2.47). It can be seen that $G(s)$ is a suitable model for the system and controller analysis can be performed on it. However, it should be noted that the system resembles a second order system and could have been modeled this way due to the gains in the first and second order being several magnitudes

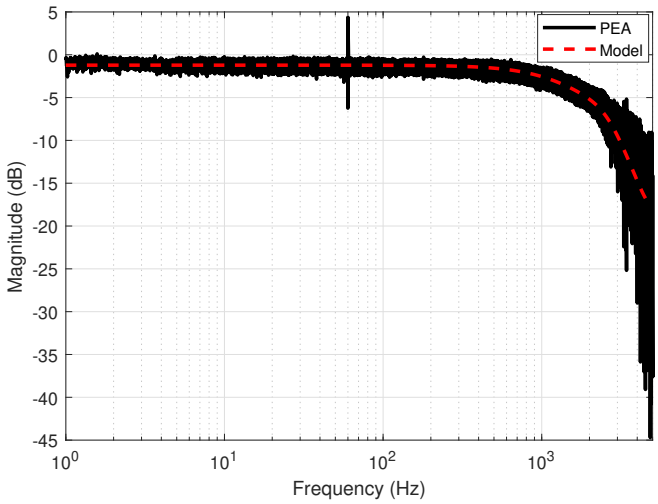

Figure 2.21: Frequency response of the PEA system compared to a 4th order linear plant model described in Eq. 2.47

higher than the higher order gains. The frequency range was not large enough to capture any resonance peaks making the estimates for the higher orders possibly inaccurate. A PID controller is placed in series with the PEA system and multiplies onto $G(s)$ the following transfer function $C(s)$.

$$C(s) = \frac{K_d s^2 + K_p s + K_i}{s} \tag{2.48}$$

The three gains in the PID controller serve different purposes. The P gain will generate a control response that directly proportional to the error and has the advantage of being fast acting. However, the P term cannot eliminate steady state errors on its own. The I gain adjusts its contribution to the control response over time and is capable of eliminating steady state errors in the system. However it can slow down response of a system to undesirable levels. The D term generates higher signal strengths if the change in error at an instant in time is larger. This component is useful to eliminate overshoots in the control performance by penalizing large velocities in the control response. One major drawback of the D term is that it can add noise to the system due to it being based on differentiation. High frequency

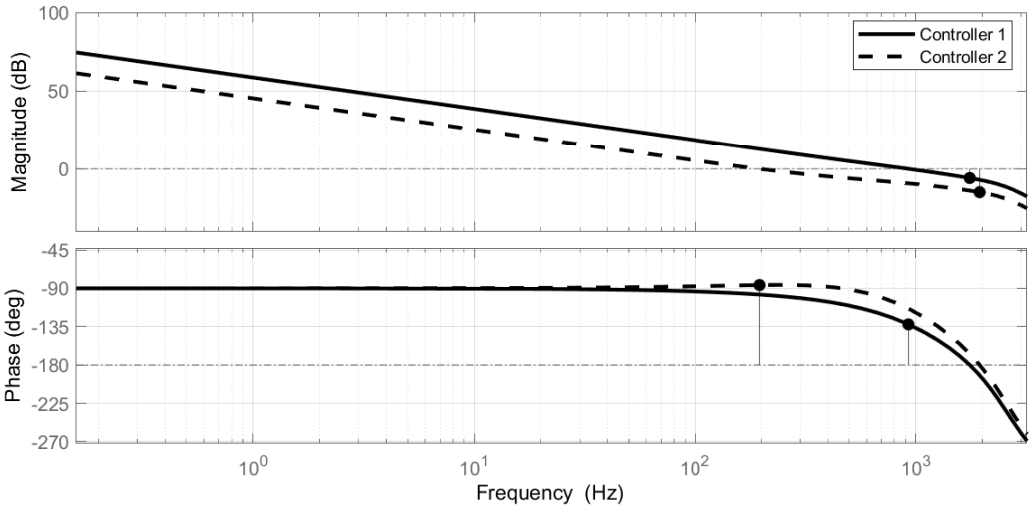

Figure 2.22: Bode diagram of PI controllers applied to $G(s)$ with indicated gain and phase margins. Controller 1 shows a higher bandwidth but lower gain and phase margin.

Table 2.6: Controller gains

Controller	K_P	K_I
controller 1	1.207	7009
controller 2	0.5265	1521

noises within the system will become amplified due to their high rate of change in the error.

For PEAs, a PI controller is usually suitable for as a closed-loop controller in which the D gain is chosen to be 0. This term adds damping to the controlled system which is not necessary for the PEA which has a very fast response. Additionally, a derivative on error amplifies errors which can be counterproductive to the control goals. Two different PI controllers are designed to control the PEA system based on its system identification. Gains of these controllers are chosen such that they are stable and possess a different bandwidth and are found using Matlab's control system toolbox. Fig. 2.22 shows a Bode plot of two PI controllers of different gains such that their bandwidth is different. Controller 1 is a high bandwidth controller possessing a bandwidth of approximately 1.4 kHz while controller 2

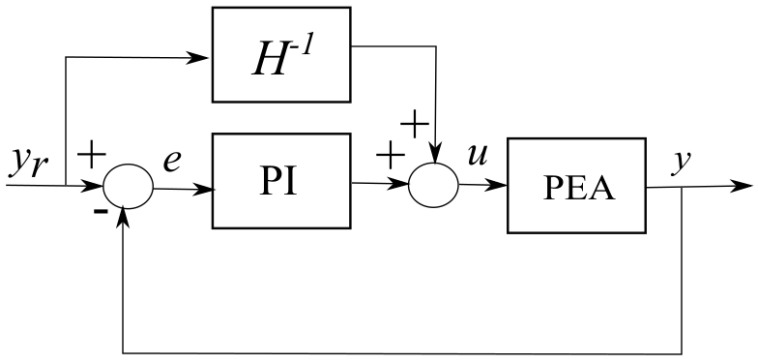

Figure 2.23: Block diagram of feedback-feedforward controller

has a lower bandwidth at approximately 320 Hz. Both controllers are stable with positive gain and phase margins as indicated by the black dots on the magnitude and phase plots. However, controller 2 is a more robust controller possessing a greater phase and gain margin than controller 1. Table 2.6 lists the gains used in both PI controllers.

The PI controllers are fundamentally working on a nonlinear model when controlling a PEA. Instead a feedforward component is added to the controller to compensate for the hysteresis in the system. Fig. 2.23 shows a block diagram of the controller in question. The H^{-1} term is the inverse hysteresis of the system and three models are compared in this slot. Namely, one created using the BW, PI, and JA models. Additionally, a situation where no model for hysteresis is provided. Figs. 2.24 and 2.25 show the error the two controllers for different compensators for sine wave signals. It can be seen that the error magnitude for all compensators is generally smaller than those found in the uncompensated case. However, the magnitude is only decreased by about a factor of 2 over the uncompensated controller in controller 1. Also, in controller 2, the difference between the uncompensated case and the compensated case is much more improved in all cases. These differences come from the response time of the controllers. Controller 1 has a much higher bandwidth than controller 2. However, an advantage that controller 2 has over controller 1 is that it has a much better robustness due to its higher phase and gain margins. In this sense, it can be seen that the

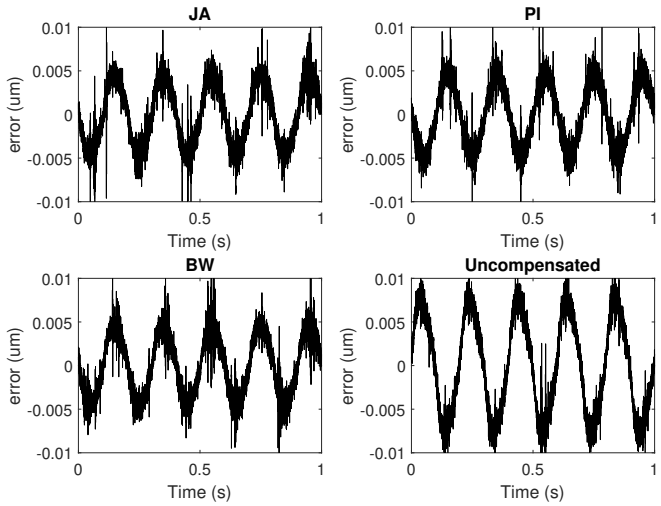

Figure 2.24: Controller 1 tracking error for a sine wave signal comparing the different hysteresis models

feedback-feedforward controller can enable more robust controllers.

An investigation on the noise spectrum in controller 1 is given in in Fig. 2.26 and for controller 2 in Fig. 2.27. It can be seen that the two differential equations based controllers do not significantly affect the noise spectrum as compared to the uncompensated case however, the PI model has some additional peaks of noise that are not present in the other models. This is most likely due to the disjoint nature of the PI model where each threshold value in the input produces an unsmooth transition to a new line segment. the differential equation based models do not have this problem because they produce smooth curves. In controller 2, much less noise is present at high frequency in all cases. These experiments suggest that for sine wave signals, hysteresis compensated proportional-integral controllers are very effective at improving performances for slower controllers.

Figs. 2.28 and 2.29 show the tracking errors for a triangle wave signal shown in Fig. 2.10. These figures show a different error profile compared to the sine wave signal but compensated about as well compared to this first case. Error wise, all compensators perform similarly and produce about half of the largest error present in the uncompensated case when using the

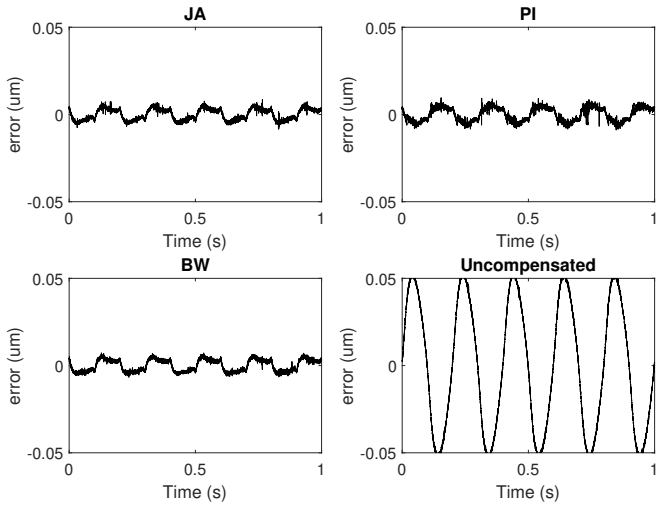

Figure 2.25: Controller 2 tracking error for a sine wave signal comparing the different hysteresis models

controller 1 gains. For controller 2, A much reduced error compared to the uncompensated case is found.

Figs. 2.30 and 2.31 show the frequency spectrum of the errors of both controllers for the triangle reference signal. Both controllers have a significant amount of frequencies in the lower end of the spectrum which is partly due to harmonics present in the wave pattern. The difference between the two controllers is not as large as that found in the sine wave reference, but it can still be observed that more high frequencies are present in controller 1 compared to controller 2, and that the PI model tends to have more higher frequencies in its errors.

In this chapter, the PI, JA, and BW models were introduced. Additionally, their performance as compensators for a PEA were analysed in open and closed loop applications. The models showed reasonable accuracy with the PI model being more accurate in triangle wave applications while the JA and BW models showed similar accuracy to each other and were both better than the PI model for sine wave applications. The closed loop performance showed comparable results for all models and improved especially the performance for slower, more robust controllers.

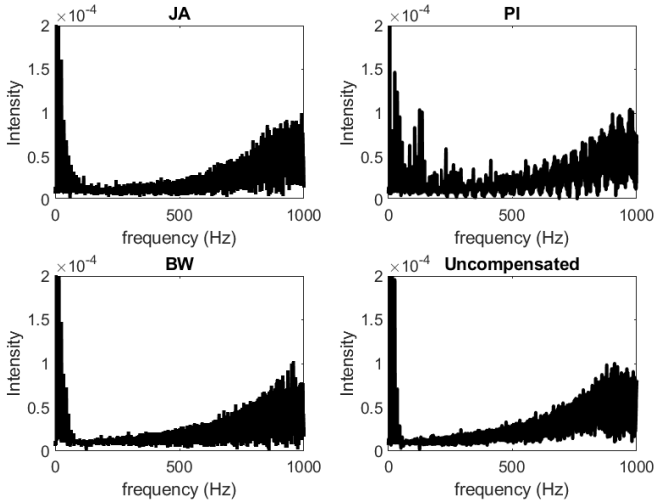

Figure 2.26: Frequency distribution of sine wave errors in controller 1 comparing the different hysteresis models

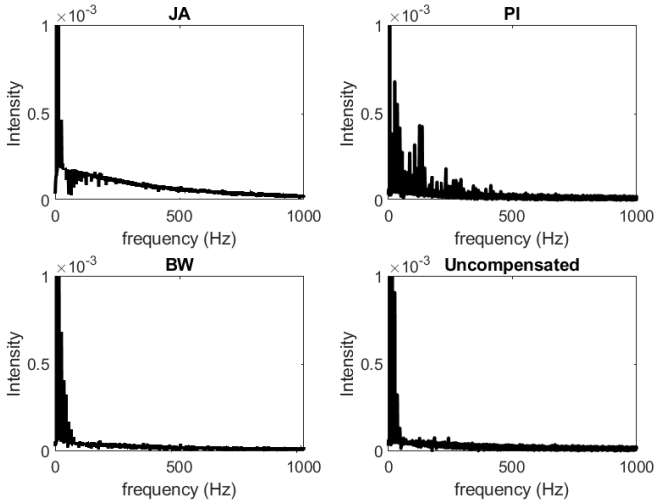

Figure 2.27: Frequency distribution of sine wave errors in controller 2 comparing the different hysteresis models

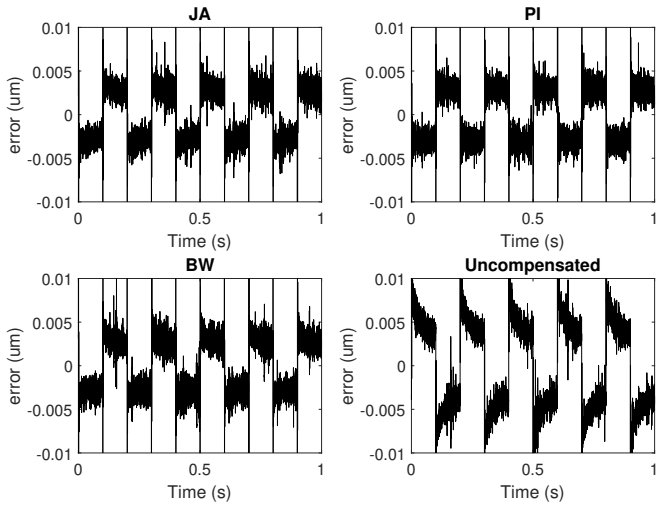

Figure 2.28: Frequency distribution of sine wave errors in controller 1 comparing the different hysteresis models

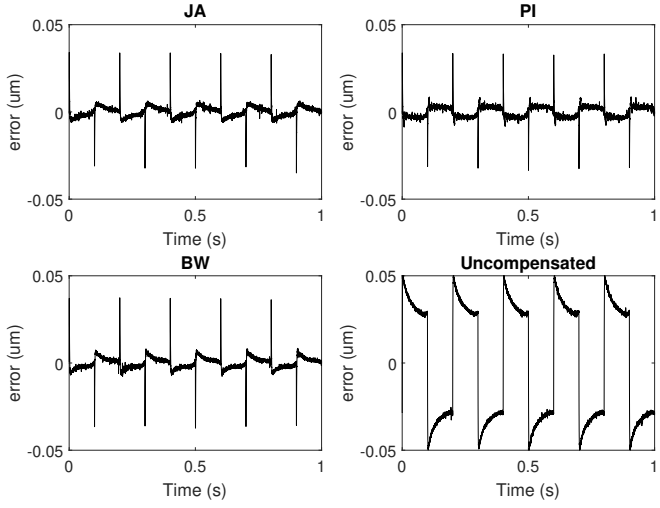

Figure 2.29: Frequency distribution of sine wave errors in controller 2 comparing the different hysteresis models

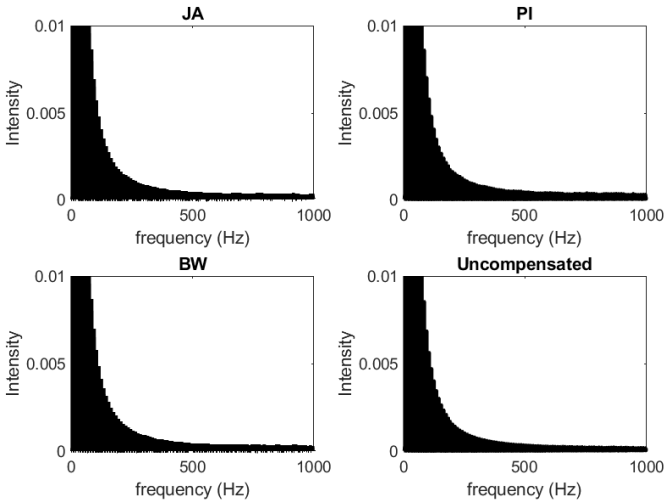

Figure 2.30: Frequency distribution of sine wave errors in controller 1 comparing the different hysteresis models

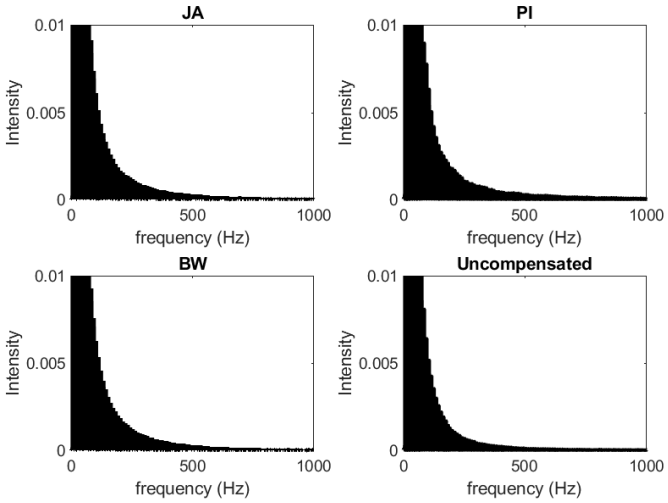

Figure 2.31: Frequency distribution of sine wave errors in controller 2 comparing the different hysteresis models

Chapter 3

Polarization Sensing in PEAs

The source of the piezoelectric effect in ferroelectric materials is the polarization changes in response to mechanical or electrical excitations. It has been observed that charge driven control of PEAs cancels a significant amount of the hysteresis in the system. This fact is largely due to its connection with the polarization of the system. One of the difficulties related to charge driven control of PEAs comes from the complications related to the PEA amplifier. It is relatively straightforward to design a voltage driven amplifier to drive a capacitive load such as a PEA. However, current amplifiers are normally more complicated to implement than typical voltage solutions [54].

The objectives in this chapter is to measure the polarization state of a PEA over the course of its movement and to describe the hysteresis between voltage and polarisation with the JA model. A hysteresis compensator that functions in the polarisation domain is then tested.

3.1 Experimental System

The experimental system for this set of experiments relies on measuring a current over the course of the PEA's driving range. This is not natively possible using the E-625 which only provides an output of the PEA position and knowledge of the PEA input voltage. The PEA system used in these experiments is the P-843.30 preloaded stack actuator. This device is equipped with a strain gauge sensor that is used for displacement measurements of the PEA system. However, the E-625 amplifier is not equipped to read this sensor natively. For these experiments, the Quanser Q8 data acquisition card is used in conjunction with MATLAB simulink. The Quanser Q8 can be used to both power the strain gauge sensor and read the voltage difference on the Wheatstone bridge. The operating principle of the Wheatstone bridge can be explained by examining the schematic of the circuit. Fig. 3.1 shows a schematic of the Wheatstone bridge circuit used in the P-843.30. The system is composed of 4 Resistors and 4 equipotential points. Resistors R_1, R_3 are constant resistors and resistors R_2, R_4 are resistances produced by strain gauge strips. These strain gauge strips are placed on the PEA material and stretch with the actuator. The strain gauge itself is a substrate upon which a conductive thin film pattern is placed. This conductive region will stretch with the substrate causing the electrical path to narrow or widen if the material is contracted. These effects serve to change the resistance of these reistors in respone to the strain of the material. This strain dependent resistance if measured can be used as a strain detector on the device.

Strain sensing on a Wheatstone bridge is done by applying some voltage u_{AC} to points A and C and measuring voltage u_{BD} on points B and D. The current from point A has two paths it can follow to reach point C. The first path crosses R_2 and R_3 and the second path crosses R_1 and R_4. If the resistances are balanced within the bridge, the output $u_{BD} = 0$ because the same amount of current is flowing through each path. Using the voltage divider

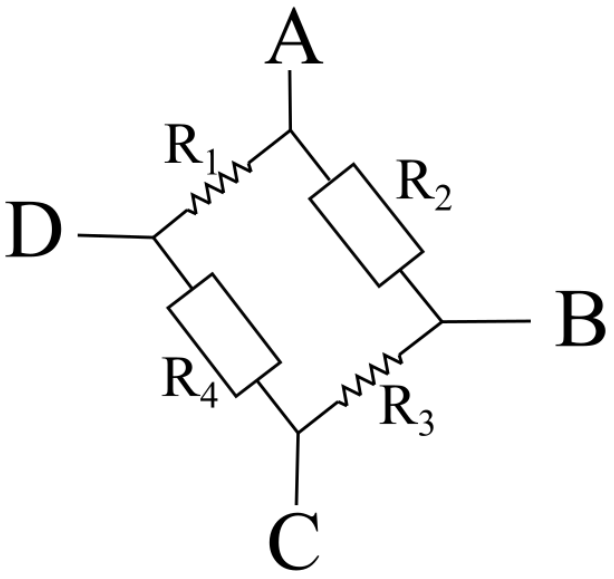

Figure 3.1: Strain gauge sensor bridge circuit

equation, u_{BD} can be calculated as follows.

$$u_{BD} = u_{AC}(\frac{R_3}{R_2 + R_3} - \frac{R_1}{R_1 + R_4}) \tag{3.1}$$

Assuming $R_r = R_1 = R_3$ and $R_s = R_2 = R_4$ where R_r is a reference value of resistance and R_s is the stain gauge resistance, Eq. (3.2) can be used to measure the resistance of the strain gauge.

$$R_s = R_r(2\frac{u_{AC}}{u_{BD}} - 1) \tag{3.2}$$

The current moving through the PEA is measured by adding a resistance to the low side of the PEA before the voltage is grounded. This shunt resistor is a low value such that it does not affect the voltage on the PEA by very much and allows for the determination of the current across the resistance using Ohm's law. The measurement of the current moving through the resistor is done using a current sense amplifier AD8418. A low-pass filter is added to the current sense amplifier to filter out noise found in the current signal. Fig. 3.2 shows the shunt based current sensor used on the PEA device. The AD8418 chip provides an

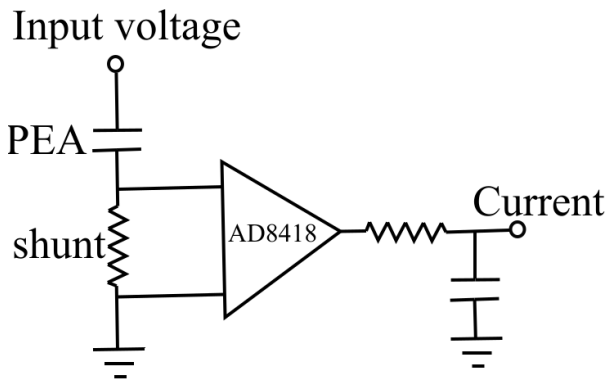

Figure 3.2: Shunt based current sensor used to measure current flowing through the PEA

amplification of 20x for the current sensed across the shunt.

3.2 Impedance-Based Polarization Sensing

The polarization state of the PEA is difficult to measure directly. However, a change in polarization in the PEA will also change it apparent capacitance. A stack actuator such as the P-843.30 is made up of several wafers of piezoelectric material stacked on top of each other. Fig. 3.3 shows an equivalent circuit of the stack actuator. On the left, the stack actuator has a series of electrodes sandwiching a volume of piezoelectric material between them. All electrodes are powered in parallel. On the right, an equivalent circuit of capacitors in parallel are shown.

The piezocermamic within the PEA is a dielectric with high resistance. Each plate of the capacitor elements within the PEA is assumed to be parallel with the other plates forming a collection of parallel plate capacitors plugged in parallel. The capacitance of a parallel plate capacitor can be written as follows.

$$C = \frac{\varepsilon A}{d} \tag{3.3}$$

Where C is the capacitance, ε is the electric permittivity of the enclosed material, A is

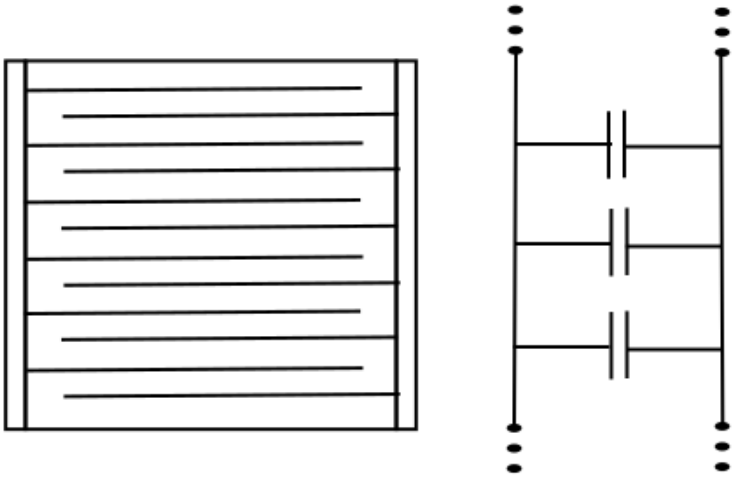

Figure 3.3: Piezoelectric stack actuator equivalent capacitor circuit

the area of the plates, and d is the spacing between the plates. The capacitance is related to the permittivity which is itself related to the polarization of the embedded material. Consider the electric displacement field $\boldsymbol{D} = \varepsilon \boldsymbol{E}$ where $\boldsymbol{E}$ is the electric field vector. The field between parallel plates can be considered unidirectional and uniform therefor vector notation is unnecessary at first approximation. The following expression for the capacitance involving the polarization can be written by introducing the effective field.

$$C = \frac{(\varepsilon_0 + \alpha \frac{P}{E})A}{d} \tag{3.4}$$

Eq. (3.4) relates the capacitance of a single capacitor component in the stack actuator to the polarization of the material. If the polarization varies linearly with the electric field, then the capacitance remains constant over the input range. However, as was seen in section 2.1.2, the polarization in a ferroelectric material is not linear. It is then expected that the capacitance of the actuator should change as it is driven electrically. It has been observed in PZT thin films that the capacitance decreases for rising voltage levels above 0V [64, 65]. The reason for this drop is due to the tendency for the polarization to saturate. The saturation

Table 3.1: Dimensions of the P-843.30 capacitor elements

Length	5.0 mm	Width	4.8 mm
Thickness	0.055 mm	number of wafers	600
Travel range	45 um	Resonant frequency	10 kHz

makes the slope of the polarization decrease as the electric field increases and as seen in Eq. (3.4), the capacitance of the PEA depends on the ratio of the polarization over the electric field. The saturation shrinks this ratio and an apparent drop in capacitance is the result. The PEA is not a single capacitor but multiple capacitors in parallel as seen in Fig. 3.3. Table 3.1 shows some of the characteristics of the P-843.30 actuator. It is composed of 600 capacitive elements arranged in parallel with dimensions 5.0 mm $\times$ 4.8 mm $\times$ 0.055 mm.

It should be noted that measurements of polarisation based on Eq. (3.4) is only possible in a quasi-static case and that deviations away from the ideal parallel plate capacitor will also introduce errors in the calculation of the polarisation. However, if the frequency at which the polarisation is measured is fast compared to the frequency that the PEA is driven, then the quasi-static approximation is applicable. Ensuring that the capacitors are ideal capacitors is more difficult to verify but ultimately isn't too important for these measurements since the true value of the polarisation isn't necessarily being sought. Rather, the qualitative dynamics of the polarisation is what is most important in this section and a capacitor that is roughly a parallel plate capacitor will behave similarly to the ideal case with some extra nonlinearity that is not accounted for in this section but of smaller importance than the main contributing components.

Capacitors in parallel are additive. Assuming N identical capacitors make up the measured capacitance of the system, the following equation for polarization can be written.

$$P(t) = \frac{\left(\frac{C(t)d}{NA} - \varepsilon_0\right)}{\alpha} E(t) \tag{3.5}$$

In principle, thickness of the wafers will also change due to the piezoelectric effect when E is varied. The travel range of the P-843.30 is 45 um for all 600 wafers. The change in a single wafer can be found by dividing it by the total number of wafers. Hence, a single capacitor in the system will see its thickness increase by 75 nm over the maximum input range of the PEA which represents approximately 0.1% of the thickness of the PEA. Since this contributes to the capacitance by a small amount, this interaction is neglected and the separation of the capacitor plates are assumed to be constant. The electric field is related to the input voltage on the plates of the capacitor. The electric field between two plates can be obtained by using the equation $E = V/d$ where V is the voltage across the plates and is the input parameter in our system. A method is required to obtain the capacitance.

To obtain the capacitance, the impedance of the PEA is calculated knowing the voltage and current characteristics of the system. However, to calculate the impedance, a reference signal is needed to calculate the impedance at a particular frequency. The impedance of the system Z can be calculated as follows.[66]

$$Z = \frac{|V|}{|I|} e^{i(\phi_V - \phi_I)} \tag{3.6}$$

Where V is the voltage, I is the current, ϕ_V is the voltage phase and ϕ_I is the current phase. A capacitive impedance is defined by the following purely imaginary impedance.

$$Z_C = \frac{1}{i\omega C} \tag{3.7}$$

Where ω is the angular frequency. To obtain a capacitance measurement, the signal must be overlaid with a sensing frequency. Ideally this sensing frequency would have a high enough frequency that the PEA would not be capable of meaningfully responding to it which would be the case above its resonant frequency. However, due to the limited sampling rate of the

Quanser Q8, it is not possible to create frequencies that are sufficiently high. Instead, a 50 Hz ripple voltage is superimposed onto the signal with a small amplitude. This signal allows for the possibility of sensing the capacitance of the PEA while minimizing the displacement changes as much as possible. A ripple frequency that is higher than the driving frequency is required if capacitance is to be monitored over the course of the driving range. For example, if an impedance is calculated using the driving frequency, it corresponds to the average impedance value over the period.

Fig. 3.4 shows the input overlaid with a ripple signal used to measure the impedance of the device. Fig. 3.5 shows the measured current associated to this input. It can be seen that the ripple current is very prominent in this measurement due to the fact that it is of much higher frequency than the driving voltage and capacitive loads have a smaller impedance towards faster frequencies. The effective sampling rate of the impedance measurement becomes 0.02 s due to requiring this much time to complete one cycle which is the minimum requirement to extract its information using a FFT alorithm. From the fourier coefficients that are obtained, and assuming that the imaginary impedance is purely capacitive, the following equation can be used to obtain the capacitance

$$C = -\frac{1}{\omega_r}\frac{A_{I_r}^2 + B_{I_r}^2}{A_{I_r}B_{V_r} - A_{V_r}B_{I_r}} \tag{3.8}$$

Where ω_r is the angular frequency of the ripple signal, $A_{I_r} = Re(I_r)$ is the real value of the ripple current, $B_{I_r} = Im(I_r)$ is the imaginary value of the ripple current, $A_{V_r} = Re(V_r)$ is the real value of the ripple voltage, and $B_{V_r} = Im(V_r)$ is the imaginary value of the ripple voltage. From the capacitance, Eq. (3.5) can be used to find the polarization. Fig. 3.6 shows the results of this process. At the peaks of the polarization curve, it can be seen that a polarization drop seems to occur when the voltage changes directions. This drop is likely due to some coupling between the two signals. As can be seen in the current plot in Fig. 3.5,

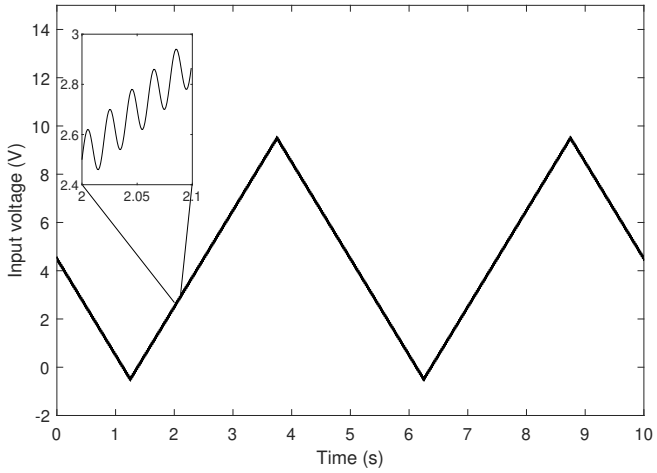

Figure 3.4: input voltage onto the PEA system showing a low frequency, high amplitude driving signal overlaid with a high frequency, low amplitude ripple signal

the driving signal generates some current jumps depending on if the voltage is increasing or decreasing. These jumps have frequency components that are common to the ripple signal and impede the measurements. Better results may be acquired with higher frequencies that are difficult to achieve with the used hardware in these experiments, but may be achievable with different hardware in future experiments.

3.3 Polarization Hysteresis Compensation

The polarization state of the PEA is closely connected to the JA model estiblished in Section 2.1.2. It is then required to find JA model parameters that suitable for the PEA system. The P-843.30 is an actuator based on the PIC 255 PZT material. Some general approximations on JA parameters can be found using material properties as outlined in [67]. The saturation polarization is the most straightforward to obtain from data by examining the value at which the material saturates in polarization. At room temperature, A saturation polarization of approximately 0.35 C/m^2 is measured and a coercive field value of approximately 1.5 kV/mm

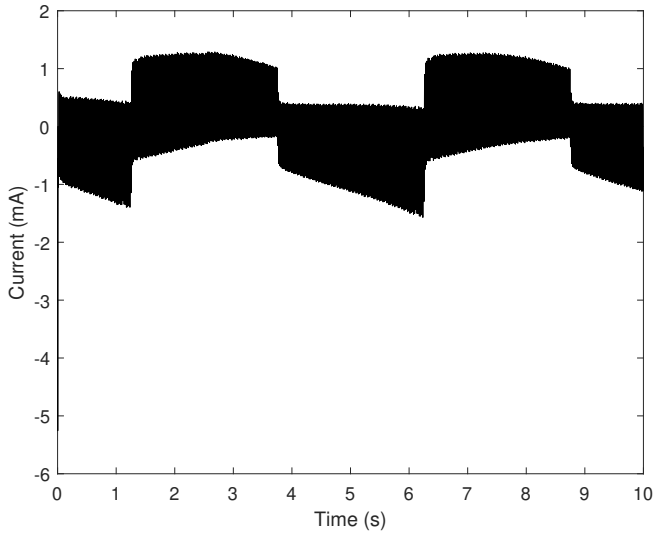

Figure 3.5: Measured current flowing through the PEA showing a large current generated by the ripple signal

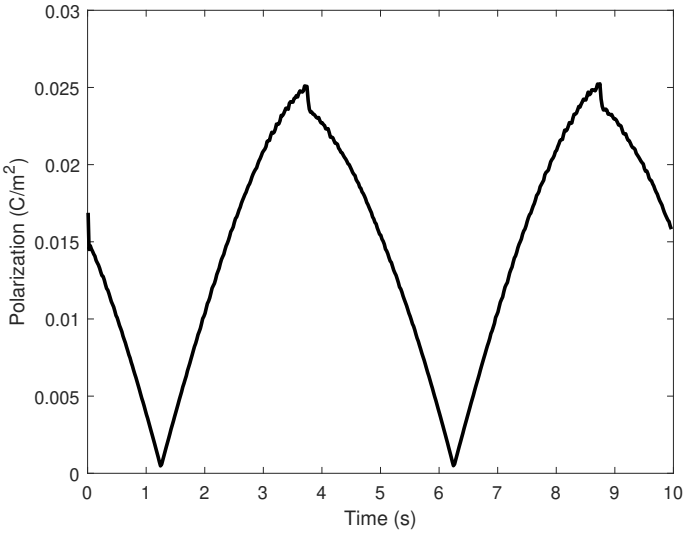

Figure 3.6: Polarization measurements based on voltage and current measurements

[68]. Fig. 3.7 shows a diagram of the ferroelectric hysteresis with several susceptibility values $\chi(E) = \frac{dP}{dE}$ at key locations. A simple first approximation for the pinning factor is to give it the value of the coercive field $k = E_c = 1.5 \times 10^6$ Parameter c is estimated based on the tip susceptibilities when the polarization changes direction $c = \frac{\chi^-}{\chi^+}$. This is due to the fact that c is a ratio between reversible and irreversible processes. When the polarization hysteresis is at a high value in an increasing direction, most of the domains have been unpinned and the reversible processes dominate. Wheras when the direction is initially reversed, the irreversible process dominates due to requiring depinning before the output reacts to the change of direction. Parameter a can be approximated using the susceptibility at the coercive field $a = \frac{P_s}{3\chi_c}$. Parameter α can be estimated from parameters a and P_s as follows $\alpha = \frac{3a\chi_c - P_s}{P_s\chi_c}$. Utilizing these approximations and minimizing by least squares, an appropriate polarization model that is crudely based on the ferroelectric properties found in the literature can be found.

Inverting the JA model allows for the compensation of the polarization hysteresis when it is voltage driven. Fig. 3.8 shows the result of the compensated polarization curves using the JA inverse model. It can be seen that the polarization tracks the triangle wave pattern well though there s some disagreement notably at the peaks. Fig. 3.9 shows the percent error throughout the trajectory. It can be seen that the modeling error is generally below 5% through at the peaks, it can jump to over 10%. To examine the influence of the Polarization state of the PEA on its displacement, the displacement measured by the strain gauge circuit is examined and plotted with the modeled polarization in Fig. 3.10. It can be seen that the hysteresis between the displacement and polarization is reduced compared to the hysteresis between the voltage and the displacement. This is what is expected since polarization is closely related to the charge on a capacitor. However, when compared to charge driven data found in the literature, the measured hysteresis between polarization and displacement is larger than that found between charge and displacement [69]. This may be due to experimental

errors present in the experimental method and should be investigated more closely to obtain a better understanding of the influence of polarization on the displacement hysteresis in PEAs.

In this chapter, a polarisation sensing scheme is presented to obtain hysteresis curves between the polarisation and the voltage by measuring the current produced by a high frequency, low amplitude ripple signal that is overlaid over the driving signal of the PEA. The polarisation was then fitted to a JA model and a compensator was designed to linearize the polarisation of the PEA.

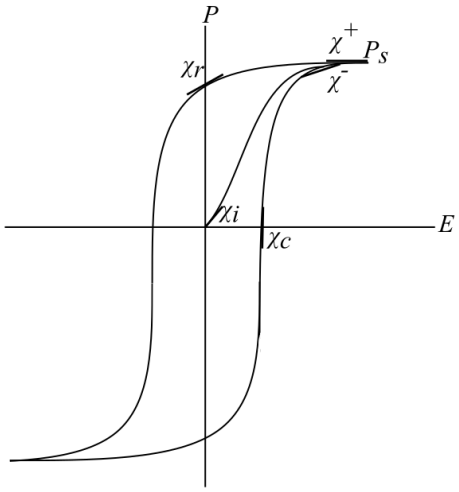

Figure 3.7: Diagram of ferroelectric hysteresis showcasing several key susceptibility locations

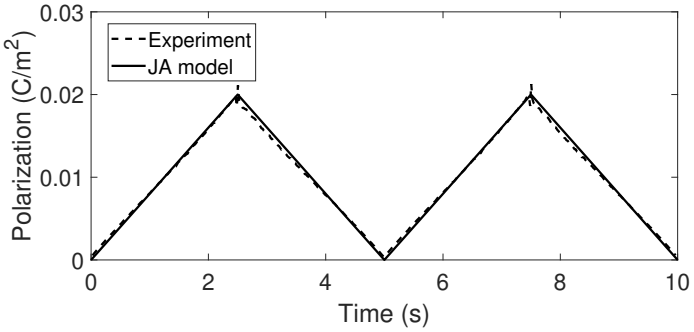

Figure 3.8: Polarization compensated for hysteresis using the JA model

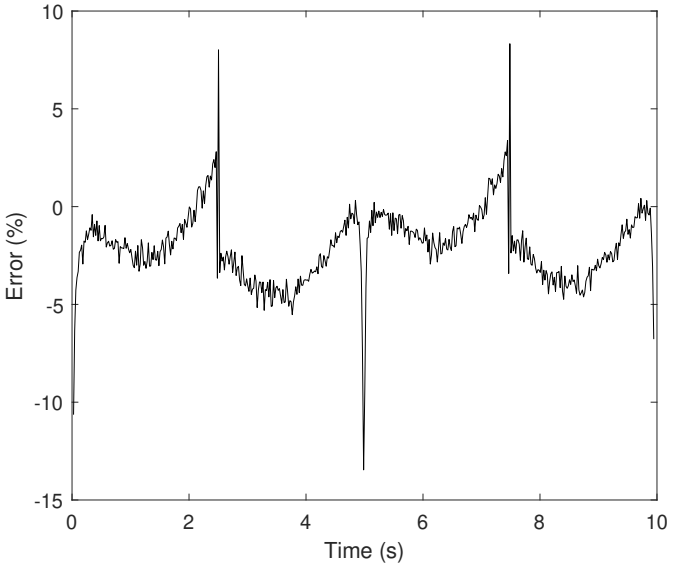

Figure 3.9: Modeling error in polarization using the JA model

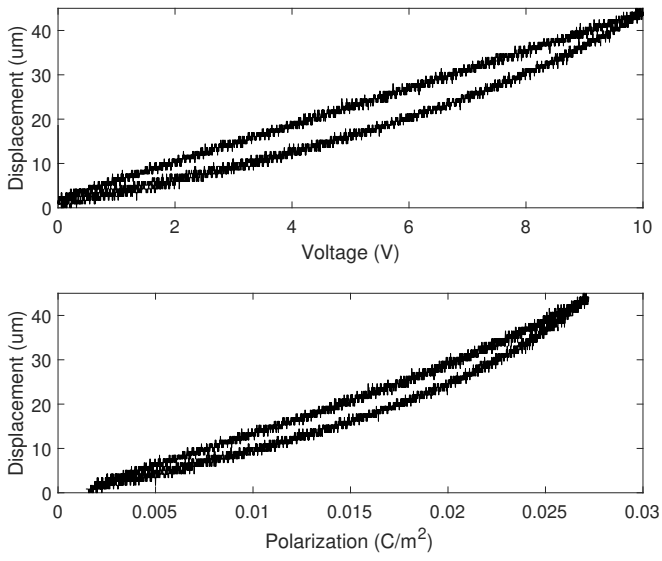

Figure 3.10: Displacement vs polarization hysteresis compared to displacement vs. voltage

Chapter 4

Parameter Estimation of Hysteresis

Generally when modeling some aspects of PEAs, parameter estimation algorithms are required to obtain the best possible models for data extracted from the PEAs. For many hysteresis models, the estimation can be difficult to perform in a timely manor which can be detrimental to some control methods that may seek to tune model parameters online [70]. The popularity of the PI model of hysteresis is partly due to its ease of parameter identification but as the model becomes more complicated with more and more modified operators that are harder to treat geometrically, parameter identification algorithms are often required to find some elements of these models [71].

Taguchi's method is a global optimization method based on the use of orthogonal arrays [72]. The idea behind the Taguchi method is to attempt to preserve the strengths of an exhaustive search for parameters, but while improving the efficiency of the search. An exhaustive search of parameters is the least efficient search method but is guaranteed to find the optimal configuration of parameters in the discrete finite case. Taguchi's method seeks to compare multiple configurations while minimizing overlapping configurations through the use of orthogonal arrays. The Taguchi method was successfully used in identifying JA model parameters for ferromagnetic properties of non-oriented steel showing better performance

than genetic algorithms, differential evolution, and particle swarm optimization methods [73]. However, Taguchi's method does not have a suitable 5 parameter orthogonal array for the JA method and thus a larger orthogonal array must be used which can slow down the process compared to a 4 parameter model like the BW model.

The Nelder-Mead algorithm is a method that can be used to solved an unconstrained optimization problem. The Nelder-Mead method is based on a simplex structure in the parameter space of the multi-valued function being minimized. The original algorithm was first proposed by Nelder and Mead in 1965 as a method to solve function minimization problems [74]. The Nelder-Mead method is widely used for numerous optimization problems but does not natively handle constraints which may be present in the problems.

The Taguchi method and the Nelder-Mead algorithm are both deterministic optimization algorithms that will return the same result for the same inputs. This puts a burden on appropriate initial conditions for proper convergence. For nonlinear problems such as hysteresis, stochastic methods are often reported with good results. The Genetic algorithm is inspired by evolutionary processes in biological systems. In this model a population with different parameter values are generated and assessed based on their fitness results. The results that fit the problem the best are kept and combined while the weaker results are discarded. A new population based on the stronger members is generated. A key stochastic element in the genetic algorithm is a mutation parameter which have a chance to skew certain parameter values away from the parent population and allows the global space to be more properly explored. Another stochastic parameter estimation algorithm is the particle swarm optimization algorithm that is described in the following section. One of the appealing properties of many stochastic methods is that their formulation is well suited to modification [75–77].

In this chapter, two new parameter estimation techniques are developed. The first one involves the JA model in which a data set of normalised JA models is created using the Monte

Carlo method to analyse which parameters of the JA model are most responsible for changes in remnant strain and hysteresis area. A modified particle swarm optimization algorithm is then proposed based on the Monte Carlo data analysed to speed up the parameter estimation time. Secondly, a parameter rescaling procedure is developed for the PI model which easily scales the area of a PI model based on modifying one parameter and rescaling all parameters such that the hysteresis curve returns to its original length. This rescaling procedure is then applied to the application of frequency dependent broadening of hysteresis curves.

4.1 Particle Swarm Optimization

The particle swarm optimization (PSO) method is a stochastic global optimization method inspired by the behavior of swarms of animals in the wild searching for food. It has been observed in the wild that flocks of birds can cooperate to share information about food discoveries to the entire flock to benefit the population. Inspired by this process, the PSO method seeks to send objects called particles throughout the parameter space to find optimal solutions to the problem being investigated. A particle is a point in the parameter space of the optimization problem which yields some value for a fitness function associated to this point. The general principles of the PSO method is to distribute a finite number N of particles throughout the parameter space and to assess their fitness for the optimization problem. This is the first step of the PSO algorithm and the main decision that must be made is in the distribution of parameters across this space. Initial conditions can have a large effect on the overall speed of convergence of this algorithm because some configurations may have all particles far from the optimal solution. Other configurations may have some particles close to the optimal solution.

Once an initial distribution of particles is set for the PSO method, the particles broadcast their fitness results and the particle with the best performance influences the behavior of

other particles in the swarm. A movement algorithm must be defined for the particles in the swarm such that each iteration, the particles will move from their position in the parameter space and assess another candidate solution, with the knowledge of the current best known solution in the space. Consider a vector $\boldsymbol{X} = [x_1 x_2 ... x_n]^T$ such that a function $f(\boldsymbol{X})$ is defined. $\boldsymbol{X}$ denotes a position in the parameter space and $f(X)$ is the fitness function. The parameter space is of order n and denotes the number of coefficients that are sought to be optimized.

A particle $P = [\boldsymbol{X}, \boldsymbol{V}]^T$ is a quantity that is characterized by its position and velocity V. The velocity term is the important evolutionary term in the algorithm and provides a means for the positions of the particle to change every iteration and continue to search for better solutions. Each particle retains information about its own personal best position in the parameter space, p_B, as well as the group's best position g_B. The velocity term is dictated by these two quantities and can be described as follows.[78]

$$\boldsymbol{V}_i(t_{k+1}) = w\boldsymbol{V}_i(t_k) + c_1 r_1(\boldsymbol{p}_B(t_k) - \boldsymbol{X}(t_k)) + c_2 r_2(\boldsymbol{g}_B(t_k) - \boldsymbol{X}(t_k)) \tag{4.1}$$

Where w is referred to the inertia of the particles, c_1 and c_2 are referred to as cognition parameters, and $r_1, r_2 \in [0, 1]$ are random variables. The random variables are important to prevent premature convergence into a local minima and creates a means for particles to explore in unknown directions and hence increases the chance of finding a global minima. The cognition parameters tune the amount of bias the particles place on swarm information. A higher c_1 creates more personal bias whereas a higher c_2 creates more global bias. The inertia adds a component of influence of the previous velocity term. A higher inertia will mean that it is more difficult to influence the direction of the particle. The second step in the PSO algorithm is to update the position in a successive iteration based on the updated

velocity rule shown in Eq. (4.1).

$$\boldsymbol{X}_i(t_{k+1}) = \boldsymbol{X}_i(t_k) + \boldsymbol{V}_i(t_{k+1})\Delta t \tag{4.2}$$

Eq. (4.2) updates each particle's positions to assess their values. The values of the coefficients w, c_1, c_2, the initial positions of particles, and the number of particles are all factors that can be used to tune the PSO performance. The biggest disadvantage of the PSO algorithm is that if these parameters are not chosen correctly, premature convergences can occur and unsatisfactory optimization can result. However, in some cases, the convergence can be too weak and convergence time is then very long. In particular, the inertial term in the PSO has a large effect on the convergence of the PSO algorithm and several structures have focused on its modification to improve convergence of the algorithm on a variety of problems. In [79], it was found that varying the inertia factor randomly performed well and most efficiently of several strategies tested. Utilizing this process, the PSO algorithm intertia can be selected randomly between 0.5 to 1.

The PSO method does not innately contain parameter boundary handling and thus for problems with boundary constraints, these properties must be added to the PSO algorithm. Different approaches are used for this purpose such as changing the personal and global best updates past the boundaries, repositioning the particles, and preventing the infeasible positions before they occur [80]. One approach is to define a bounce function when a particle reaches a wall. This can be done by the reflect method. This method is illustrated in Fig. 4.1 and represents the case similar to a billiard ball bouncing off a wall. An expression for the new position of the parameter $x'(t_{k+1}$ can be calculated as follows

$$x'(t_{k+1}) = x_b \pm |x(t_{k+1}) - x_b| \tag{4.3}$$

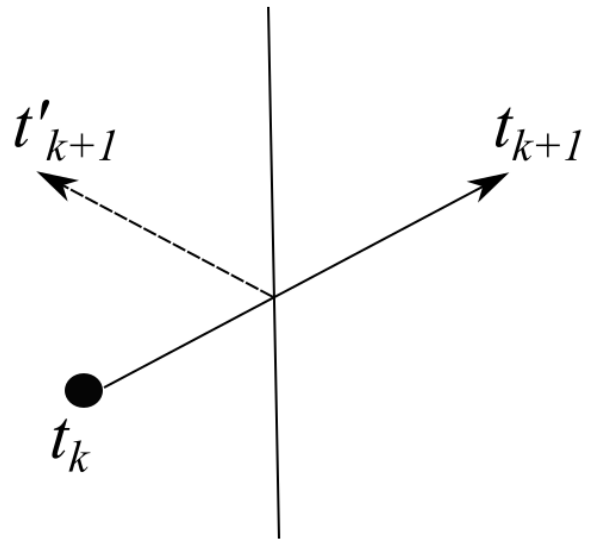

Figure 4.1: Particle reflecting at parameter boundary

Where x_b is either the positive or negative bound in question and the sign of Eq. (4.3) is taken positive if x_b is the lower bound or negative if x_b is the upper bound.

4.2 Monte Carlo Studies on Hysteresis

Monte Carlo methods are a technique that is characterized by the repeated use of randomized variables to obtain a sample of data. These methods are used in a broad range of problems in many different disciplines. In physics, these methods are utilized to simulate different processes such as the quantum monte carlo methods that seek to find solutions to certain complex multivariable problems. Otherwise, many statistical physics problems that require a large number of variables can often be solved using monte carlo methods by randomly assigning variables and examining the effects of the models under these conditions. The overall strength of Monte Carlo methods rely on a statistical ensemble that is useful to solve a problem. In this section, Monte Carlo methods are utilized to create a large number of of potential hysteresis solutions and appealing aspects of the curves are extracted from the data

to attempt to find probabilistic patterns in parameter identification.

The goal is to set up Monte Carlo experiments that can be used to better understand the effect of parameter selection of the JA model established in section 2.1.2. In this model, five parameters must be estimated to create a hysteresis curve. However, not all parameters yield appropriate hysteresis curves for the PEA system. For example, some solutions will generate curves with a negative slope when the rate of change of the input is positive. This situation is nonphysical. Also, the JA model being a model for ferroelectric hysteresis means that inherent in the equation is a memory component that can retain some non-zero value of output when the input returns to 0. This property is often called remnance but the JA model can generate solutions where the domain wall pinning is so high that each period, the model output climbs significantly for multiple periods. In fact, in PEAs, we observe that after the first period, the output will retain a non-zero displacement but does deviate considerably from this position value when the input returns to zero for successive iterations unless the PEA is allowed to rest for some period of time. In that case, solutions to the JA model that significantly deviate from the value $y(T)$ where T is the period of a periodic input function are considered nonphysical and rejected.

A useful measure of comparison of hysteresis curves generated by the JA model is also required in order to make statistical comparisons with the Monte Carlo method. After rejecting nonphysical solutions to the JA model, hysteresis curves of different lengths, areas, and shapes are produced with valid parameter configurations. Unmodified, these curves are difficult to compare because of their varying properties. A normalized JA model is found to adjust the length of the hysteresis curves to a common length. Doing this, hysteresis curves will only vary in area and in shape. This facilitates the use of the area as a measure for hysteresis curves because with the length normalized, comparing curves of similar area will mainly differ in shape.

To normalize the JA model, consider the classic JA model established in Eq. (2.33).

This differential equation produces hysteresis curves of length $L_m = y_m^{max} - y_m^{min}$ where y_m^{max} is the maximum output coordinate of the modeled hysteresis loop and y_m^{min} is the minimum cooredinate of the modeled hysteresis loop. These coordinates correspond to th closed hysteresis loop and thus the loading curves generated by the model should not take these values. The normalized JA model can be described as follows.

$$\frac{dP}{dt} = \frac{L_p}{L_m}\frac{dE}{dt}F(E,P) \tag{4.4}$$

Eq. (4.4) obviously normalizes the length to a chosen length L_p but such a description is not useful unless a similar scaling is also available for the compensator. Thankfully, due to the linearity of the differential operator, the following normalized inverse model can be derived as follows.

$$\frac{dP'}{dt} = \frac{\frac{dE}{dt}}{F(\frac{L_m}{L_p}P', E)} \tag{4.5}$$

The normalized JA model is extremely useful for parameter identification because many parameter candidates may be immediately rejected as JA model candidates of a system due to their lengths being very different. However, the normalize model has a scaling property that broadens the number of potential solutions for a given system.

With a scalable model of JA hysteresis, a Monte Carlo experiment can be conducted that generates N solutions to the normalized JA model. Parameters $\boldsymbol{p} = [P_s, c, k, a, \alpha]$ are randomized for each iteration until N suitable models are found. The bounds for the parameters are shown in Table 4.1. 2,000,000 hysteresis samples are generated to examine statistical trends in the parameter space of the normalized JA model. The input function for the JA model is the unipolar sine wave used in Eq. (2.40). From this input, it can be seen that the input starts at a minimum and reaches a maximum at a period of $T/2$.

A solution filter must be applied to the Monte Carlo simulation to remove nonphysical

Table 4.1: Monte Carlo simulation parameter bounds

Parameter	Lower bound	Upper bound
P_s	1	100
a	1	100
α	0.005	0.5
k	0.01	10
c	0.001	0.999

solutions from the set of data. As mentioned earlier, solutions in which the hysteresis curve goes in the opposite direction of the input must be removed. The following condition is applied to a generated hysteresis curve.

$$\text{sign}(H(u(T/2)) = \text{sign}(u(T/2)) \tag{4.6}$$

Eq. (4.6) sets a condition on the half-period of the hysteresis curve such that the maximum input value creates an output that is in the same direction as the input. The following condition ensures that the remnant displacement is positive.

$$H(u(0)) \leq H(u(T)) \tag{4.7}$$

Eq. (4.7) screens out certain situations in which the displacement varies in the same direction as the input but the value of the output when the input returns to its initial value is less than it was initially. This would represent a solution in which cycling the system produced domains with less overall energy than they started with which is not seen in practice. Finally, the following condition is necessary to screen out hysteresis curves that require more than a single period to adequately close.

$$\frac{H(u(T))}{H(u(2T))} > .98 \tag{4.8}$$

Eq. (4.8) requires the output of the hysteresis curve after one and two periods and requires the ratio of these two points to be sufficiently close together such that the second period climbs by no more than 2% of the previous period.

Each simulation solution from the Monte Carlo set has a measurable value of area. Let $u(t)$ be a periodic input with monotonic half-periods. Let p be the set of parameters that describes a hysteresis curve H_p. The area, $\gamma(H_p(u))$ of a hysteresis curve is defined by Eq. (4.9) over a single period T by the following integral which describes the area within the normalized area curve with the absolute value ensuring a positive value.

$$\gamma(H_p(u)) = \int_0^T \left| \frac{H_p(u(t))}{\sup H_p(u(t))} \right| dt \tag{4.9}$$

Fig. 4.2 shows the distribution of parameters in the Monte Carlo set. It be can seen that parameters are not typically uniform. This is due to the conditions imposed on the solutions of the normalized JA model. In particular, parameters a, c, and k are not uniform in distribution and therefore their selection within the studied bounds are more important to generate physical hysteresis curves. Parameter a has a greater chance to generate suitable hysteresis curves for larger values than for smaller values. This parameter is present in the denominator term of the tanh function in the anhysteretic term of the JA model as shown in Eq. (2.23. Smaller values of a serve to saturate the tanh function with smaller input values which may be why fewer acceptable solutions are found in this range. For parameter c, several solutions are available throughout its range. However, more solutions are available as c approaches 1. This parameter controls how how much of the domain wall deformation is reversible with 1 representing a completely reversible process and 0 representing a completely irreversible process. More reversible processes are more likely to create hysteresis curves that behave according to our constraints. The most notably skewed distribution is that of the parameter k whose values drop off very rapidly before $k = 2$. k is related to the amount of

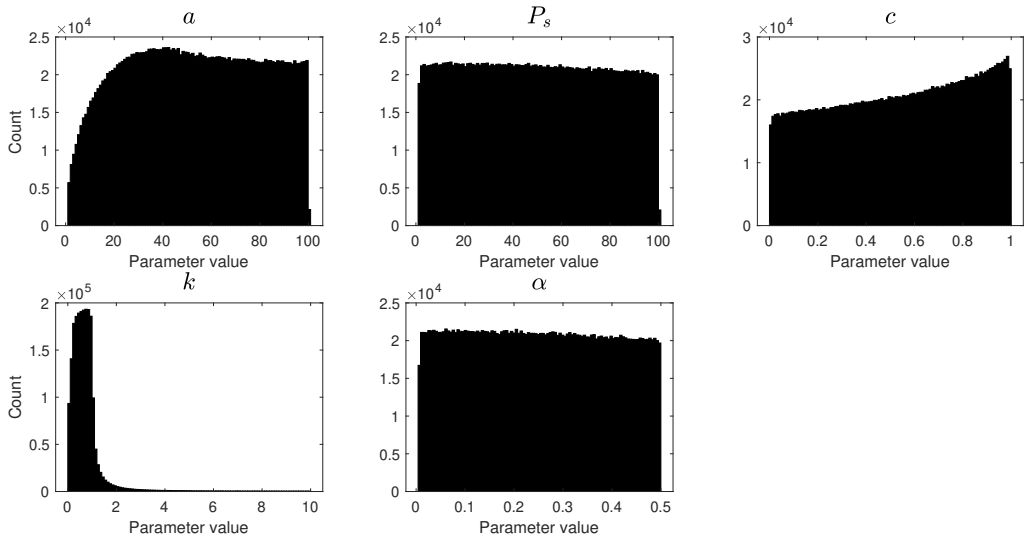

Figure 4.2: Histogram of the resulting JA parameters found through Monte Carlo simulations.

energy that is required to break pinning sites in the JA model. It is clear that two high of an energy requirement produces curves that do not behave as expected in practice.

Samples of the hysteresis models in the Monte Carlo are all of the same length due to the normalized property of the modified JA model. This allows for comparisons between hysteresis curves over a single axis rather than two. Area differences then represent hysteresis curves that are generally wider. Fig. 4.3 shows different hysteresis samples from the Monte Carlo simulations that are larger and smaller than the PEA curve. This example showcases a potential strategy for parameter estimation of hysteresis models when the model is scalable such as the normalized JA model. If information on normalized area is known, then solution candidates for the system's hysteresis can be found in areas of the parameter space that are dense in solutions that are close in area compared to the system. A distribution of the normalized areas found in the Monte Carlo data can be found in figure 4.4. It can be seen that the normalized JA model is more likely to generate smaller hysteresis areas. The PEA has a normalized area of 0.2022 placing it in an area of the parameter space that has many different solutions.

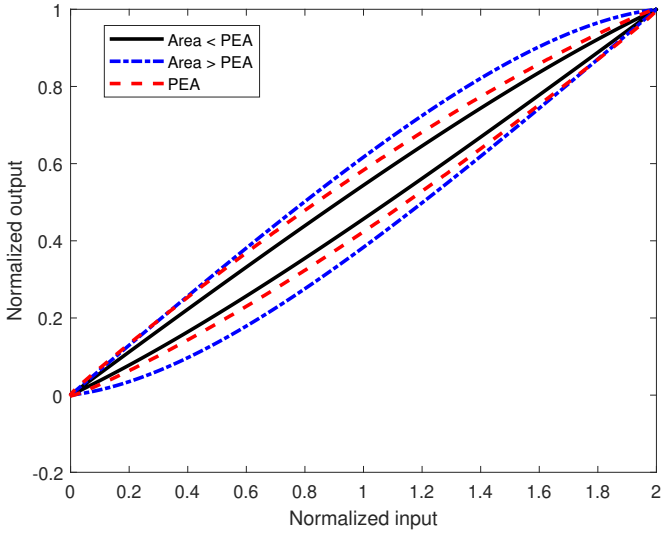

Figure 4.3: Comparison of JA hysteresis curves generated by Monte Carlo method with different normalized areas

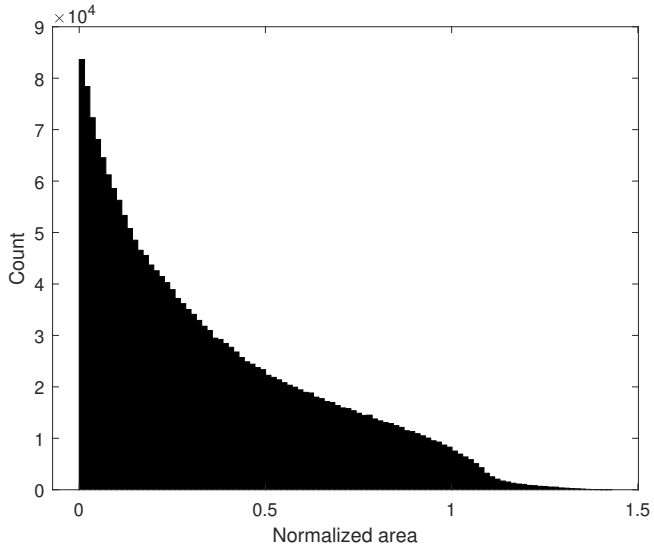

Figure 4.4: Histogram of the distribution of normalized found in the Monte Carlo data set

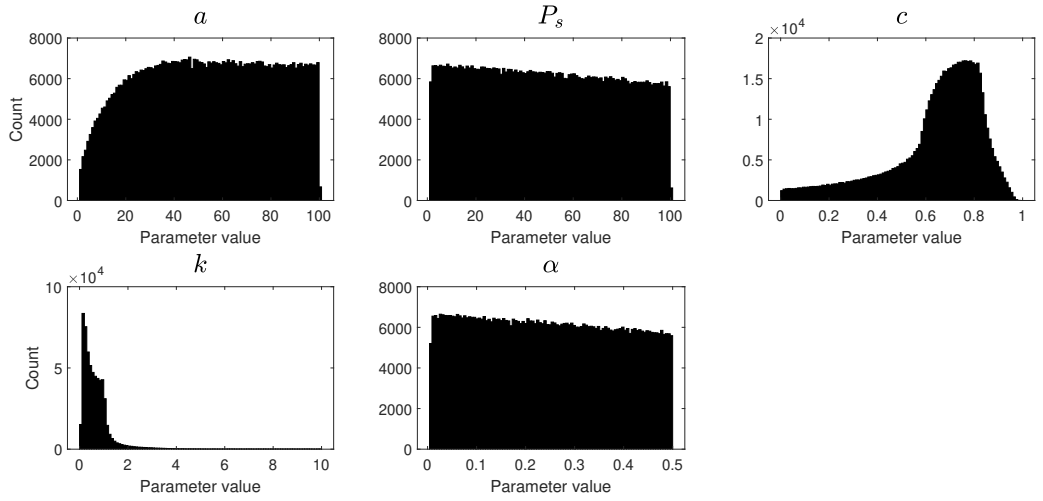

Figure 4.5: Histogram of Monte Carlo simulations with areas near the PEA area.

To examine the effects of area on the parameter space of the normalized JA model, Monte Carlo simulations that are near the PEA hysteresis are picked and a new distribution on this restrained set of data is examined. Hysteresis areas ranging from 0.15 to 0.25 are included in this new set. Fig. 4.5 shows the distribution over the parameter space in this new set of data. It can be seen that parameters a, P_s, and α are largely unaffected by this data filtering which suggests that they have a small influence on the area of the curve. This makes sense because these three parameters describe the anhysteretic curve which is hysteresis free. However, the parameters c and k are heavily modified compared to those found in Fig. 4.2. These parameters describe the motions of the domain walls and are the source of the hysteresis in the JA model. Thus, as expected, they are the most important parameters in the determination of the area of the normalized JA model. Fig. 4.6 shows a scatter plot between the parameters c and k. The results show that there is a cluster of points that is more dense in the lower right region compared to other locations.

In addition to the area, it is interesting to examine the effect of normalized JA model parameters on the remnant displacement that occurs after one period. This is what occurs

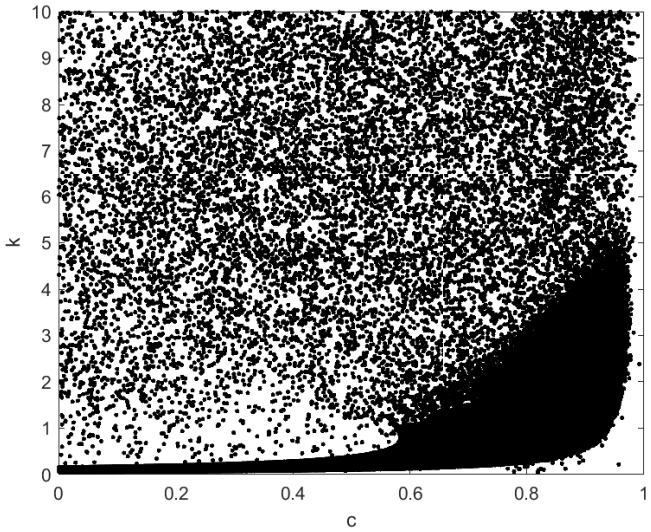

Figure 4.6: Scatter plot of parameters c and k in the Monte Carlo data set with similar area to the PEA.

when the PEA is first driven from a period of rest and the input returns to 0. This remnant displacement y_{rem} is calculated as follows.

$$y_{rem} = y(T) - y(0) \tag{4.10}$$

The remnant displacement can be extracted from the Monte Carlo data set and curves that possess a remnant displacement close to that found in the PEA is used to study what effect parameters have on this effect in the JA model. Fig. 4.7 shows the distributions of remnant displacements found in the Monte Carlo data. Shorter remnant points are more common than longer ones and they all appear under a value of 1. The reason for this is that the maximum value of normalized hysteresis curve is 1 thus a remnant displacement that is larger than this is not possible. Fig. 4.8 shows the parameter distribution found in the set of JA hysteresis curves in the restrained remnant displacement range. It is observed once again that c and k are the most heavily modified distributions in this restrained set but parameters P_s and α are slightly skewed compared to the distributions found in Fig. 4.2. A scatter plot

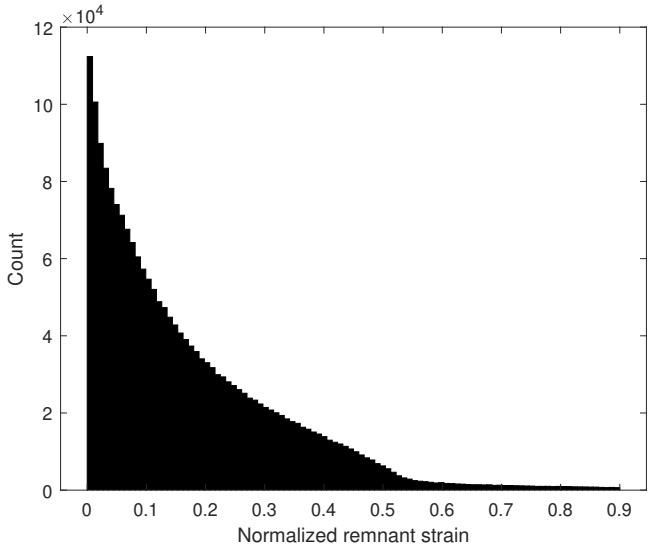

Figure 4.7: Histogram of the distribution of remnant strains found in the Monte Carlo data set

between parameters c and k is conducted in Fig. 4.9. Compared to the area distribution found in Fig. 4.6, solutions for remnant displacements near the PEA is much more densely positioned in parameter space.

4.3 Improved Particle Swarm Optimization of JA Parameters

The PSO algorithm has been used before to find JA parameters. In [81], a PSO algorithm was adapted to the JA model my fitting a multiobjective function. It was found that comparing errors in the hysteresis area on as well as the normal least squares error could improve the convergence of the algorithm. In [82], An iteration dependent inertia was used to prevent premature converence. Inspired by these two approaches, two novel PSO algorithms for the JA model are developed. The first is the normalized particle swarm optimization algorithm (NPSO) in which the normalized JA model described in the previous section is used to

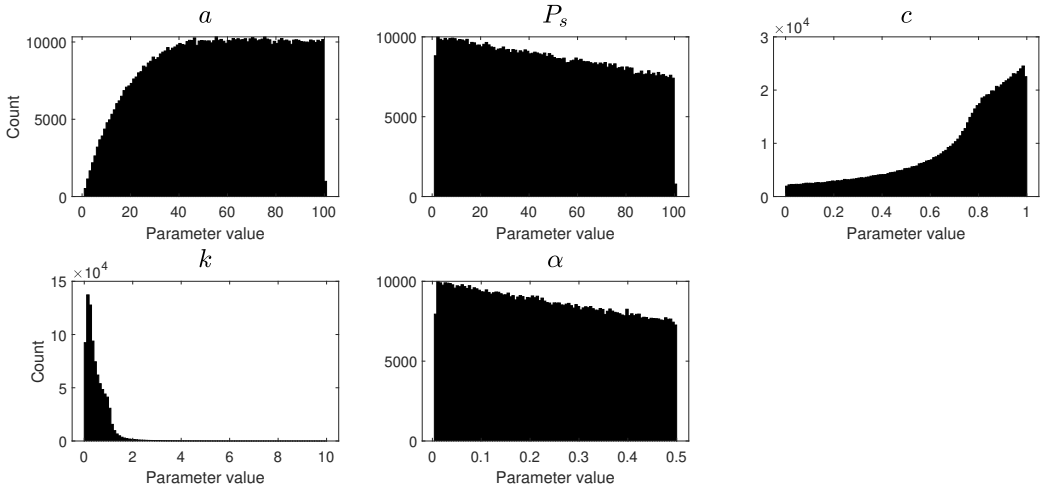

Figure 4.8: Histogram of Monte Carlo simulations with remnant displacements near the PEA remnant displacement.

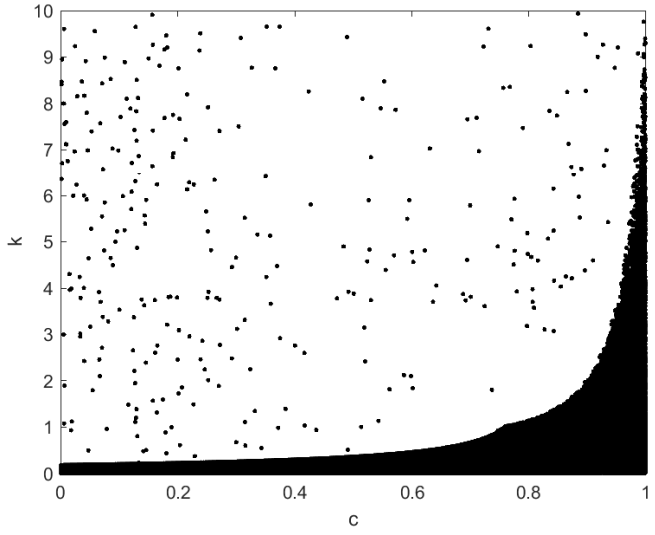

Figure 4.9: Scatter plot of parameters c and k in the Monte Carlo dataset with similar remnant displacements as the PEA

improve the rate of convergence of the JA model. A normalized, modified PSO algorithm is developed by adding an iteration-dependent term into the normalized PSO algorithm that is based on the data generated by the Monte Carlo experiments of the previous section.

In the previous section, Monte Carlo simulations were performed to understand how the choice of parameters affected the resulting normalized JA hysteresis curve. The normalization allowed for the comparison of the normalized areas of these curves which acted as a gauge of approximately how much wider a curve was compared to another without considering the overall shape of the loops themselves. Using this approach, it appeared that parameters c and k were majorly responsible for the area of the hysteresis curve and an area dense in solutions was found in the $c-k$ plane. This extra information can be useful in estimating parameters for a particular system with hysteresis with knowledge of what normalized area is desired. The particle swarm algorithm in particular is well suited to be modified based on extra information about the desired fitness due to the swarm behavior.

The remnant displacement distribution is found to be approximated by the following exponential equation and forms an upper bound of appropriate solutions for PEA hysteresis.

$$k_u = 0.112e^{2.644c} + 2.644 \times 10^{-9}e^{21.74c} \tag{4.11}$$

From the area distribution, we notice that unlike the remnant conditions, it constrains a lower bound of c.

$$k_l = 0.04517e^{1.989c} + 8.883 \times 10^{-16}e^{36.584c} \tag{4.12}$$

These two boundary functions enclose a large density of solutions that have areas, and remnant displacements that are similar to the ones measured in the PEA. A mean value that lies between the two curves can be generated by adding the two curves together and diving by 2. Using this curve, a modified PSO algorithm can be generated with the curve acting as

an attractor to the particles. The velocity equation in Eq. (4.1) can be modified as follows.

$$\boldsymbol{V}_i(t_{k+1}) = w\boldsymbol{V}_i(t_k) + c_1 r_1(\boldsymbol{p}_B(t_k) - \boldsymbol{X}(t_k)) + c_2 r_2(\boldsymbol{g}_B(t_k) - \boldsymbol{X}(t_k)) + \frac{c_3 r_3}{t_k}(\boldsymbol{p}_D(t_k) - \boldsymbol{X}(t_k)) \tag{4.13}$$

Where $\boldsymbol{p}_D(t_k)$ is a position that points somewhere within the data bounded by eqs. (4.11) and (4.12). All that is known from the data is that there is a higher density of potential solutions within the data found in the Monte Carlo simulations. It's not clear where within the data the particles should be attracted towards. To uniformly explore the space, a random value of c is generated between its bounds and placed into the mean bound function $k(c) = \frac{k_u(c)+k_l(c)}{2}$ to generate coordinate in the parameter space of k. The parameters that are not k or c in $\boldsymbol{p}_D(t_k)$ are kept the same. This random attractive term in the data dense region is useful to direct the swarm into more promising regions but due to the direction varying every iteration, the swarm may tend to lose its ability to explore solutions close to the global and personal best values. This addition to the velocity is then more beneficial early on in the optimization process than it is later on when it may better to investigate more closely to the global minimum. To add this behaviour to the modification, its weight c_3 is divided by each iteration. Early on in the process, the data driven part will have a more prominent impact on the swarm's search but will grow smaller as the search progresses.

Three PSO algorithms are compared for their convergence. The first is an unmodified PSO algorithm dubbed PSO. The second is a PSO algorithm where fitness is done over the normalized JA model instead of the regular JA model dubbed NPSO. Finally, a modified NPSO algorithm is created by adding the data driven term shown in Eq. (4.13). A 5 particle swarm is used with a constant initial condition that is uniform across the parameter space. Fig. 4.10 shows the results of the three PSO algorithms studied. It can be seen that the PSO algorithm performs much worse than the normalized versions. This is because the unnormalized version will always have disagreements in the length of the hysteresis curves

whereas in the normalized version, only the shape and the area of the hysteresis curve is compared in the fitness function. Unlike other authors who modify the fitness to also include area, each assessed solution in the proposed normalized algorithm implicitly compared and the number of solutions that are close to the experimental data is augmented. Comparing the NPSO with the NMPSO, it can be seen that the additional data-driven term helps the particle swarm find better solutions sooner than the NPSO and augments the chance that the algorithm converges to a better solution. It can be seen that the modification did not significantly affect the convergence time after 100 iterations compared to the NPSO. It should be noted that these improvements show improvements for a PSO strategy with a small number of particles. For a large number of particles, it may not show significant improvement over the NPSO method for a large number of particles because the particles will cover a larger portion of the parameter space and may start close by chance. However, the reduction of particles in the PSO algorithm is desirable because it reduces the amount of calculations that are performed in every iteration.

Considering computational time, each solution is made up of a JA model calculation on an input vector containing 10^5 points. Each iteration, a particle must updates its position and calculates a new solution at that point representing calculations on the order of 10^5. The number of particles then increases the computational time linearly representing $N10^6$ arithmetic computations where N is the number of particles. The NMPSO shows that it improves convergence for a smaller number of particles and thus can conserve computation time.

4.4 Prandtl-Ishlinskii Curve Scaling

The PI model has appealing straightforward geometric interpretations that allow for the calculation of parameters of the model to suit the system being modeled. However, extensions

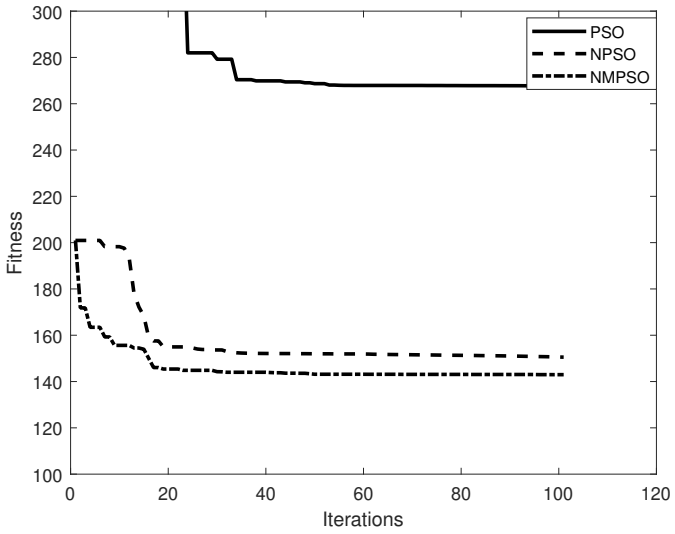

Figure 4.10: Fitness results between the PSO, NPSO, and NMPSO

of the model create difficulties in this process and if the model requires many parameters to achieve appropriate levels of accuracy, recalculation of hysteresis parameters can become costly if the shape of the hysteresis has a tendency to change. In this section, a rescaling process that exploits some properties of the PI model to efficiently change the width of the hysteresis curve while preserving the shape is proposed.

As mentioned in Section 2.1.1, the PI model can be thought of as a series of linear pieces with different slopes and the slope of an individual section is determined by its coefficient as well as the coefficients associated to all thresholds that came before that part. The PI model has the following properties

I. The PI model possesses the homogeneity property on its parameters c_i. In other words, the following equation is valid for the PI model

$$H(u, \alpha \boldsymbol{c}) = \alpha H(u, \boldsymbol{c}) \tag{4.14}$$

From this homogeneity property, scaling the hysteresis curve by a factor of α is the

same as scaling all all parameters by a factor of α.

II. The PI model possesses an odd symmetry property with respect to its parameters. The following equation is valid

$$H(u, -\boldsymbol{c}) = -H(u, \boldsymbol{c}) \tag{4.15}$$

This property is in fact a result of the first property when $\alpha = 1$ and can be used to reduce parameter estimation searches if they are conducted on the PI model.

III. Coefficient c_0 has the following additive property on the derivative of the hysteresis curve with respect to the input

$$\frac{dH(u, c_0 + \alpha, c_1, ...)}{du} = \alpha + \frac{dH(u, c_0, c_1, ...)}{du} \tag{4.16}$$

This property comes from the geometrical interpretation of the coefficients being associated to the slopes of the line functions that approximate the hysteresis curves. The parameter c_0 represents the first slope of the linear function from $[0, r_1]$ and successive slopes add or subtract to this "original" slope.

The goal now is to exploit the properties above to design a modeling scheme that can easily adjust a given hysteresis curve to a new hysteresis curve that better represents the system that is being modeled. This situation is useful for PEA applications. For example, when the frequency of the input is increased, it is observed that the hysteresis curve widens due to the rate-dependent nature of the PEA hysteresis. In addition, temperature affects the width and the stroke length of the PEA hysteresis curves. The width tends to shrink as temperature increases due to phase change that occurs at the Curie temperature. Past the curie temperature, the PZT unit cells cannot stably hold the Ti atom in a polarized position without external forces. This translates to a situation where above the curie temperature, the

polarization is dictated by a mainly reversible process which minimizes the overall hysteresis and approaching such a temperature gradually decreases the hysteresis in the system.

From property 1, it is possible to normalize PI hysteresis curves like was done to JA hysteresis curves in the previous section. Using this, the stroke length of the hysteresis curve can be set to an arbitrary length and the shape of the curve and general width in the normalized space remains the same. However, from property 3, tuning the parameter c_0 tunes the overall slope of the hysteresis curve and stretches it along its length. This process does not preserve the width in the normalized space. This can be seen by calculating what multiplicative factor adding α to c_0 has on the overall slopes of each section of the hysteresis curve. For the first linear function between values $0, r_1$ in the $u - y$ space, the multiplicative increase in slope by adding α to c_0 is the following.

$$\frac{dH([0, r_1], c_0 + \alpha, c_1, ...)}{du} = (\alpha + c_0) = (\frac{\alpha}{c_0} + 1)c_0 \tag{4.17}$$

For an arbitrary segment $[r_i, r_{i+1}]$, the same process yields the following

$$\frac{dH([r_i, r_{i+1}], c_0 + \alpha, c_1, ...)}{du} = (\alpha + \sum_{j=0}^{i} c_j) = (\frac{\alpha}{\sum_{j=0}^{i} c_j} + 1) \sum_{j=0}^{i} c_j \tag{4.18}$$

Hence, the factor by which the slopes are scaled by changing only c_0 depends on the original value of the slope and thus is generally different for all sections. However, the rate of change of the hysteresis curve in general is constant. This implies that the shape of the overall hysteresis curve doesn't change. Only its slope components do. This stretches the shape of the hysteresis over a longer or shorter hysteresis free line. To characterize the area change between the two curves, the peak value of the hysteresis curve is calculated as follows with $r_{N+1} = u_{max}$

$$H(u_{max}) = \sum_{i=0}^{N} \sum_{j=0}^{i} c_j (r_{i+1} - r_i) \tag{4.19}$$

If c_0 is increased by α then the peak of the curve changes to the following.

$$H_\alpha(u_{max}) = H(u_{max}) + N\alpha r_1 \tag{4.20}$$

To obtain the area under the curve of the forward moving curve in the PI model, it can be done by calculating the area under each line segment which creates a trapezoid as shown in Fig. 4.11. For a monotonically increasing input from $[0, u_{max}]$, the area A can be calculated as follows.

$$A = \sum_{i=0}^{N}(r_{i+1} - r_i)(\sum_{j=0}^{i} c_j(r_i - r_j) + \sum_{j=0}^{i+1} c_j(r_{i+1} - r_j)) - u_{max}H(u_{max}) \tag{4.21}$$

The area of the PI curve when c_0 is increased by a factor of α, A_α, can be expressed as a function of the original area.

$$A_\alpha = A + (N\alpha r_1 u_{max} - \alpha \sum_{i=0}^{N}(r_{i+1}^2 - r_i^2)) \tag{4.22}$$

Finally, to scale this new curve down to its original length, coefficients can be multiplied by a factor of $\frac{H(u_{max})}{H_\alpha(u_{max})}$ and the areas scale down by the same proportion by virtue of Property I. Thus, the area of a PI model with coefficients $\frac{H(u_{max})}{H_\alpha(u_{max})}[c_0 + \alpha, c1, c2, ...]$ can be expressed in terms of the original coefficients as follows

$$A_{rescaled} = \frac{H(u_{max})}{H(u_{max}) + N\alpha r_1}(A + (N\alpha r_1 u_{max} - \alpha \sum_{i=0}^{N}(r_{i+1}^2 - r_i^2))) \tag{4.23}$$

The rescaling process is illustrated in Fig. 4.12. In this figure, subfigure a) shows the original hysteresis curve modeled by some PI model. Subfigure b) shows the effect of adding to the hysteresis free parameter, some factor α. If all coefficients of this new PI hysteresis model

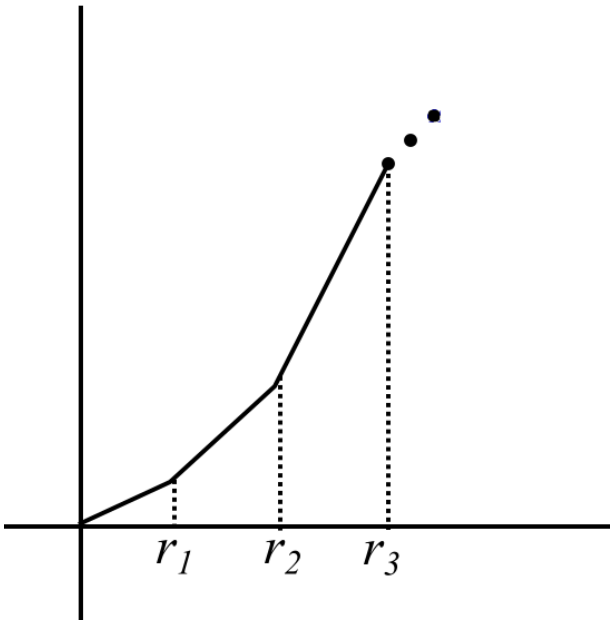

Figure 4.11: Calculating the area under the curve of the forward curve in the PI model

are then scaled by a factor $H(u_{max}/H_\alpha(u_{max})$, then the max output of the new hysteresis curve produced by this process will coincide with the original hysteresis curve, but its hysteresis area will be altered as is shown in subfigure c). The main appeal of this process is that a desired area of a hysteresis curve can be achieved sequentially by modifying only a single parameter in the PI model and rescaling the resulting curve. This process can be useful in applications where the hysteresis curve may widen or narrow depending on certain processes. This is the case with PEAs where an observed widening of the hysteresis curve is found when the frequency is increased and a narrowing occurs when the temperature increases.

To examine the effectiveness of this method for adjusting modeled PI modeling parameters to curves of different frequencies, PEA hysteresis curves are generated at different frequencies using the P-753 LISA actuator. Optimal parameters are calculated in a 80 parameter PI model with thresholds ranging from 0 to 8 with increments of 0.1. Initial PI model parameters are found for the 10 Hz case and a mean RMS error is calculated. To find optimal values of α that represent the new hysteresis area, the area of the new hysteresis curve is calculated

and Eq. (4.23) is used to find an α value that generates an area of the desired magnitude. Fig. 4.13 shows the PEA hysteresis with the rescaled hysteresis described in this section. It can be seen that PEA hysteresis widens with frequency which would require a refitting of hysteresis curves to describe at all frequencies. The rescaled PI model shows good scaling in area to the measured hysteresis curves. However, as frequencies get higher, it can be observed that the shape of the rescaled PI curves doesn't agree as well with those of the PEA. This is especially apparent in the lower half of the hysteresis curves.

Fig. 4.14 shows the mean RMS error when compared with a static PI model and the adjusted hysteresis using the proposed scaling process. It can be seen that rescaling the hysteresis to the width of the new curve significantly reduces the speed at which errors begin accumulating in the modeled system. Fig. 4.15 shows the expected negative trend for α to track the area of the PEA hysteresis. Since the area grows larger, α must take stronger negative values as the frequency increases.

In this chapter, a set of JA solutions with randomized parameters is generated to study statistics in the parameter space of the model to find trends to facilitate parameter estimation. It was found that parameters c and k are the most responsible for the modifications of hysteresis area and remnant strain. A modified PSO algorithm is developed to leverage the statistical trends found and to help solutions converge faster with fewer computations. Additionally, a parameter rescaling method is developed for the PI model which allows for the scaling of PI hysteresis area to a desired value by modifying a single parameter in the model and rescaling to the original length. The rescaling procedure is then used to describe frequency dependent broadening of PEA hysteresis.

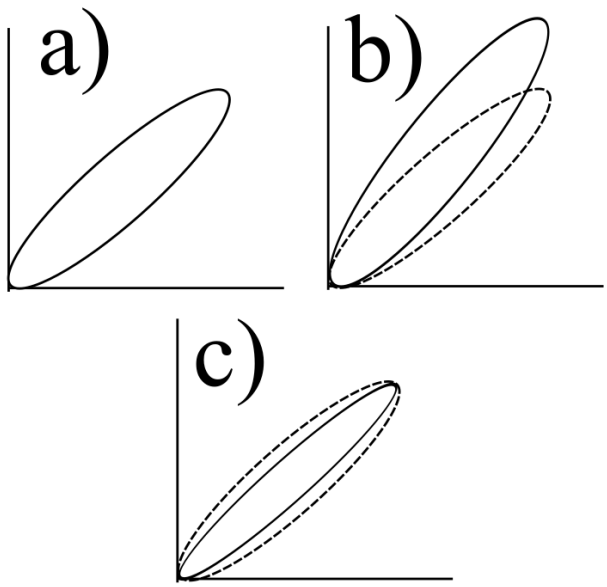

Figure 4.12: PI curve scaling procedure. a) The original hysteresis loop. b) c_0 is changed. c) The hysteresis length is rescaled to its original length.

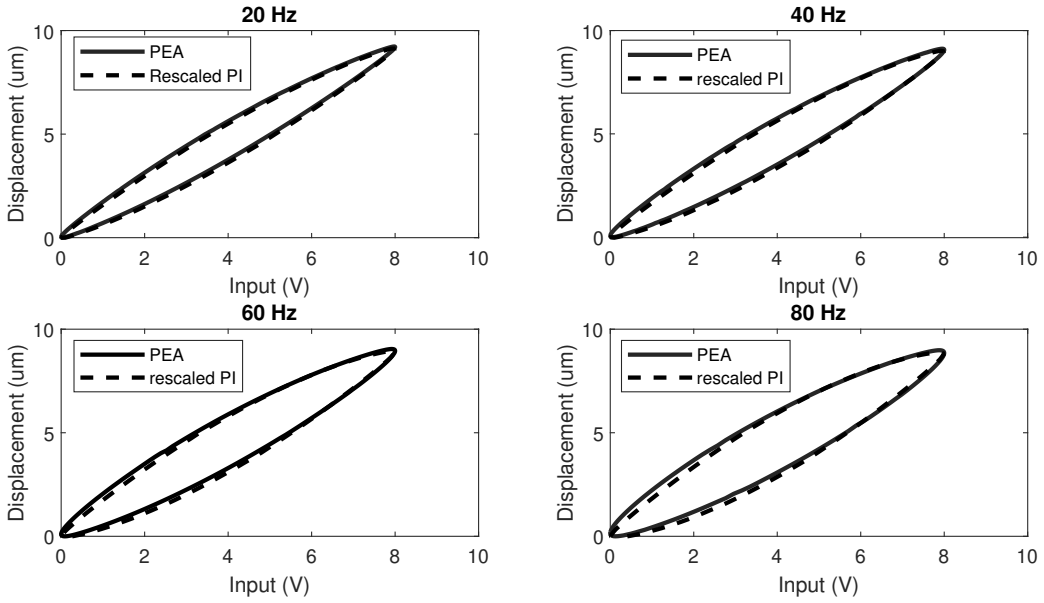

Figure 4.13: Frequency dependent hysteresis modeled using the PI curve scaling process

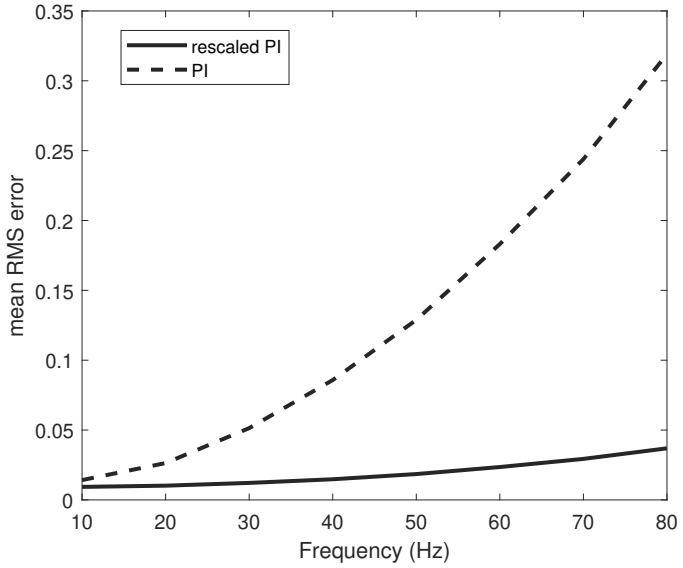

Figure 4.14: Mean RMS error between measured and modeled hysteresis curves comparing static and scaled PI models

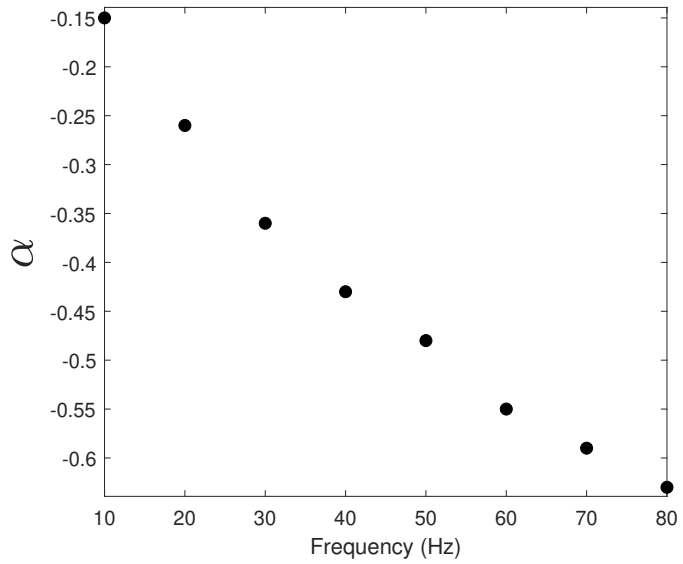

Figure 4.15: Values of α that generate hysteresis areas similar to the measured areas

Chapter 5

Temperature-Dependent Modeling

PEAs are used in many diverse applications, some of which are subject to changes in the environment. In certain microscopy applications, a temperature induced structural change may be interesting to observe. In atomic force microscopy, PEAs are often used to position the scanning needle utilized in these devices. For structural monitoring, piezoelectric sensors must perform in seasonal temperatures which could represent significant temperature swings.

The external environment can affect the PEA performance in a variety of ways. Most notably for temperature, the position of the PEA system will change as temperature is varied. This effect is extremely important for PEA systems because the thermal contractions and expansions of the system can be very large in comparison to the electromechanical positioning range of the PEA system. The treatment and compensation of these thermal deformations has been discussed in a number of papers. For piezoelectric devices used as sensors, these deformations can lead to sensor errors. Thermal compensation of piezoelectric dynamometers is treated in [83] where the thermal expansion of the piezoelectric material is treated linearly. In [84], a physical approach to temperature-based changes to piezoelectric sensors for structural health monitoring is proposed. This approach once again assumes linear dynamics of the PEA actuator with a first order approximation for the temperature

dependence an does not address the nonlinearities in the PEA system themselves. Data-driven approaches to this problem such as those found in [85] generate good results over the range of temperature values required but provide no cause to the change making it difficult to use existing data for other systems and no understanding of how data changes with the change of system parameters. In other applications, the thermal contributions are compensated passively through the system itself. In [49], a piezoelectric energy harvester is passively compensated to retain similar vibrational properties over an extended temperature range. Balancing of thermal expansion coefficients is used to compensate temperature expansions on a Fabry-Perot spectrometer etalon is performed in [86].

Temperature-based modeling on specific piezoelectric non-linearities has not been extensively studied in the literature. For temperature-compensated hysteresis modeling, an extended PI model is proposed to compensating temperature effects by adding temperature dependent terms to all operators within the PI model, a temperature component [87]. While this approach can generate good temperature agreement in hysteresis curves, it complicated parameter estimation by adding an increased layer of complexity on the already large number of parameters required to be estimated for good hysteresis agreement and the process itself is entirely phenomenological.

It should be noted that ferroelectric PEAs are also pyroelectric and thermal effects could be modeled to include these effects. However, at static temperature, the pyroelectricity does not come into play. It is instead related to the thermal displacement which is neglected in this model. The electrocaloric constant in PZT thick films was measured to be 0.06×10^{-6} $\mathrm{K} \cdot \mathrm{m/V}$ in [88]. Assuming a similar constant in the PEAs used in this study, temperature variations across the full range of the PEA input would not exceed 0.06°C which is considered negligible in this study. Thus, pyroelectric effects can be considered negligible and only piezoelectric and ferroelectric effects are considered. In fact, the modeling presented in this section can be thought of as a nonlinear model for the piezoelectric constant because they

create a nonlinear capacitor term that represents a linear piezoelectric constant.

In this section, some results on temperature dependent observations in PEAs are shown. An alternative approach to temperature-dependent modeling of PEA hysteresis is shown that is based on the nonlinear capacitance properties of the PEA. This method is simpler than existing approaches and the parameter estimation complexity does not scale with the number of parameters used in the model.

5.1 Experimental System

The experimental system used in temperature based experiments is once again based at its core on the Quanser QPID-e data acquisition device relaying information between MATLAB Simulink and the PEA system described by the E-625 piezoservo controller utilized in open loop mode and acting as a voltage amplifier for the P-753.1CD LISA actuator acting as the PEA. Added to this system is a vacuum oven equipped with a thermal controller as seen in Fig. 5.1. The oven used is the Superland DZF-6020 vacuum oven with digital temperature controller. The oven has a temperature range of 40°C to 250 °C which is suitable for the PEA system utilized which has a maximum rated temperature of 80°C. The oven temperature sensor is non-detachable and is placed within the chamber. However, oven temperature does not reflect the true temperature of the PEA system. Fig. 5.2 shows the PEA setup within the oven. The PEA stage is placed on top of a copper block to help distribute the heat from the elements evenly. Close to the oven elements, a fan is used to circulate heated air through the oven. Attached to the PEA are 3 digital DS18b20 thermal sensors. The probes are attached to the PEA using kapton tape and a placed along the enclosure. The distribution of the probes can be seen in Fig. 5.3.

The oven characteristics may have overshoot if the control parameters are not selected properly. Fig. 5.4 shows the temperature curves when the oven is set to a value of 50°C. It is

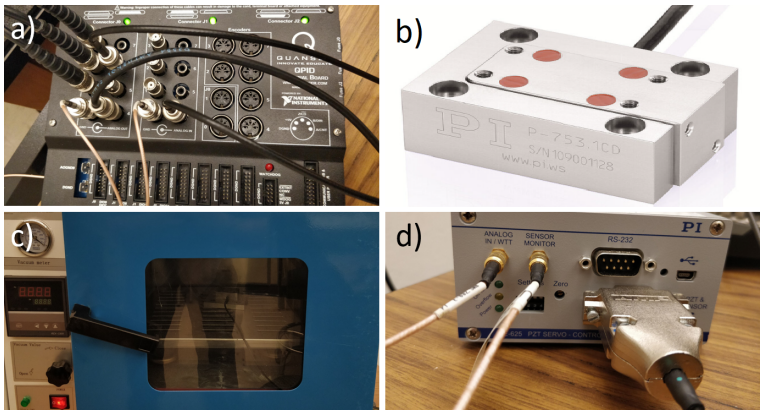

Figure 5.1: Experimental system. a) Quanser QPID-e b) P-752 PEA c) Oven d) E-625 amplifier

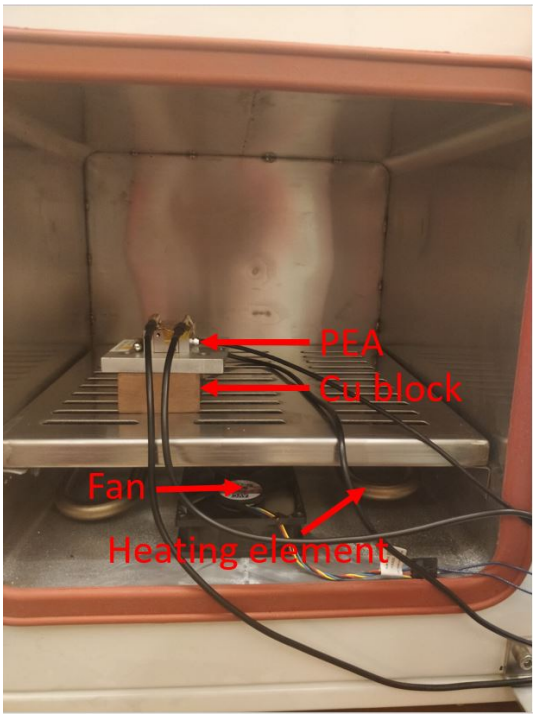

Figure 5.2: PEA setup within the oven

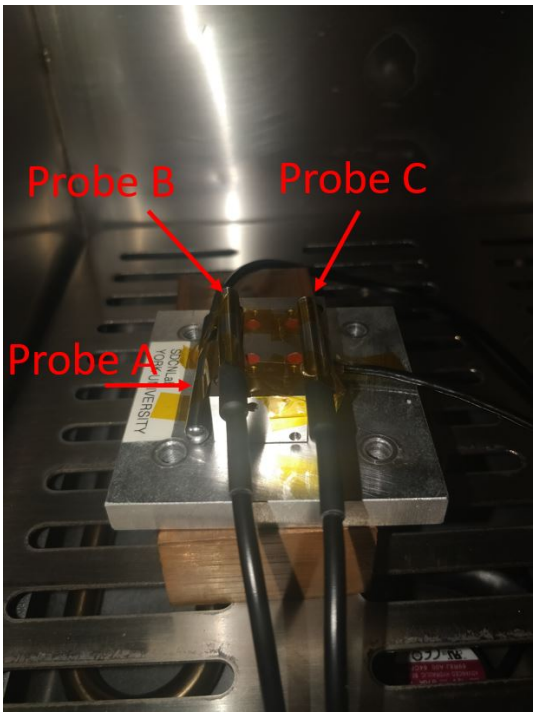

Figure 5.3: PEA setup within the oven

seen that all three temperature probes converge to a similar value. Probe A initially senses temperatures that are lower than those sensed by probe B and probe C. This may be due to being in contact with a larger amount of the stainless steel enclosure of the PEA system.

One possible concern about temperature-based PEA tests is the thermal performance of the sensor used. The PEA system utilizes a capacitive sensor that senses position in the PEA system by forming an air capacitor between the probe and the target. The measured capacitance of this system is directly related to the spacing of these plates and with stretching or shrinking, the plate distance is varied. The largest source of error that can come from this system is from the thermal expansion of the sensor plate material which contributes to an error of about 2 nm/°C. However, these fluctuations are only truly important if temperature is varied during operation. At steady state temperatures, these errors do not move and instead only demand a zero point recalibration from the user. An additional source of error that can be important in steady state operation comes from the bowing effect that can

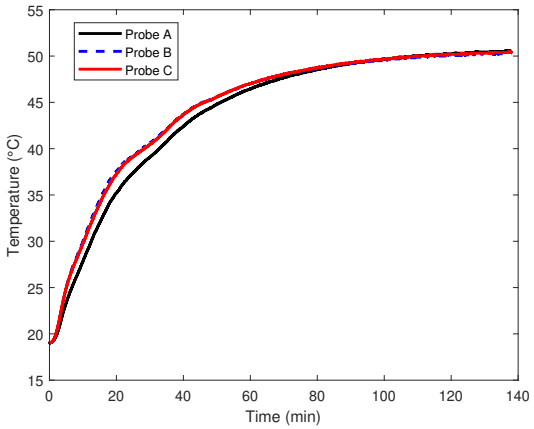

Figure 5.4: Settling time of the oven used in PEA experiments on 3 probes

happen if the thermal expansion properties of the plate materials is mismatched with the expansion properties of the mounting material. Fig. 5.5 illustrates the effect of bowing due to a mismatch in thermal expansion coefficients α_A, α_B. If the base material possesses a larger thermal expansion coefficient than the sensor plate, then inward bowing can be observed. If the vice-versa is true, outward bowing can be observed the the plates. The plates are assumed to be parallel and flat and therefor any significant bowing will add some nonlinearity to the probe readout. However, it is assumed that this effect is not significant at the temperature range that is being utilized.

5.2 Temperature-Extended Asymmetric Prandtl-Ishlinskii model

In this section, a temperature extended asymmetric Prantl-Ishlinskii (TAPI) model is described to compensate for PEA hysteresis across a range of temperatures. This temperature extension is inspired by physical modeling of electromechanical systems.

When a piezoelectric material is in the presence of an electric field, it's body is deformed

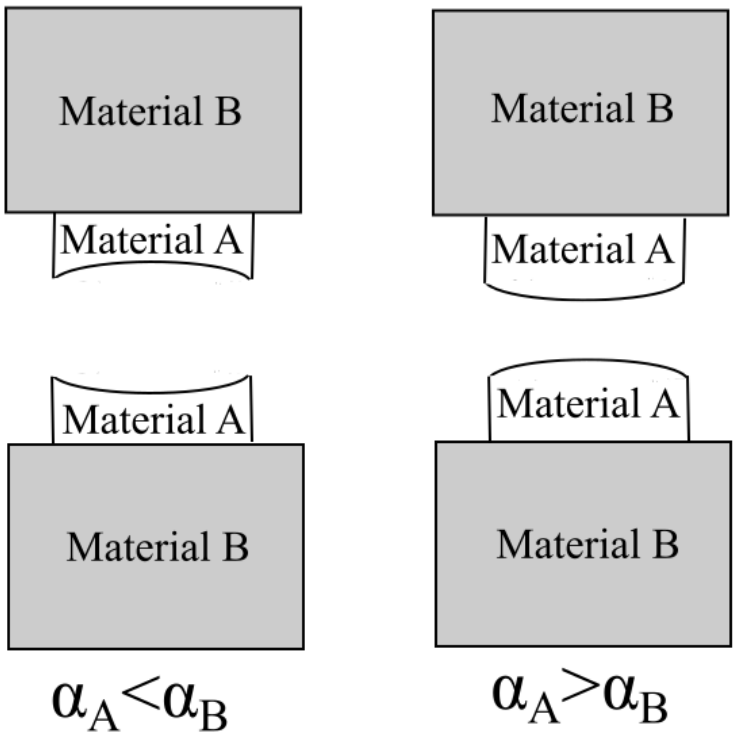

Figure 5.5: Capacitive sensor thermal bowing.

and a strain is induced. This effect can be described as an electromechanical coupling which allows for energy transfer from the mechanical domain to the electrical domain and vice-versa. The mechanical displacement of the PEA can be modeled as a second order mass-spring-damper system responding to an external force.

$$m\ddot{x} + c\dot{x} + kx = F_{ext} \tag{5.1}$$

Where x is the displacement, m is the mass, c is the damping coefficient, k is the stiffness coefficient, and F_{ext} is the external force acting upon the system.

The external force acting on the PEA caused by the electromechanical coupling can be described by an electromechanical transformer coefficient T_F which transforms the voltage u_T applied to the transducing component to a force. In the absence of any additional force

terms, the external Force can take the following form.

$$F_{ext} = T_F u_T \tag{5.2}$$

The expression for the external force on the PEA system is complex due to the transducer voltage being different than the applied voltage u. Hysteresis is a very commonly reported nonlinearity is present between the applied voltage and the PEA displacement. However, observations have shown that this hysteresis is not present between the charge that accumulates on the PEA plates and applied voltage. A transformer equation can be set up for the PEA position vs its charge as follows

$$q_T = T_q x \tag{5.3}$$

Where q denotes the charge on the transducer, and T_q is the electromechanical transformer between charge and displacement.

In the electrical domain, the PEA is a primarily capacitive element. However, due to the ferroelectric nature of the PEA, energy is lost through pinning sites in the material when it is electrically excited to move charges across the plates. This effect creates an energy loss which can be described as a nonlinear impedance in the electrical system. Fig. 5.6 shows the electromechanical model for the PEA system. Such a model was used by Goldfarb and Celanovic to describe the Maxwell resistive capacitor model for hysteresis [89]. This model represents a lumped parameter model of the system with a single nonlinear impedance characterized by the H block. This hysteresis block can be modeled by any hysteresis model and creates a voltage divider circuit between the hysteresis of the system and the capacitive and transducer elements. Once the current crosses the hysteresis block, it is itself divided between transducing elements and capacitive elements. From Kirchhoff's laws, the following

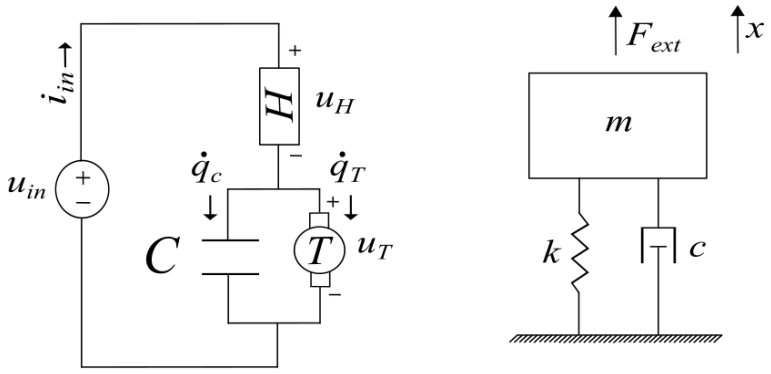

Figure 5.6: Electromechanical model of PEA

equations are derived.

$$u_{in} = u_H + u_T \tag{5.4}$$

$$i_{in} = \dot{q}_C + \dot{q}_T \tag{5.5}$$

The right side of Fig. 5.6 is the mechanical domain of the PEA. Most PEAs have comparatively high stiffness compared to their damping and mass terms and for low frequency excitations, this stiffness term is dominant in the force expression. To describe the mechanical movement of the PEA, Eq. (5.1) can be approximated to be as follows for low frequencies.

$$kx = F_{ext} \tag{5.6}$$

Eq (5.5) describes how the charge is shared between the transducer block and the capacitor block. In an ideal capacitor, C remains constant and the transducer charge can be described as $q_T = q - u_T/C$. Later in this section, the nonlinear effect of domain reorientation is described which makes this case a nonlinear capacitor.

It should be remarked that the PI model is related to the electromechanical model for the following reasons. Firstly, the electronic system from Fig. 5.6 can be reduced to an equivalent capacitor component C_{eq} which accumulates a charge q in response to a voltage

$u = u_{in}$. Thus, $q = C_{eq}u$. q is related to the displacement x and the following expression can be derived by utilizing Eqs. (5.2)-(5.5)

$$q = T_{eq}x = (\frac{Ck}{T_F} + T_q)x \tag{5.7}$$

An expression for x as a function of u then requires an understanding of the equivalent capacitance of the circuit. Assuming that the impedance block H is made up of capacitors in series that are modeled using the PI model, e.g. each capacitor acts as a short circuit and is switched on if an input exceeds its threshold, then assuming each component contributes a capacitance C_i to the block, the total potential across the H block can be written assuming m capacitors are turned on.

$$u_H = q\sum_{i=1}^{m}\frac{1}{C_i} \tag{5.8}$$

Forming an equivalent capacitor with the effective capacitor created from blocks C and T can be done by utilizing Eq. (5.5). Combining it with the capacitance term from Eq. (5.8) yields an expression of the form $q = C_{eq}u$ where C_{eq} is expressed as follows.

$$C_{eq} = \frac{(C + \frac{T_qT_F}{k})\sum_{i=1}^{m}\frac{1}{C_i}}{C + \frac{T_qT_F}{k} + \sum_{i=1}^{m}\frac{1}{C_i}} = \sum_{i=1}^{m} c_i \tag{5.9}$$

Eq. (5.9) is shown to shares the same structure as Eq. (2.9) and justifies the interpretation of PI parameters representing capacitance values and a model of the form $x = H(u)$ can be established.

To describe the force term, it's important to have a suitable model for the hysteresis of the system to have a good approximation of the voltage on the electromechanical transducer. The PI model described in Section 2.1.1 can be used. However, the electromechanical model provides a means of interpretation on what the the PI model represents. The PI parameters are parallel breakaway forces that require certain amounts of energy before contributing to

the full force. The thresholds in the PI model are then zones where Coulomb frictions are dominant and before the input provides a force strong enough to overcome the zone of static friction for a particular operator, no force contribution is added into the system. Once the threshold is attained, the PI output is linear with respect to the input. The c_i parameters can then be interpreted as stiffness in the mechanical domain. In the electrical domain, the charge vs voltage relationship is the parameter space of this evolution. In the electrical domain, the coefficients represent capacitance with c_0 representing a linear case of capacitance while the thresholds correspond to a pinning type effect similar to Coulomb friction. In fact, this effect is very similar to what is used to create the JA model. The JA model is based on the idea that domain walls can be pinned and prevented from moving until the pinning sites are broken. This physical interpretation of the PI model in the electrical domain can be used to extend the PI model to a modified PI model. For example, the the classical PI model, the capacitor term is considered to be ideal and linear. A modification of this c_0 term in the PI model can yield hysteresis curves that more accurately model the PEA hysteresis. It is known that PEA hysteresis is asymmetric and that the classical PI model can only describe symmetric hysteresis. However, if the hysteresis-free term in the PI model is chosen such that it is an odd function, then more interesting behavior can be characterized.

Let $g(u(t))$ be an odd, Lipshitz coninuous function that is added to the memoryless component of the classic PI model. An asymmetric PI model can be written as follows

$$H(u) = g(u(t)) + \sum_{i=1}^{n} c_i F_{r_i}[u](t) \tag{5.10}$$

The function $g(u(t))$ generates asymmetric hysteresis as long as $\frac{dg(u(t))}{du}$ is not constant. The reason this occurs is that if the slope of the hysteresis-free curve is not constant, then the slope of the section of the curve between two successive threshold values $[r_i, r_{i+1}$ modifies a section of this the hysteresis free function $g(u(t)) + c_1 F_0[u](t)$ going forward. However, when

the input is varied backwards, slope modifications between those two thresholds now acts on a different part of the hysteresis free curve. Hence, symmetry is only guaranteed if the slope of the hysteresis free curve is the same everywhere.

It's clear that the addition of a more generalized odd function generates asymmetric hysteresis curves and this form of modification has been reported in the literature [90]. The next step is to choose a suitable odd function to model the behavior of the PEA system. From the observation that the memoryless function that embeds the PEA hysteresis corresponds to a capacitor, this function can be chosen such that it models a nonlinear capacitor. In section 2.1.2, the rotation of the domains inside the PEA were described to create the JA model. In particular, a hysteresis-free term for the anhysteretic polarization was written in Eq. (2.20). Keeping the temperature term, the anhysteretic polarization of the PEA can be written as follows.

$$P = P_s \tanh(\frac{u}{aT}) \tag{5.11}$$

The added polarization changes the permittivity of the PEA and contributes to the charge of $q_C = Cu_T + q_P$ where $q_P = P_s \tanh(\frac{u}{aT})$ are the bound charges that are added due to the reorientation of the polarization vector towards the electric field direction. The total charge as described by Eq. (5.5)

$$q = q_C + q_P + q_T \tag{5.12}$$

From Eqs. (5.9), (5.11), and (5.12), the charge of the system can be written as

$$q = \sum_{i=1}^{m} c_i u + P_s \tanh(\frac{u}{aT}) \tag{5.13}$$

From Eq. (5.13) and comparing it to Eq. (5.10), it is clear that Eq. (5.11) is a suitable candidate function for $g(u(t))$.

From Eq. (5.11), the temperature dependence already naturally appears. However, further temperature dependence can be added. When a PEA undergoes a temperature change, its ferroelectric properties change. In PZT ceramics, it has been reported that remnant polarization, saturation polarization, and coercive field decay with temperature [91]. If temperature is not kept constant, then temperature effects can impact the structure of the hysteresis by contributing to unpinning for example. In the JA model, to track these changes brought by temperature, an extended model was later developed with temperature dependent parameters [92]. Fig. 5.7 shows an illustration of some of the changes that occur when the temperature is increased. Here. T_c refers to the Curie temperature which acts as a threshold temperature between the phase transition between ferroelectric and paraelectric states. E_c designates the coercive field value which moves towards 0 as the temperature approaches T_c. The saturation polarization gets smaller as well as temperature increases. The saturation polarization can be modeled according to the following using Weiss domain mean field theory [93].

$$P_s(T) = P_s(0)\left(1 - \frac{T}{T_c}\right)^{\beta} \tag{5.14}$$

Here, β is called the critical exponent and characterizes the approach to the phase transition. $P_s(0)$ specifically is the saturation polarization when the temperature is at absolute zero. The following equation is chosen to characterize the hysteresis of the PEA.

$$H(u(t), T) = c_1 P_s(0)\left(1 - \frac{T}{T_c}\right)^{\beta} \tanh\left(\frac{u(t)}{aT}\right) + c_1 F_0[u](t) + \sum_{i=2}^{n} c_i F_{r_i}[u](t) \tag{5.15}$$

Eq. (5.15) is a temperature-dependent, asymmetric PI model dubbed the TAPI model. Note that this equation has its temperature contributions confined to the asymmetric part of a hysteresis-free component of the asymmetric PI model. In the TAPI model, parameter estimation is slightly less straightforward compared to the classic PI model due to the fact

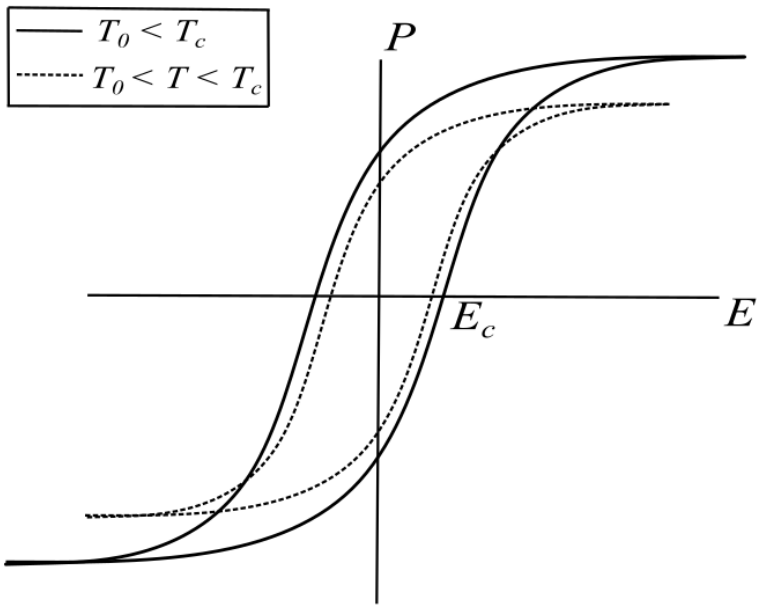

Figure 5.7: Effect of temperature of the P-E hysteresis in ferroelectric materials.

that the slope of the hysteresis curve changes due to the temperature dependent component. To find new parameters suitable for the TAPI model, parameters P_s and a are optimized while rescaling classical coefficients c_i into new coefficients c_i^* suitable for the TAPI model. Using this method, the burden of parameter estimation is confined to two parameters in the asymmetric term while the hysteresis contributing parameters are systematically readjusted. An initial fit of the hysteresis curve using the PI model is performed to find optimal parameters that describe the forward moving hysteresis curve by taking $P_s = 0$. Afterwards, assuming no temperature dependence initially on P_s, parameters P_s and a are adjusted until the best fit is achieved while adjusting all hysteresis contributing parameters to the new slope of the hysteresis curve as follows.

$$c_i^* = \sum_{j=1}^{i} c_j - c_1^* \frac{Ps^2}{a} (r_i/a) - \sum_{j=2}^{i-1} c_j^* \tag{5.16}$$

Parameters C_i^* are analytically adjusted parameters based on the classical PI model

parameters.

One of the major advantages of modeling hysteresis using the PI model is that there exists an analytical inverse that is itself a PI model. By applying the inverse model to the input signal, the hysteresis of the system can be canceled with a proper modeling description. However, the regular inversion process of the classical PI model does not apply to the TAPI model due to the hysteresis-free curve not being constant. However, because there exists a classical PI model embedded into the TAPI model, an iterative process can be used to find the hysteresis inverse. Fig. 5.8 shows a block diagram of the proposed hysteresis compensator for the TAPI model. The TAPI model is a superposition of the classical PI model with

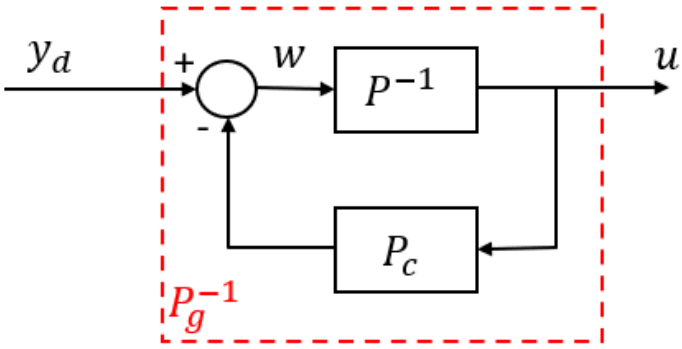

Figure 5.8: TAPI compensator block diagram

a nonhysteretic part that includes asymmetric effects as well as temperature effects. The output y_g can be expressed as the following sum.

$$y_g = P_g[u](t) = P[u](t) + P_c[u](t) \tag{5.17}$$

where P is the classical PI model and $P_c = c_1 P_s(0) \left(1 - \frac{T}{T_c}\right)^{\beta} \tanh\left(\frac{u}{aT}\right)$. A compensator P_g^{-1} is designed based on Fig. 5.8 that includes an inverse classical PI model P^{-1} with a feedback element that includes the P_g term that describes both asymmetry and temperature contributions. This compensator creates an input signal u that can be inputted to the plant

to cancel its hysteresis and generate a desired output y_d. To determine the operators that constitute P^{-1}, utilising the fact that an inverse classical PI model is also a classical PI model, we seek an expression in the following form.

$$P^{-1}[u](t) = \hat{c}_1 w(t) + \sum_{i=2}^{n} \hat{c}_i F_{\hat{r}_i}[w](t) \tag{5.18}$$

Here, $\hat{c}_i$ are the inverse coefficients and $\hat{r}_i$ are the inverse thresholds that are different from those in the uninverted case. These coefficients can be determined analytically from the classical PI model as described in Section 2.1.1. The inverted TAPI model is interesting because the temperature and asymmetric effects are not present in the hysteretic elements of the classical PI model. This implies that the hysteretic parameters only need to be found once and the parameters for the temperature extension are found independently.

The TAPI model is tested on a variety of input ranges and a variety of temperatures. To generate a threshold vector, the input range is divided into increments of 0.1 V generating a set of values in the interval [0, 8], which is the input range studied in this case. Fig. 5.9 shows the input/output behaviour of the PEA system. The equation that describes the input signal $u(t)$ can be described as follows.

$$u(t) = \frac{\text{floor}(t)}{2}(1 + \sin(2\pi f t - \frac{\pi}{2})) \tag{5.19}$$

Where floor(t) is the floor function applied to the time that generates an integer amplitude that increases with time, and f is the frequency chosen to be 5 Hz in these experiments. The input is sent to the E-625 amplifier and amplified 10x before it is applied to the PEA. When the PEA output is plotted against the input described by Eq. (5.19), the bottom figure in Fig. 5.9 is generated which shows a hysteresis curve with many minor loops. The top figure shows the input signal vs. time as an incrementing sine wave, as well as the PEA response. The

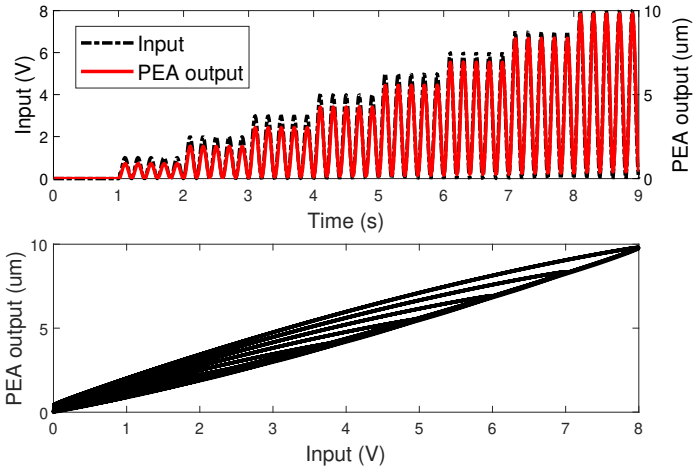

Figure 5.9: Open loop output of PEA system at room temperature and hysteresis curve showing minor loops.

input was chosen so that a number of minor loops would be present to increase the accuracy of the modelling throughout the voltage range of the PEA system. The bottom figure shows the PEA hysteresis generated from the input/output data. In this figure, the input returns to zero, but the output retains some remnant displacement due to memory effects.

PEA hysteresis behaviour is initially fitted using the classical PI model to obtain a set of parameters $\mathbf{c}$. Since a variety of input signals are used, the problem of remnant strains accumulating as the input range for a period is changed can create errors if they are not accounted for. To describe this behaviour, the initial conditions of the OSP operators must be chosen so that the desired behaviour is achieved. Initial conditions w_0 are determined considering the local minima in the output data $\min(\mathbf{y})$ and the minima generated by the classical PI model $\min(\mathbf{y}_P)$. Optimal w_0 are found by minimising the following function.

$$M = \sum_{i=1}^{N} \left(\sqrt{(\min(\mathbf{y}_P) - \min(\mathbf{y}))^2} \right) \tag{5.20}$$

Here, the sum is over the N local minima in the data. To convert the classical PI model to an asymmetric model, see Eq. (5.16) used in conjunction with minimising model data

points y_i^m with measured data points y_i to minimise M.

$$M = \sum_{i=1}^{N} \left(\sqrt{(y_i^m - y_i)^2} \right) \tag{5.21}$$

Fig. 5.10 shows the result of the PEA hysteresis fitted after adjustment to the asymmetry and incorporation of the correct initial conditions. This process produces values for the parameters P_s and a at the temperature at which the experimental data were collected. To complete the identification of the TAPI model, only β remains to be identified. An efficient way to find β is by the variation in the maximum displacement, which varies greatly with temperature. Let $\max(\mathbf{y}_T)$ be the set of local maxima of the modelled TAPI model at all temperatures and $\max(\mathbf{y})$ the corresponding measurements at these locations. β is found by minimising the following M

$$M = \sum_{i=1}^{N} \left(\sqrt{(\max(\mathbf{y}_T) - \max(\mathbf{y}))^2} \right) \tag{5.22}$$

The identification procedure for the TAPI model builds on the appealing parts of the classical PI model to minimise the parameter estimation burden on this new and more complex model. The initial step of the process is to find the best PI model, and subsequent steps sequentially add tweaks to this process to identify the remaining parameters that were added in the TAPI model.

With suitable parameters identified, the performance of the TAPI model can be verified. Hysteresis loops at multiple input ranges are creates at temperatures from room temperature to 70°C. Fig. 5.11 shows that the TAPI model continues to describe the measured data at all temperatures within the range. Most notably, the TAPI accurately models the changes in peak displacement which changes with temperature while also maintaining accurate loop shape despite changes with temperature. Fig. 5.12 shows only the peak displacement values

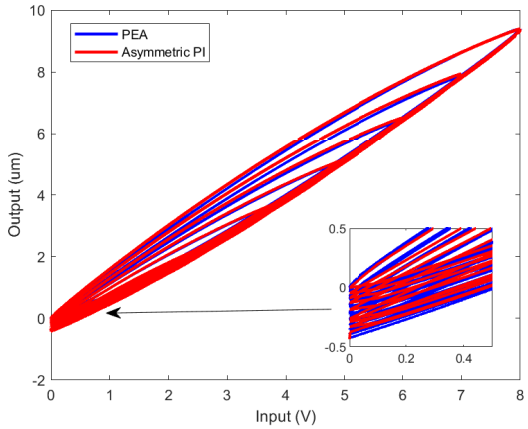

Figure 5.10: Modeling results of asymmetric hysteresis over a range of minor loops

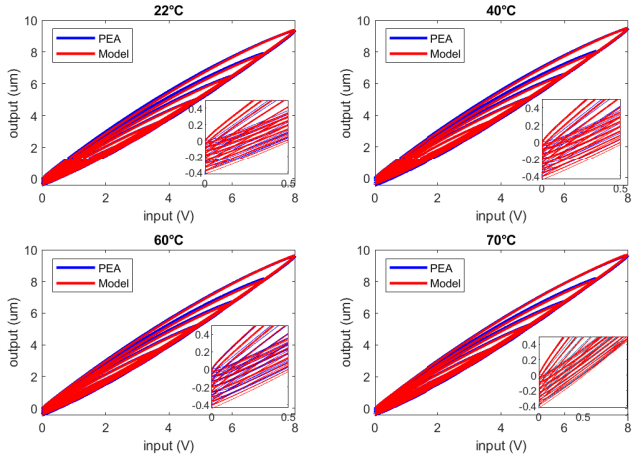

Figure 5.11: Temperature dependent hysteresis curves compared to their fitted TAPI model

along the output curve. It is shown that peak displacement for the entire input range is close to the measured value at all temperatures.

Using the inverse model described by Eqs. (5.17)-(5.18), a compensator is designed and tested at different temperatures. Fig. 5.13 shows the results of the PEA output after the compensator is applied to the input. It is seen that the compensator effectively linearlizes the output of the PEA at all temperature values. The compensation is effective also on major and minor loops. The widening of the curve near zero indicates that some modeling

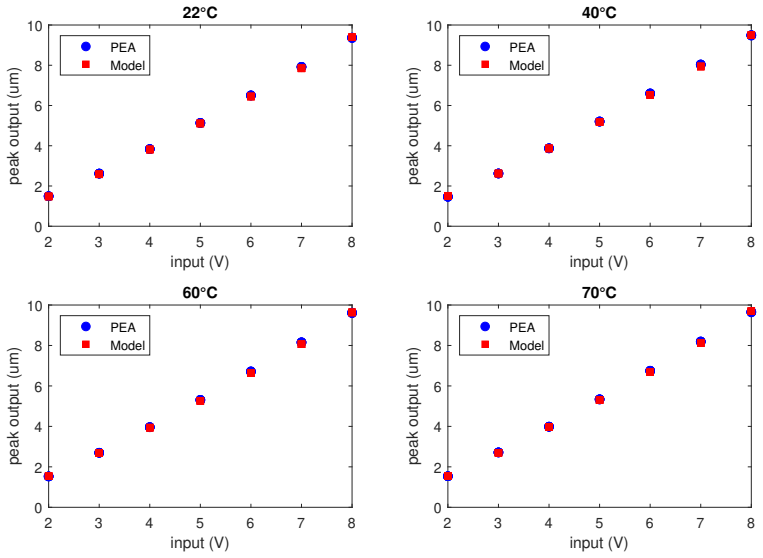

Figure 5.12: Modeling of temperature dependent displacement changes

errors are present in the initial conditions of the model, which are assumed to not depend on temperature in this study. Future studies based on the TAPI model should consider temperature dependence on the initial conditions of the OSP operators since they represent remnant displacements that are assumed to also vary with temperature and the results of the compensation confirm these findings as it is observed that the compensated output widens slightly at the bottom due to some steady state errors from incorrect remnant displacements.

To study the effectiveness of the TAPI model, the model error is shown in Fig. 5.14. It can be seen that the model error in the TAPI model stays below 0.2 um which represents about 2% error over the full range. Fig. 5.15 shows the modeling error of the TAPI model with no assumed temperature dependence. the TAPI model for $T = 22°C$ is utilized as a model for all temperature experiments. The results show a noticeable increase in modeling error compared to the results shown in Fig. 5.14. The TAPI model is shown to keep errors at similar levels throughout the temperature range whereas an increase in 18°C in an asymmetric PI model that does not take into account temperature effects exceeds the error levels observed in the

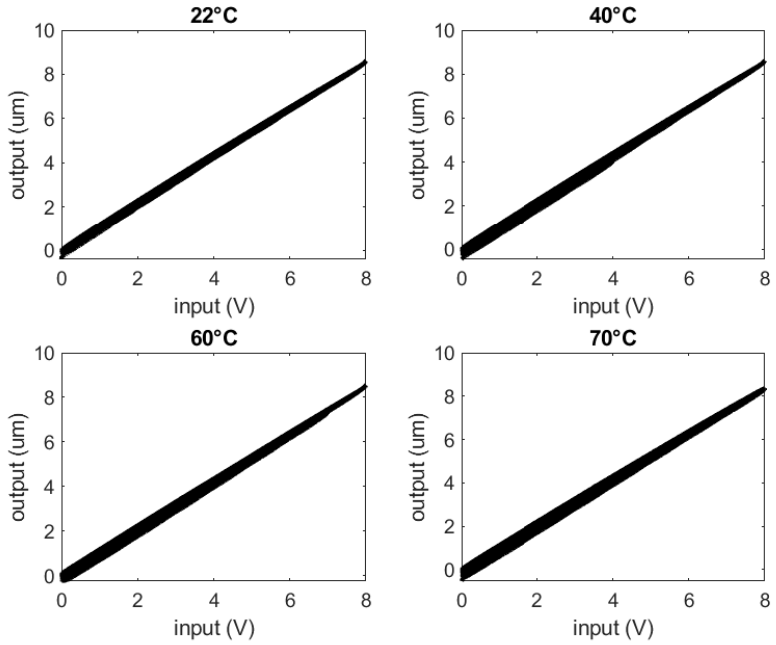

Figure 5.13: Results of the temperature extended compensator applied to the PEA system

TAPI model within the range of 22°C to 70°C. In fact, up to 0.4 um of error can be observed at 70°C if temperature is not accounted for in the model which is about double the error of the temperature dependent model.

5.3 Temperature-Dependent Coupled Hysteresis Compensation for a Fabry-Perot Interferometer

A Fabry-Perot interferometer (FPI) is an optical resonator consisting of a cavity generated by two parallel reflecting plates, often called an etalon. Within the FPI, light can reflect between the two plates multiple times, and each reflection imparts a phase change to the reflecting ray that can interfere with other rays. At certain light frequencies, the light can interfere constructively amplifying these wavelengths compared to others. This represents a resonance within the cavity at certain wavelengths that can be used as a fine pass-band filter

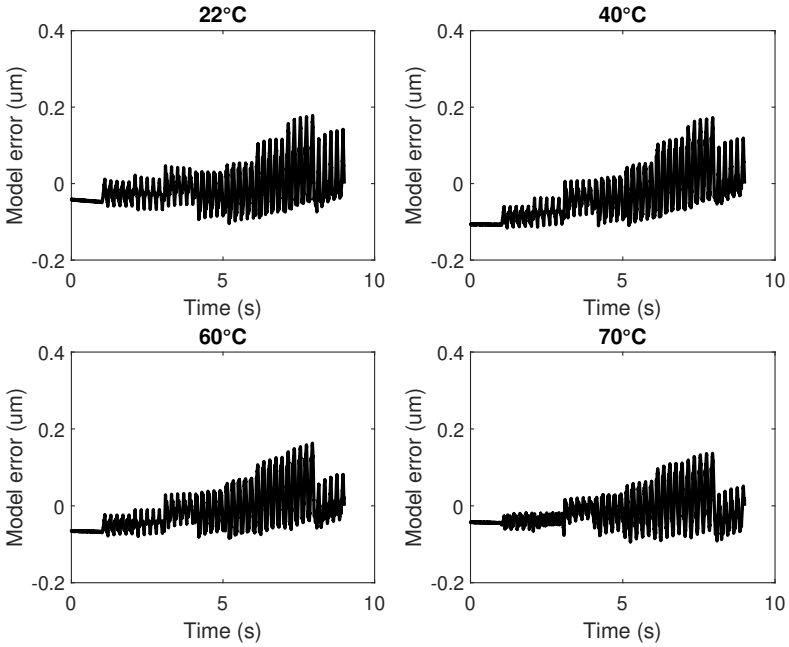

Figure 5.14: Model error of the TAPI model at different temperatures

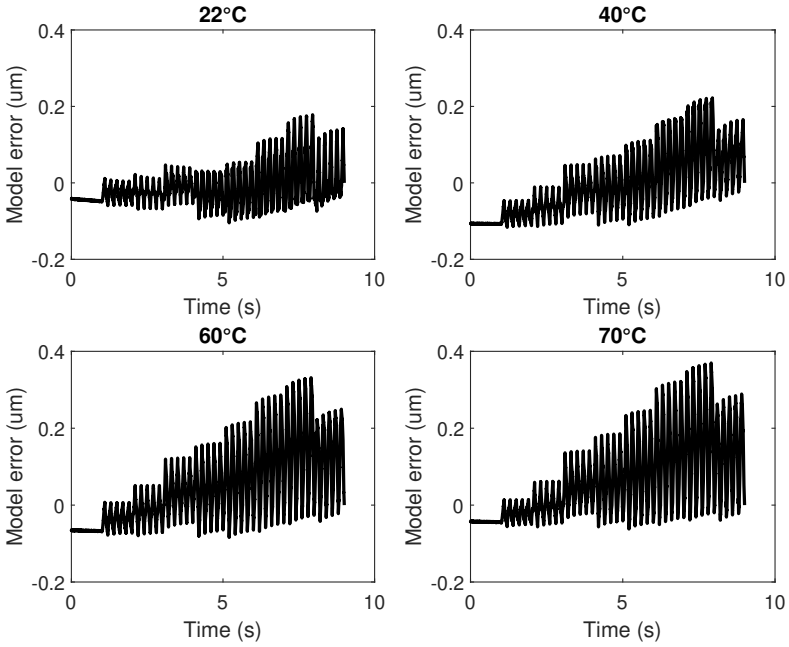

Figure 5.15: Model error of the TAPI model assuming no temperature dependence

at these resonant frequencies. The resonant wavelength can be tuned by varying the distance between the plates, which allows for applications within spectroscopy.

The quality of the FPI system is determined by its finesse, which is a measure of the free spectral range of the system relative to the width of the pass band. Due to the dependence of the width of the passband, it is clear that the parallelism of the plates is very important to ensure high-quality system performance. Any deviations in the parallelism of the plates will create a cavity with locations representing different distances, and hence different phase differences. The peak intensity of the resonant wavelengths will thus be diminished and wider.

Ensuring optimal quality of an FPI system clearly requires precise control of the parallelism of the plates, which is made more complicated in spectroscopy applications in which the cavity length is normally changed. To correct for this effect, a system of PEAs can be used to position a mirror of the FPI while together compensating for any misalignment effects. This system was designed and realised at SDCNLab in partnership with MPB Communications Inc. for stratospheric spectroscopy measurements. However, nonlinear PEA effects will continue to deteriorate the performances of such a system if they are not taken into account. In particular, during stratospheric tests, the temperature of the atmosphere can have an effect on the test results, and thermal compensation is needed. As shown in Section 5.2, the effects of temperature also affect the non-linear modelling of PEA systems. In this section, the TAPI model is adapted to the 3-axis FPI system, and a coupled TAPI model and compensator are designed and tested for the use of this FPI system.

5.3.1 Experimental System

The FPI is driven by three P-887.51 PEAs from Physik Instrumente and displacement is measured by a capacitive sensor D-015.00 from Physik Instrumente, one for each respective

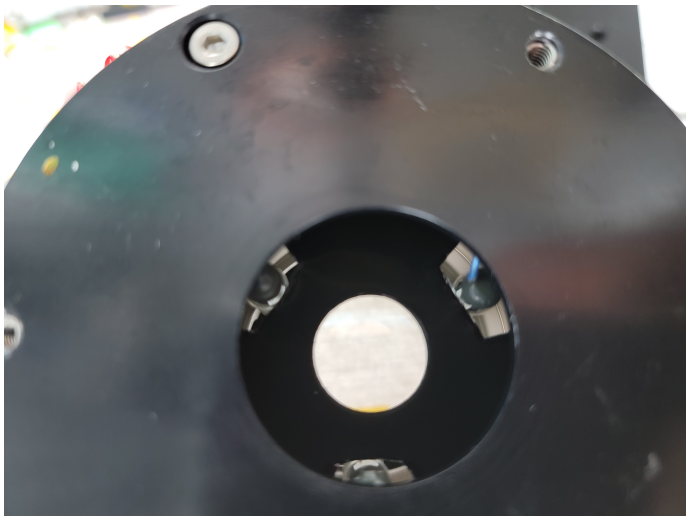

Figure 5.16: Inner optics of the FPI showing PEA placements

PEA. Three E-503 piezo amplifiers are used to supply voltage to each individual PEA and are commanded by RS-232 connections to a PC-104 computer. Real-time commands are sent using RTAI at a 50 Hz sampling rate. Fig. 5.16 shows the inside of the FPI which is composed of two parallel quartz plates that are controlled by three PEAs on the contours. The outer enclosure of the FPI is shown in Fig. 5.17 showing Minco polyimide thermofoil heaters which are used to control the temperature of the enclosure. The enclosure is further insulated using a mylar tent to prevent heat from escaping into the environment in an effort to control the temperature of the system as well as possible.

The position of the PEA with respect to the sensor is not collocated. Fig. 5.18 shows the positions of actuators A_i and sensors S_i relative to the centre of the device. Movement of an actuator serves to tilt the plate, causing displacements between the three sensors. Due to the geometry of the actuator and sensor placements, activating one actuator to tilt the plate creates an equal displacement on the other actuators and sensors relative to the origin. Using this property, the following collocation correction can be written on the PEA positions

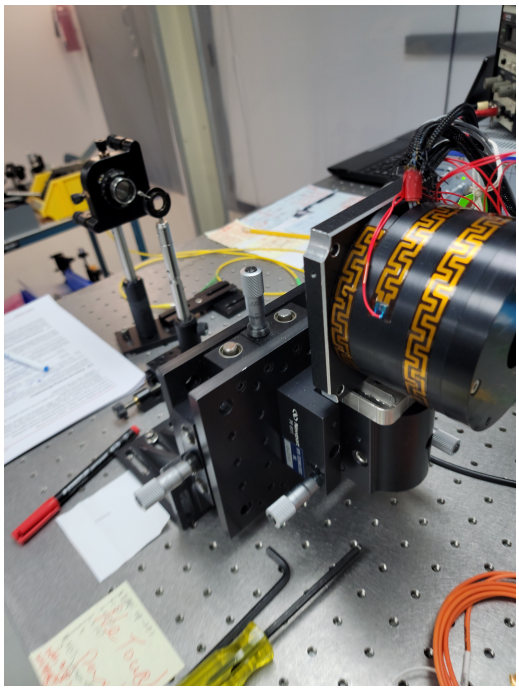

Figure 5.17: Outer enclosure of the FPI

y_i for each of the actuators.

$$y_1 = S_1 + \frac{2}{3}(\frac{S_3 + S_2}{2} - S_1)\frac{r_1 + r_2}{r_1} \tag{5.23}$$

$$y_2 = S_2 + \frac{2}{3}(\frac{S_3 + S_1}{2} - S_2)\frac{r_1 + r_2}{r_1} \tag{5.24}$$

$$y_3 = S_3 + \frac{2}{3}(\frac{S_1 + S_2}{2} - S_1)\frac{r_1 + r_2}{r_1} \tag{5.25}$$

Using Eqs. (5.23 - 5.25), the output displacements of the three actuators can be determined. An open-loop input-output response can be plotted for the position of each actuator after driving a single actuator with an input voltage. The corresponding behaviour can be seen in Fig. 5.19. In this figure, each column represents the output of PEAs 1-3 and each row corresponds to a sinusoidal driving signal of frequency 1 Hz. This frequency was chosen due

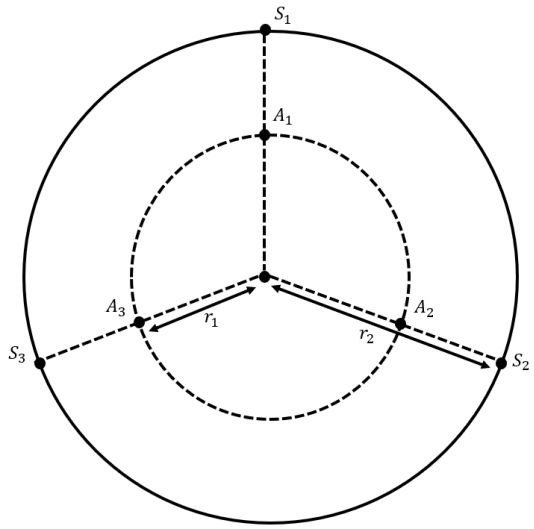

Figure 5.18: FPI plate diagram showing sensor and actuator positions

to the small sampling rate restrictions on the system. If the frequency is chosen too high, there will be fewer data points for modelling. In the figure, it can be seen that the diagonal elements show strong hysteresis behaviour, which is typical of PEA systems, whereas the off-diagonal elements also show some nonzero response representing mechanical coupling effects. It can also be seen from all diagrams that these effects are not necessarily the same. For example, hysteresis loops in the top left corner compared to the ones in the bottom right corner do not reach the same magnitude. The coupling effects are also different. This system then represents nine different hysteresis curves that must be characterised and compensated for. Additionally, the input-output behaviour should be decoupled for better system control.

The PEAs that drive the FPI mirror are temperature-dependent, and the hysteresis behaviour changes based on their temperature. To characterise this effect, the input-output behaviour of FPI is studied at a room temperature of 23°C, 30°C, and 35°C. The open-loop response at 30°C and 35°C is shown in Figs. 5.20 and 5.21, respectively.

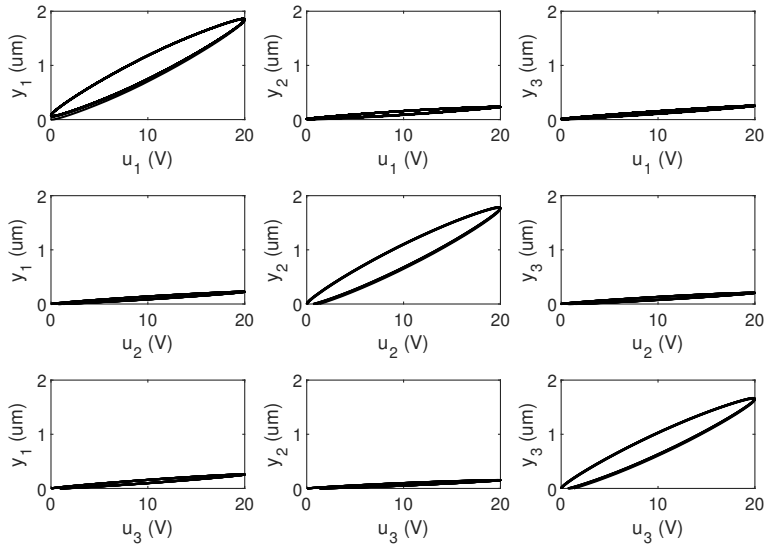

Figure 5.19: Open loop response of the FPI system at 23°C

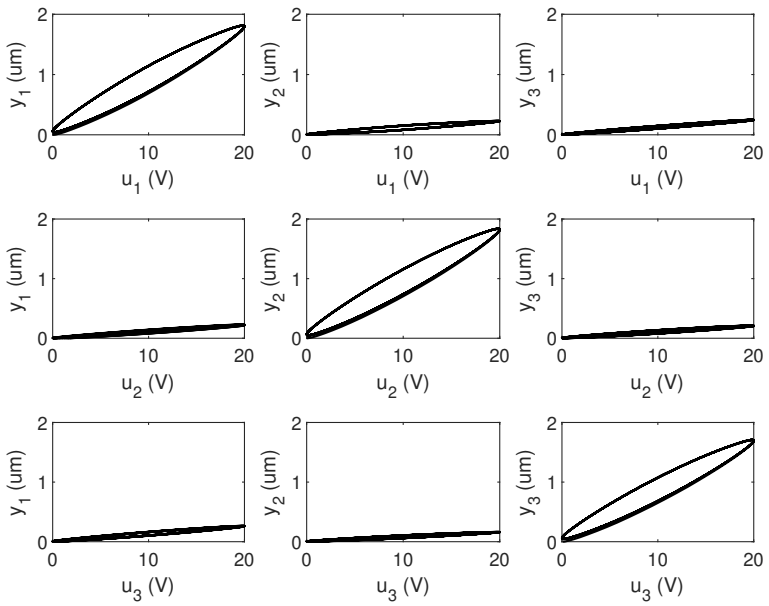

Figure 5.20: Open loop response of the FPI system at 30°C

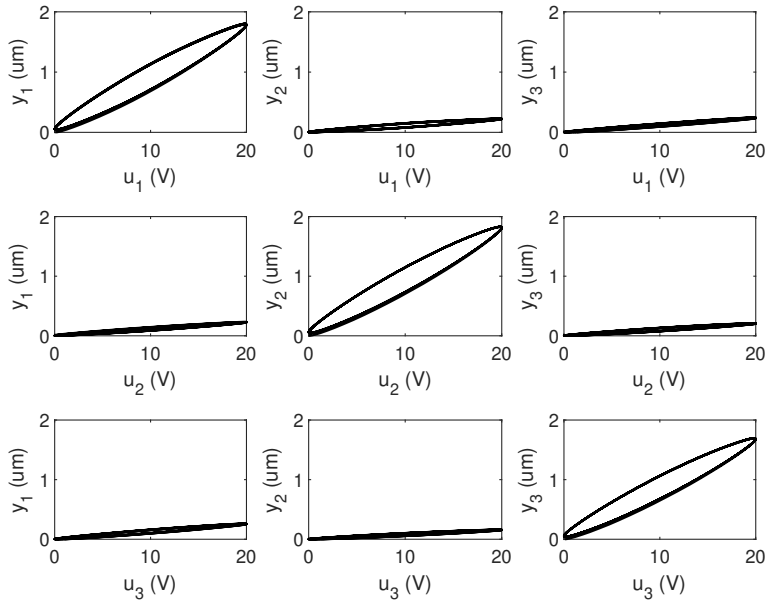

Figure 5.21: Open loop response of the FPI system at 35°C

5.3.2 Coupled TAPI Model

Let the output vector $\boldsymbol{y} = [y_1, y_2, y_3]^T$ represent the displacement of PEAs 1-3 and let the input vector $\boldsymbol{u} = [u_1, u_2, u_3]$ denote the inputs in their respective PEA. Each pair $u_i - y_j$ can be associated with a TAPI model as follows.

$$y_j(u_i, T) = P_s^{ij}(1 - \frac{T}{T_C})^{\beta_{ij}} \tanh(\frac{u_i}{a_{ij}T}) + \sum_{k=1}^{n} c_k^{ij} F_{r_k}[u_i](t) \tag{5.26}$$

In Eq. (5.26), all classical PI coefficients c_k^{ij}, as well as the coefficients of the TAPI model P_s^{ij}, a_{ij}, and β_{ij} are required to be found for the nine components of the coupled model, while T_c and r_k are assumed to be common for all models. This is reasonable because all actuators are made of the same material and should have Curie temperatures around the same value, while thresholds r_k are chosen before modelling. In principle, r_k does not need to be common between the models, but they are kept the same for simplicity. The observed

output displacement for a given PEA is then the sum of three TAPI models.

$$y_j(\boldsymbol{u}, T) = y_j(u_1, T) + y_j(u_2, T) + y_j(u_3, T) \tag{5.27}$$

Eq. 5.27 shows the expected response of PEA j as a function of all inputs and is made up of three classical PI models for each given input signal and three different hysteresis-free nonlinear components as a result of domain reorientation in piezoelectric materials. A coupled TAPI compensator can be designed as follows.

$$u_i = P_{ii}^{-1}(w_i) \tag{5.28}$$

Where P_{ii}^{-1} denotes the inverse classical PI model detailed in Section 2.1.1 for the diagonal components and w_i is the input to this model which includes the components of the TAPI model as well as the coupling components. The shape of w_i is given as follows.

$$w_1 = y_{1d} - y_1(u_2, T) - y_1(u_3, T) - P_s^{11}(1 - \frac{T}{T_C})^{\beta_{11}} \tanh(\frac{u_1}{a_{11}T}) \tag{5.29}$$

$$w_2 = y_{2d} - y_2(u_1, T) - y_2(u_3, T) - P_s^{22}(1 - \frac{T}{T_C})^{\beta_{22}} \tanh(\frac{u_2}{a_{22}T}) \tag{5.30}$$

$$w_3 = y_{3d} - y_3(u_1, T) - y_3(u_2, T) - P_s^{33}(1 - \frac{T}{T_C})^{\beta_{33}} \tanh(\frac{u_3}{a_{33}T}) \tag{5.31}$$

where y_{id} is the desired output in PEA i and $y_i(u_j, T)$ are the predicted outputs based on modelled TAPI models. Thus, Eqs. (5.28 - 5.31) form a decoupled compensator for the coupled TAPI model. Each compensator is made up of an inverse TAPI model and two TAPI models that describe the coupling effects of other inputs.

5.3.3 Coupled TAPI Compensation Results

The behavior of the coupled TAPI compensator must be tested in practise to linearise both the outputs of the three PEAs and also to decouple the outputs of the system by zeroing the off-diagonal elements in the $u_i - y_j$ domain. A 9-parameter PI model is used to approximate the 9 hysteresis curves at temperatures 23°C, 30°C, and 35°C. The limited sampling rate also limited the possibility of a greater number of parameters in the PI model. Once the classical PI model is fitted, the temperature dependence is added by finding parameters P_s^{ij}, a_{ij}, and β_{ij} to introduce the temperature dependence of the TAPI model. Figs. 5.22 - 5.24 show the decoupled TAPI compensator response over the tested temperature range. Comparison with Figs. 5.19 - 5.21 illustrates that, in all cases, the diagonal is linearised, while the off diagonal shows decent decoupling performance with the output nearer to zero than before compensation. However, it can be seen that some coupling remains, since the slopes of the lines are not perfectly zero.

To better compare the compensator results, the modelling error $y - y_d$ is plotted in Figs. 5.25 - 5.27. It can be seen that the error is confined to under 0.2 um in all cases. It can be seen, however, that larger errors exist at the extremities of the output. This behaviour is due to modelling inaccuracies due to smaller slopes with a small number of data points due to sampling rate. At small slope values, modelling inaccuracies are magnified, creating this effect at extremities. Improvements can be made if a larger sampling time is used, allowing more coefficients and more data points for coefficient determination. From the collected data, it can be seen that the decoupled TAPI compensator improves the input-output behaviour of the FPI system studied.

In this chapter, a temperature-dependent asymmetric PI model is developed based on ferroelectric principles. The model only affects a hysteresis-free region of the electromechanical PEA model making the implementation simple. The model is further applied to a FPI system

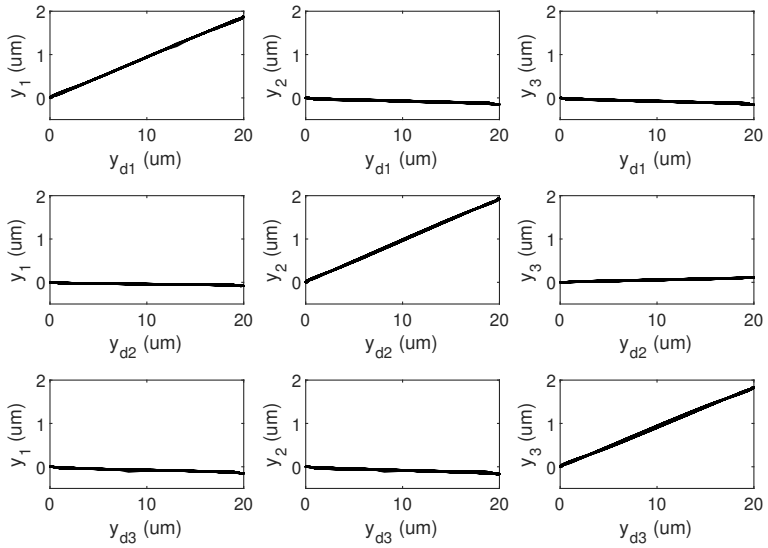

Figure 5.22: FPI response using the coupled TAPI compensator at 23°C

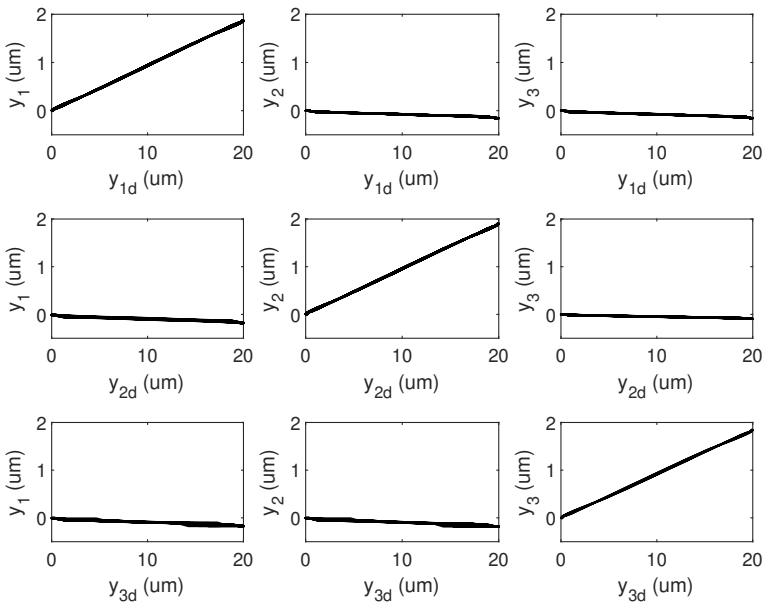

Figure 5.23: FPI response using the coupled TAPI compensator at 30°C

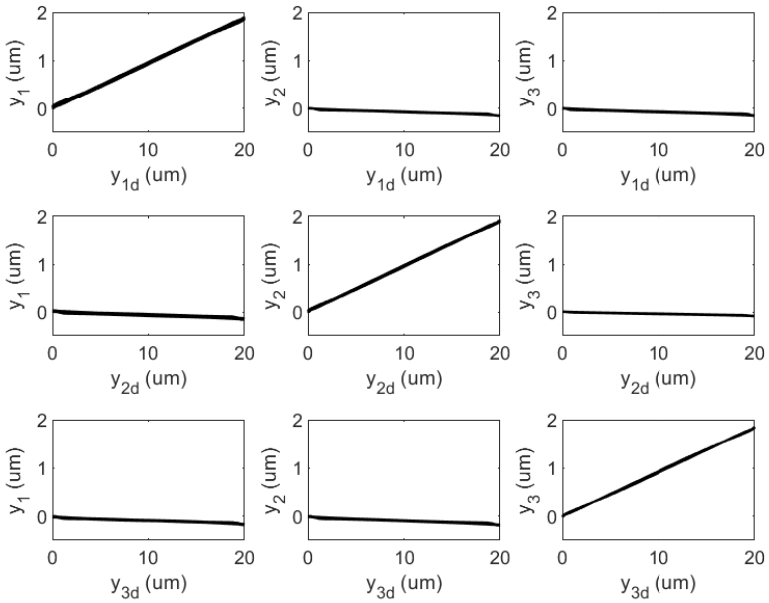

Figure 5.24: FPI response using the coupled TAPI compensator at 35°C

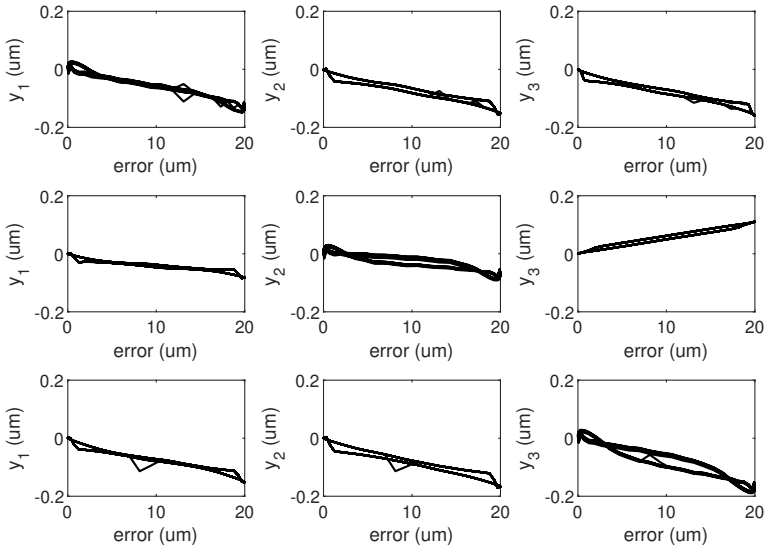

Figure 5.25: FPI tracking error using the coupled TAPI compensator at 23°C

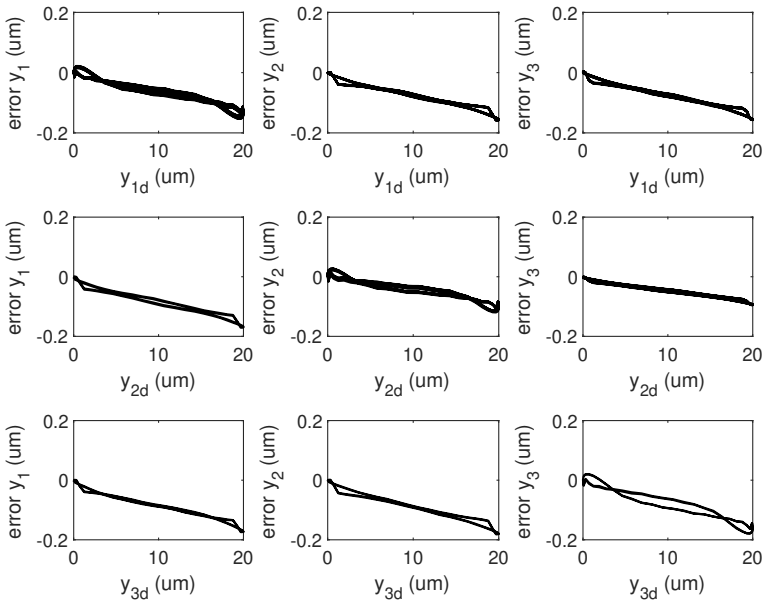

Figure 5.26: FPI tracking error using the coupled TAPI compensator at 30°C

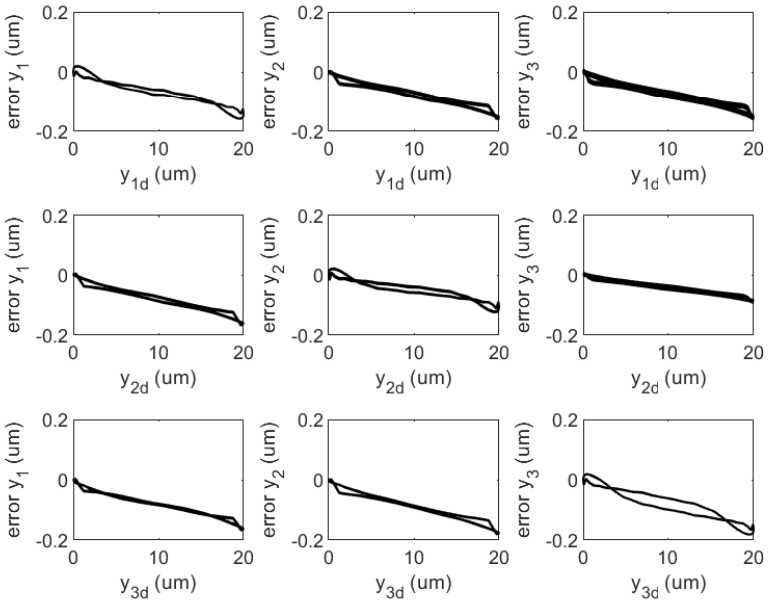

Figure 5.27: FPI tracking error using the coupled TAPI compensator at 35°C

with three coupled PEAs. A decoupled TAPI model is developed to linearize this system.

Chapter 6

Conclusion

The overarching theme of this dissertation has been the idea that the hysteresis present in PEAs at its core is a physical phenomenon created by the fact that most PEAs are created using ferroelectric materials. From the processes that dictate the behaviour of these classes of materials, inspiration can be utilised to explore more detailed nuances of the usual modelling of hysteresis in PEAs. The modelling of piezoelectric hysteresis was investigated for use in piezoelectric actuator systems. The Prandtl-Ishlinskii, Bouc-Wen, and Jiles-Atherton models were investigated and compared in their performances as open-loop compensation methods for the PEAs. It was found that all approaches could compensate for hysteresis effectively, but the differential equation-based models had generally better accuracies than the the PI model while also adding less modelling noise into the system due to their smoother curves. However, the PI model has appealing properties in its own right, such as adaptability, ease of parameter identification, and an inverse structure that is itself a PI model with new inverse parameters. When models are compared in a closed-loop proportional-integral controller with a feedforward hysteresis compensation term, all compensators were found to reduce control error compared to an uncompensated proportional-integral controller with the same parameters. Two controllers were designed with different bandwidth and robustness. For a

higher bandwidth controller, the compensators reduced the overall error by about half of what was seen in the uncompensated controller, though some added noise featured prominently in the PI model compared to the JA and BW model. This higher-bandwidth controller was designed at the expense of robustness, as indicated by its lower phase and gain margins. A slower but more robust controller was also evaluated. This controller showed much greater improvement when used in conjunction with an inverse hysteresis model, with these models improving the error by an order of magnitude over the uncompensated case. The results suggest that hysteresis modelling can improve the robustness of simple proportional integral control schemes by reducing the burden of hysteresis as a disturbance in these systems, making lower bandwidth controllers more viable. At higher bandwidths, while control performance is still increased with modelling, it should be noted that modelling errors can inject errors into the system that could lower the robustness of these controllers, which are already less robust than controllers designed with a lower bandwidth. These issues should be taken into account to ensure the proper stability of the system.

This work also explores the hysteresis generated in the electrical domain of the PEA in its polarisation state. It is known that the hysteresis between charge and displacement in PEA systems is much reduced compared to the hysteresis between voltage and displacement. However, it was noted that the hysteresis in many PEAs using ferroelectric materials comes from the dynamics between their polarisation state and the electric field applied to the system. Tracking this polarisation state had never been attempted; therefore, an experimental procedure was designed to investigate this parameter and model it based on the physics-based JA hysteresis model, which is assumed to describe these polarisation dynamics. The system is based on tracking the impedance of the system using a low-amplitude, high-frequency sensing signal that is overlaid on a lower frequency but higher-amplitude driving signal. From the measured impedance of the ripple signal, a polarisation value was extracted considering the imaginary part of the impedance as belonging to a capacitance. This is a valid model, since

PEAs are mainly capacitive loads, and a stack actuator can be modelled as a certain number of capacitors plugged in parallel. Using this method, it was possible to model hysteresis between the polarisation state of the actuator and the voltage while creating a compensated signal that allowed the polarisation state to track a desired output. The modelled polarisation was shown to reduce hysteresis between voltage and displacement, though some hysteresis remained.

Another topic that was investigated in this dissertation was the parameter estimation of certain hysteresis models. It has often been stated in the literature that proper parameter estimation for differential equation-based models limits their application in practise, whereas the effect of parameters on the general characteristics of the hysteresis curve is not as well understood compared to operator-based models where coefficients typically have some geometric meaning. A Monte Carlo simulation study was performed on the JA model to help understand the impact some of the parameters in this model have on the area of the hysteresis curves and the remnant displacement. However, since modelled hysteresis curves can have wildly different lengths, a normalised JA model was developed and the inverse normalised JA model was described. This normalisation procedure increases the number of potential compatible solutions that can accurately describe PEA hysteresis, since it no longer screens out solutions that would be out of range. Using this developed normalised JA model, Monte Carlo simulations are performed to assess a large number of normalised hysteresis curves across the parameter space. These models are evaluated for their remnant displacement and hysteresis areas. This large number of characterised hysteresis curves, solutions that have areas, and remnant displacements that are close to those found in the PEA system are investigated. It was found that when the data were selected in the characteristic range of PEA hysteresis, regions with a high density of potential solutions were found in both cases for two specific parameters in the JA model, namely the parameters c and k. These data were used to modify the PSO algorithm, which had been used successfully in the past to find

the JA hysteresis parameters. Two modifications are made to the PSO algorithm. The first is to assess only the normalised JA model in an otherwise unmodified PSO algorithm. The second modification is to use the normalised JA model along with a modified velocity term in the PSO algorithm that initially attracts particles to random locations that were found to have a higher density of potential solutions from the Monte Carlo simulations. The results showed that normalising the JA model prior to parameter identification greatly improved the convergence of the PSO algorithm after 100 iterations. Furthermore, data-driven velocity modification was able to speed up the initial convergence of the PSO algorithm and a more optimal solution was found.

In this work, the estimation of parameters of the PI model was also investigated. Although parameters in the classical PI model can be found geometrically, in situations where the hysteresis curve changes frequently, a very frequent recalculation of sometimes a large number of parameters would be required. A scaling procedure is investigated on the basis of some properties of the PI model. In this procedure, the area of a PI curve is calculated simply based on its parameters, and a modification procedure is described based on adding or subtracting from the hysteresis free parameter some value and rescaling all parameters such that the length of the generated hysteresis curve returns to its original value. Using this three-step procedure, hysteresis curves can be analytically scaled in area to reflect measured data. This procedure was used to describe changes in the hysteresis area that were observed when the PEA was driven at higher amplitudes. Although the rescaling process was unable to accurately account for changes in the overall shape of the PEA hysteresis, controlling the area of the hysteresis curve through the rescaling process diminished the modelling errors over a range of frequencies without needing to recalculate all parameters.

Finally, this work considers the effect of temperature on the hysteresis modelling for PEAs. This particular topic has been largely ignored in the literature, despite observations in ferroelectric materials that the hysteresis changes in response to temperature changes. The

approach to temperature modelling utilised in this work is to provide a physical interpretation of the PI model parameters to then introduce temperature effects into the proper parameters based on understanding the origins of the hysteresis nonlinearity. Using an electromechanical model, the hysteresis-free term in the PI model can be modelled as an ideal capacitor. In practise, the PEA is not an ideal capacitor, as its polarisation does not behave linearly. To account for this, the anhysteretic term borrowed from the domain wall description of the polarisation is incorporated into the hysteresis-free coefficient of this model which created a PI model with a generalised odd function as a hysteresis free term rather than a linear hysteresis-free component. A temperature extension to the saturation polarisation is added to further extend the model to a temperature-dependent model, and the model is dubbed the TAPI model. The TAPI model is temperature dependent and asymmetric has a very appealing description because asymmetric and temperature dependence is entirely described in one term of the model, while the classical PI model remains part of the description. Identification procedures are developed on the basis of the strengths of the classical PI model, making the TAPI model parameter identification simple. An inverse TAPI model is described and formulated iteratively. The results of the TAPI model show that it describes the temperature dependence in the hysteresis well and that a feedforward compensator based on the TAPI model is designed. It was found that the TAPI model successfully linearised the hysteresis of the PEA system. The TAPI model was also tested on an FPI system composed of three actuators that move a mirror to change the gap spacing of the optical cavity. A decoupled TAPI compensator was designed to linearise the outputs while also decoupling the mechanical influences each PEA had on each other. The TAPI model was able to show good performance in this task across the temperature range that was studied, further improving the behaviour of a system that is sensitive to temperature changes.

6.1 Future Work

Several research directions can be explored on the basis of the elements described in this dissertation. First, investigations into the state of polarisation in the PEA systems were limited by the equipment used. The ripple signals generated to sense the polarisation state had to be done at a relatively low frequency, limiting studies to very low-frequency driving signals. Additionally, for more accurate polarisation determinations, conditions after a single oscillation should be approximately quasistatic. Ideally, these ripple signals should be higher than the first resonant mode of the PEA so that the PEA displacement is not greatly affected by these measurements. Under these conditions, a much more accurate determination of the polarisation can be achieved to better study their effects.

In parameter estimation, a lot of research has been conducted in this field in a variety of different models. However, methods to more quickly and reliably converge solutions to an acceptable degree are still of great interest. In this work, a Monte Carlo simulation over the parameter space of the JA model helped pinpoint locations of solution candidates that agree with the PEA system. If a more detailed analysis of the effect of model parameters for differential equation-based models was provided such that hysteresis curves could be tuned without heavily relying on optimisation algorithms, it would help eliminate one of their biggest drawbacks. For the PI coefficient rescaling procedure described in this work, future research that would greatly benefit this method would be to extend it to more complicated PI models. In this work, scaling on the classic PI model was done, but it is not guaranteed to work for PI models based on different operators or asymmetric PI models. Such a procedure would greatly benefit these more complex models, since they often require more parameter optimisation rather than simple coefficient recalculation.

Finally, temperature-dependent modelling of PEAs is slowly gaining more attention in the literature, and there is a lot of space left to explore. In this work, a temperature-extended

asymmetric PI model is proposed to describe changes in PEA hysteresis. However, it was found that the initial conditions of the OSP operators should also be temperature dependent to properly describe the changes found in remnant displacement. Furthermore, other non-linearities, such as creep, should be investigated for their temperature-dependent behaviour. Control strategies in variable temperature environments can be explored for a more general applicability of PEAs. Lastly, other environmental effects of PEAs could be investigated, such as environmental pressure, which would also be useful for study for use in the FPI system, which runs experiments in the stratosphere with different atmospheric conditions.

Appendix A

Publication List

1. Savoie, Marc, and Shan, Jinjun. "Modelling and Compensation of Hysteresis in Polarization of Piezoelectric Actuators." 2018 AIAA/AHS Adaptive Structures Conference. 2018.

2. Savoie, Marc, and Shan, Jinjun. "Temperature-dependent Asymmetric Prandtl-Ishlinskii Hysteresis Model for Piezoelectric Actuators" Smart Materials and Structures. 2022

3. Savoie, Marc, and Shan, Jinjun. "Monte Carlo Study of Jiles-Atherton Parameters on Hysteresis Area and Remnant Displacement." 2022 IEEE 31st International Symposium on Industrial Electronics (ISIE). IEEE, 2022.

Bibliography

[1] Wikipedia contributors, "Lead zirconate titanate in Wikipedia, The Free Encyclopedia," 2022, [Online; accessed 10-April-2022]. [Online]. Available: https://en.wikipedia.org/wiki/Leadzirconatetitanate

[2] C. D. Near, "Piezoelectric actuator technology," in *Smart Structures and Materials 1996: Smart Structures and Integrated Systems*, I. Chopra, Ed., vol. 2717, International Society for Optics and Photonics. SPIE, 1996, pp. 246 – 258. [Online]. Available: https://doi.org/10.1117/12.239027

[3] C. Y. K. Chee, L. Tong, and G. P. Steven, "A review on the modelling of piezoelectric sensors and actuators incorporated in intelligent structures," *Journal of Intelligent Material Systems and Structures*, vol. 9, no. 1, pp. 3–19, 1998.

[4] M. Hara, Y. Yano, M. Kajita, H. Nishino, Y. Ibata, M. Toda, S. Hara, A. Kasamatsu, H. Ito, T. Ono, and T. Ido, "Microwave oscillator using piezoelectric thin-film resonator aiming for ultraminiaturization of atomic clock," *Review of Scientific Instruments*, vol. 89, no. 10, p. 105002, 2018.

[5] K. Spanner and B. Koc, "Piezoelectric motors, an overview," *Actuators*, vol. 5, no. 1, 2016.

[6] J. P. Domann and G. P. Carman, "Strain powered antennas," *Journal of Applied Physics*, vol. 121, no. 4, p. 044905, 2017.

[7] S. Saadon and O. Sidek, "A review of vibration-based mems piezoelectric energy harvesters," *Energy Conversion and Management*, vol. 52, no. 1, pp. 500–504, 2011.

[8] D. Sabarianand, P. Karthikeyan, and T. Muthuramalingam, "A review on control strategies for compensation of hysteresis and creep on piezoelectric actuators based micro systems," *Mechanical Systems and Signal Processing*, vol. 140, p. 106634, 2020.

[9] H. Habibullah, "30 years of atomic force microscopy: Creep, hysteresis, cross-coupling, and vibration problems of piezoelectric tube scanners," *Measurement*, vol. 159, p. 107776, 2020.

[10] W. Zhu and X.-T. Rui, "Hysteresis modeling and displacement control of piezoelectric actuators with the frequency-dependent behavior using a generalized bouc–wen model," *Precision Engineering*, vol. 43, pp. 299–307, 2016. [Online]. Available: https://www.sciencedirect.com/science/article/pii/S0141635915001555

[11] J. Deng, Y. Liu, S. Zhang, and J. Li, "Development of a nanopositioning platform with large travel range based on bionic quadruped piezoelectric actuator," *IEEE/ASME Transactions on Mechatronics*, vol. 26, no. 4, pp. 2059–2070, 2021.

[12] J. J. Dosch, D. J. Inman, and E. Garcia, "A self-sensing piezoelectric actuator for collocated control," *Journal of Intelligent Material Systems and Structures*, vol. 3, no. 1, pp. 166–185, 1992.

[13] S. Y. Wang, S. T. Quek, and K. K. Ang, "Vibration control of smart piezoelectric composite plates," *Smart Materials and Structures*, vol. 10, no. 4, pp. 637–644, jul 2001.

[14] K. Iwata, S. Yamazaki, P. Mutombo, P. Hapala, M. Ondráček, P. Jelínek, and Y. Sugimoto, "Chemical structure imaging of a single molecule by atomic force microscopy at room temperature," *Nature Communications*, vol. 6, no. 1, p. 7766, Jul 2015.

[15] H. Labidi, M. Koleini, T. Huff, M. Salomons, M. Cloutier, J. Pitters, and R. A. Wolkow, "Indications of chemical bond contrast in afm images of a hydrogen-terminated silicon surface," *Nature communications*, vol. 8, no. 1, pp. 1–7, 2017.

[16] G. R. Heath and S. Scheuring, "Advances in high-speed atomic force microscopy (hs-afm) reveal dynamics of transmembrane channels and transporters," *Current Opinion in Structural Biology*, vol. 57, pp. 93–102, 2019, membranes Engineering Design: Synthetic Signalling. [Online]. Available: https://www.sciencedirect.com/science/article/pii/S0959440X19300120

[17] Z. Li, J. Shan, and U. Gabbert, "Dynamics modeling and inversion-based synchronized model predictive control for a fabry–perot spectrometer," *IEEE/ASME Transactions on Mechatronics*, vol. 24, no. 4, pp. 1818–1828, 2019.

[18] "Ieee standard on piezoelectricity," *ANSI/IEEE Std 176-1987*, 1988.

[19] J. Yang, *An introduction to the theory of piezoelectricity*. Springer, 2005, vol. 9.

[20] D. C. Jiles and D. L. Atherton, "Theory of ferromagnetic hysteresis (invited)," *Journal of Applied Physics*, vol. 55, no. 6, pp. 2115–2120, 1984.

[21] C. M. Landis, "Non-linear constitutive modeling of ferroelectrics," *Current Opinion in Solid State and Materials Science*, vol. 8, no. 1, pp. 59–69, 2004.

[22] K. Bhattacharya and G. Ravichandran, "Ferroelectric perovskites for electromechanical actuation," *Acta Materialia*, vol. 51, no. 19, pp. 5941–5960, 2003, the Golden Jubilee Issue. Selected topics in Materials Science and Engineering: Past, Present and Future.

[23] C. Jullian, J. F. Li, and D. Viehland, "Comparisons of polarization switching in "hard," "soft," and relaxor ferroelectrics," *Journal of Applied Physics*, vol. 95, no. 8, pp. 4316–4318, 2004.

[24] P. Muralt, N. Ledermann, J. Paborowski, A. Barzegar, S. Gentil, B. Belgacem, S. Petitgrand, A. Bosseboeuf, and N. Setter, "Piezoelectric micromachined ultrasonic transducers based on pzt thin films," *IEEE Transactions on Ultrasonics, Ferroelectrics, and Frequency Control*, vol. 52, no. 12, pp. 2276–2288, 2005.

[25] Y. Shapiro, G. Kósa, and A. Wolf, "Shape tracking of planar hyper-flexible beams via embedded pvdf deflection sensors," *IEEE/ASME Transactions on Mechatronics*, vol. 19, no. 4, pp. 1260–1267, 2014.

[26] T. D. Usher, K. R. Cousins, R. Zhang, and S. Ducharme, "The promise of piezoelectric polymers," *Polymer International*, vol. 67, no. 7, pp. 790–798, 2018.

[27] D. A. Hall, "Review nonlinearity in piezoelectric ceramics," *Journal of Materials Science*, vol. 36, no. 19, pp. 4575–4601, Oct 2001.

[28] V. D. Kugel and L. E. Cross, "Behavior of soft piezoelectric ceramics under high sinusoidal electric fields," *Journal of Applied Physics*, vol. 84, no. 5, pp. 2815–2830, 1998.

[29] L. D. Stevens, "The evolution of magnetic storage," *IBM Journal of Research and Development*, vol. 25, no. 5, pp. 663–676, 1981.

[30] J. Zhang, H. Zhang, and X. Xiao, "New identification method for backlash of gear transmission systems," in *2018 2nd IEEE Advanced Information Management,Communicates,Electronic and Automation Control Conference (IMCEC)*, 2018, pp. 378–382.

[31] K. A. Morris, "What is Hysteresis?" *Applied Mechanics Reviews*, vol. 64, no. 5, 08 2012, 050801. [Online]. Available: https://doi.org/10.1115/1.4007112

[32] Z. Li, J. Shan, and U. Gabbert, "Inverse compensation of hysteresis using krasnoselskii-pokrovskii model," *IEEE/ASME Transactions on Mechatronics*, vol. 23, no. 2, pp. 966–971, 2018.

[33] M. Ismail, F. Ikhouane, and J. Rodellar, "The hysteresis bouc-wen model, a survey," *Archives of computational methods in engineering*, vol. 16, no. 2, pp. 161–188, 2009.

[34] A. K. Padthe, B. Drincic, J. Oh, D. D. Rizos, S. D. Fassois, and D. S. Bernstein, "Duhem modeling of friction-induced hysteresis," *IEEE Control Systems Magazine*, vol. 28, no. 5, pp. 90–107, 2008.

[35] M. Al Janaideh, S. Rakheja, and C.-Y. Su, "An analytical generalized prandtl–ishlinskii model inversion for hysteresis compensation in micropositioning control," *IEEE/ASME Transactions on mechatronics*, vol. 16, no. 4, pp. 734–744, 2010.

[36] S. Bashash and N. Jalili, "A polynomial-based linear mapping strategy for feedforward compensation of hysteresis in piezoelectric actuators," *Journal of Dynamic Systems, Measurement, and Control*, vol. 130, no. 3, 2008.

[37] R. C. Smith and C. L. Hom, "Domain wall theory for ferroelectric hysteresis," *Journal of Intelligent Material Systems and Structures*, vol. 10, no. 3, pp. 195–213, 1999.

[38] Z. Li and X. Zhang, "Model order reduction for the krasnoselskii–pokrovskii (KP) model," *Smart Materials and Structures*, vol. 28, no. 9, p. 095001, jul 2019.

[39] G. Gu and L. Zhu, "High-speed tracking control of piezoelectric actuators using an ellipse-based hysteresis model," *Review of Scientific Instruments*, vol. 81, no. 8, p. 085104, 2010.

[40] J.-D. Wei and C.-T. Sun, "Large simulation of hysteresis systems using a piecewise polynomial function," *IEEE Signal Processing Letters*, vol. 9, no. 7, pp. 207–210, 2002.

[41] H. Jung and D.-G. Gweon, "Creep characteristics of piezoelectric actuators," *Review of Scientific Instruments*, vol. 71, no. 4, pp. 1896–1900, 2000.

[42] K. Kuhnen and P. Krejci, "Inverse control of systems with hysteresis and creep," *IEE proceedings. Control theory and applications*, vol. 148, no. 3, pp. 185–192, 2001.

[43] Y. Liu, J. Shan, and N. Qi, "Creep modeling and identification for piezoelectric actuators based on fractional-order system," *Mechatronics*, vol. 23, no. 7, pp. 840–847, 2013, 1. Fractional Order Modeling and Control in Mechatronics 2. Design, control, and software implementation for distributed MEMS (dMEMS).

[44] Y. Liu, J. Shan, U. Gabbert, and N. Qi, "Hysteresis and creep modeling and compensation for a piezoelectric actuator using a fractional-order maxwell resistive capacitor approach," *Smart Materials and Structures*, vol. 22, no. 11, p. 115020, 2013.

[45] M. P. Yothers, A. E. Browder, and L. A. Bumm, "Real-space post-processing correction of thermal drift and piezoelectric actuator nonlinearities in scanning tunneling microscope images," *Review of Scientific Instruments*, vol. 88, no. 1, p. 013708, 2017.

[46] H. Kungl and M. J. Hoffmann, "Temperature dependence of poling strain and strain under high electric fields in lasr-doped morphotropic pzt and its relation to changes in structural characteristics," *Acta Materialia*, vol. 55, no. 17, pp. 5780–5791, 2007.

[47] J. Chen, L. Hu, J. Deng, and X. Xing, "Negative thermal expansion in functional materials: controllable thermal expansion by chemical modifications," *Chemical Society Reviews*, vol. 44, no. 11, pp. 3522–3567, 2015.

[48] L. Juhász, J. Maas, and B. Borovac, "Parameter identification and hysteresis compensation of embedded piezoelectric stack actuators," *Mechatronics*, vol. 21, no. 1, pp. 329–338, 2011. [Online]. Available: https://www.sciencedirect.com/science/article/pii/S0957415810002175

[49] M. Rhimi and N. Lajnef, "Passive temperature compensation in piezoelectric vibrators using shape memory alloy–induced axial loading," *Journal of Intelligent Material Systems and Structures*, vol. 23, no. 15, pp. 1759–1770, 2012.

[50] V. Hassani, T. Tjahjowidodo, and T. N. Do, "A survey on hysteresis modeling, identification and control," *Mechanical systems and signal processing*, vol. 49, no. 1-2, pp. 209–233, 2014.

[51] R. Xu and M. Zhou, "Sliding mode control with sigmoid function for the motion tracking control of the piezo-actuated stages," *Electronics Letters*, vol. 53, no. 2, pp. 75–77, 2017.

[52] L. Liu, K. K. Tan, A. S. Putra, and T. H. Lee, "Compensation of hysteresis in piezoelectric actuator with iterative learning control," *Journal of Control Theory and Applications*, vol. 8, no. 2, pp. 176–180, 2010.

[53] Y. Jian, D. Huang, J. Liu, and D. Min, "High-precision tracking of piezoelectric actuator using iterative learning control and direct inverse compensation of hysteresis," *IEEE Transactions on Industrial Electronics*, vol. 66, no. 1, pp. 368–377, 2019.

[54] M. Bazghaleh, S. Grainger, and M. Mohammadzaheri, "A review of charge methods for driving piezoelectric actuators," *Journal of Intelligent Material Systems and Structures*, vol. 29, no. 10, pp. 2096–2104, 2018.

[55] K. Buschow, R. Cahn, M. Flemings, S. Mahajan, B. Ilschner, E. Kramer, and P. Veyssiere, *The Encyclopedia of Materials: Science and Technology*, ser.

Encyclopedia of Materials: Science and Technology. Elsevier, 2001. [Online]. Available: https://books.google.ca/books?id=nd-RjgEACAAJ

[56] J. Gan and X. Zhang, "A review of nonlinear hysteresis modeling and control of piezoelectric actuators," *AIP Advances*, vol. 9, no. 4, p. 040702, 2019.

[57] Q. Xu and Y. Li, "Dahl model-based hysteresis compensation and precise positioning control of an xy parallel micromanipulator with piezoelectric actuation," *Journal of dynamic systems, measurement, and control*, vol. 132, no. 4, 2010.

[58] I. Mayergoyz, "The classical preisach model of hysteresis," in *Mathematical models of hysteresis*. Springer, 1991, pp. 1–63.

[59] M. Rakotondrabe, "Classical prandtl-ishlinskii modeling and inverse multiplicative structure to compensate hysteresis in piezoactuators," in *2012 American control conference (ACC)*. IEEE, 2012, pp. 1646–1651.

[60] B. A. Cipra, "An introduction to the ising model," *The American Mathematical Monthly*, vol. 94, no. 10, pp. 937–959, 1987.

[61] R. C. Smith and Z. Ounaies, "A domain wall model for hysteresis in piezoelectric materials," *Journal of intelligent material systems and structures*, vol. 11, no. 1, pp. 62–79, 2000.

[62] R. C. Smith, "Inverse compensation for hysteresis in magnetostrictive transducers," *Mathematical and Computer Modelling*, vol. 33, no. 1-3, pp. 285–298, 2001.

[63] M. A. Johnson and M. H. Moradi, *PID control*. Springer, 2005.

[64] S. Pandey, A. James, R. Raman, S. Chatterjee, A. Goyal, C. Prakash, and T. Goel, "Structural, ferroelectric and optical properties of pzt thin films," *Physica B: Condensed Matter*, vol. 369, no. 1, pp. 135–142, 2005.

[65] K. Liang, A. Buditama, D. Chien, J. Cui, P. L. Cheung, S. Goljahi, S. H. Tolbert, J. P. Chang, and C. S. Lynch, "The conductivity mechanism and an improved cv model of ferroelectric pzt thin film," *Journal of Applied Physics*, vol. 117, no. 17, p. 174107, 2015.

[66] P. Horowitz, W. Hill, and I. Robinson, *The art of electronics*. Cambridge university press Cambridge, 1989, vol. 2.

[67] R. C. Smith and Z. Ounaies, "A domain wall model for hysteresis in piezoelectric materials," *Journal of Intelligent Material Systems and Structures*, vol. 11, no. 1, pp. 62–79, 2000.

[68] M. Nicolai, S. Eßlinger, and A. Schönecker, "Identification of process parameters for efficient poling of pzt ceramics for mass production," *Journal of Electroceramics*, vol. 32, no. 2-3, pp. 180–186, 2014.

[69] S. A. Rios and A. J. Fleming, "Design of a charge drive for reducing hysteresis in a piezoelectric bimorph actuator," *IEEE/ASME Transactions on Mechatronics*, vol. 21, no. 1, pp. 51–54, 2015.

[70] Y. Qin and R. Jia, "Adaptive hysteresis compensation of piezoelectric actuator using direct inverse modelling approach," *Micro & Nano Letters*, vol. 13, no. 2, pp. 180–183, 2018.

[71] M.-J. Yang, G.-Y. Gu, and L.-M. Zhu, "Parameter identification of the generalized prandtl–ishlinskii model for piezoelectric actuators using modified particle swarm optimization," *Sensors and Actuators A: Physical*, vol. 189, pp. 254–265, 2013.

[72] S. K. Karna, R. Sahai *et al.*, "An overview on taguchi method," *International journal of engineering and mathematical sciences*, vol. 1, no. 1, pp. 1–7, 2012.

[73] M. A. Zaman and M. A. Matin, "Optimization of jiles-atherton hysteresis model parameters using taguchi's method," *IEEE Transactions on Magnetics*, vol. 51, no. 5, pp. 1–4, 2015.

[74] J. A. Nelder and R. Mead, "A Simplex Method for Function Minimization," *The Computer Journal*, vol. 7, no. 4, pp. 308–313, 01 1965.

[75] Q. Zhang, Y. Dong, Y. Peng, J. Luo, S. Xie, and H. Pu, "Asymmetric bouc–wen hysteresis modeling and inverse compensation for piezoelectric actuator via a genetic algorithm–based particle swarm optimization identification algorithm," *Journal of Intelligent Material Systems and Structures*, vol. 30, no. 8, pp. 1263–1275, 2019.

[76] D. Tian and Z. Shi, "Mpso: Modified particle swarm optimization and its applications," *Swarm and evolutionary computation*, vol. 41, pp. 49–68, 2018.

[77] P. Kaelo and M. Ali, "A numerical study of some modified differential evolution algorithms," *European journal of operational research*, vol. 169, no. 3, pp. 1176–1184, 2006.

[78] R. Poli, J. Kennedy, and T. Blackwell, "Particle swarm optimization," *Swarm intelligence*, vol. 1, no. 1, pp. 33–57, 2007.

[79] J. C. Bansal, P. K. Singh, M. Saraswat, A. Verma, S. S. Jadon, and A. Abraham, "Inertia weight strategies in particle swarm optimization," in *2011 Third World Congress on Nature and Biologically Inspired Computing*, 2011, pp. 633–640.

[80] S. Helwig, J. Branke, and S. Mostaghim, "Experimental analysis of bound handling techniques in particle swarm optimization," *IEEE Transactions on Evolutionary Computation*, vol. 17, no. 2, pp. 259–271, 2013.

[81] R. Marion, R. Scorretti, N. Siauve, M.-A. Raulet, and L. Krahenbuhl, "Identification of jiles–atherton model parameters using particle swarm optimization," *IEEE Transactions on Magnetics*, vol. 44, no. 6, pp. 894–897, 2008.

[82] L. Chen, Y. Feng, R. Li, X. Chen, and H. Jiang, "Jiles-atherton based hysteresis identification of shape memory alloy-actuating compliant mechanism via modified particle swarm optimization algorithm," *Complexity*, vol. 2019, p. 7465461, Feb 2019.

[83] Y. Tian, J. Zhang, Z. jin Ren, W. Liu, Z. Jia, and Y. Qi, "A novel piezoelectric dynamometer based on double-sensor for thermal compensation," *Proceedings of the Institution of Mechanical Engineers, Part C: Journal of Mechanical Engineering Science*, vol. 231, no. 23, pp. 4479–4491, 2017.

[84] S. Roy, K. Lonkar, V. Janapati, and F.-K. Chang, "A novel physics-based temperature compensation model for structural health monitoring using ultrasonic guided waves," *Structural Health Monitoring*, vol. 13, no. 3, pp. 321–342, 2014.

[85] C. Fendzi, M. Rébillat, N. Mechbal, M. Guskov, and G. Coffignal, "A data-driven temperature compensation approach for structural health monitoring using lamb waves," *Structural Health Monitoring*, vol. 15, no. 5, pp. 525–540, 2016.

[86] J. Stone and L. Stulz, "Passively temperature-compensated nontunable fibre fabry-perot etalons," *Electronics Letters*, vol. 29, no. 18, pp. 1608–1609, 1993.

[87] M. Al Janaideh, M. Al Saaideh, and M. Rakotondrabe, "On hysteresis modeling of a piezoelectric precise positioning system under variable temperature," *Mechanical Systems and Signal Processing*, vol. 145, p. 106880, 2020.

[88] R. Gupta, R. Tandon, M. Tomar, V. Gupta *et al.*, "Electrocaloric effect in pzt thick

film for the cooling device applications," in *Advanced Functional Materials and Devices*. Springer, 2022, pp. 71–79.

[89] M. Goldfarb and N. Celanovic, "A Lumped Parameter Electromechanical Model for Describing the Nonlinear Behavior of Piezoelectric Actuators," *Journal of Dynamic Systems, Measurement, and Control*, vol. 119, no. 3, pp. 478–485, 09 1997.

[90] G.-Y. Gu, L.-M. Zhu, and C.-Y. Su, "Modeling and compensation of asymmetric hysteresis nonlinearity for piezoceramic actuators with a modified prandtl–ishlinskii model," *IEEE Transactions on Industrial Electronics*, vol. 61, no. 3, pp. 1583–1595, 2014.

[91] B. Wen, Y. Zhang, X. Liu, L. Ma, and X. Wang, "Temperature-dependent ferroelectric hysteresis properties of modified lead zirconate titanate ceramics," *Journal of Materials Science*, vol. 47, no. 10, pp. 4299–4304, 2012.

[92] A. Raghunathan, Y. Melikhov, J. E. Snyder, and D. C. Jiles, "Modeling the temperature dependence of hysteresis based on jiles–atherton theory," *IEEE Transactions on Magnetics*, vol. 45, no. 10, pp. 3954–3957, 2009.

[93] J. S. Smart and J. H. Van Vleck, "Effective field theories of magnetism," *Physics today*, vol. 19, no. 8, pp. 77–78, 1966.